UNIVERSIDADE FEDERAL DE MINAS GERAIS
Programa de Pós-Graduação em Engenharia Metalúrgica, Materiais e de Minas

Doctoral Dissertation

Development of Magnesium-Based Hybrids through High-Pressure Torsion

Author: Moara Marques De Castro
Supervisor: Roberto Braga Figueiredo
Co-Supervisor: Augusta Cerceau Isaac Neta

May 2021

Moara Marques de Castro

Desenvolvimento de Híbridos a Base de Magnésio através de Torsão sob Elevada Pressão

(Development of Magnesium-Based Hybrids through High-Pressure Torsion)

Tese submetida ao programa de pós graduação de engenharia metalúrgica, de materiais e de minas, na escola de engenharia da Universidade Federal de Minas Gerais, para a obtenção do título de doutor em engenharia metalúrgica.

Área de concentração: Metalurgia física
Orientador: Roberto Braga Figueiredo
Coorientadora: Augusta Cerceau Isaac Neta

Belo Horizonte
Universidade Federal de Minas Gerais
Escola de Engenharia
2021

Castro, Moara Marques de.
C355d Desenvolvimento de híbridos a base de magnésio através da torsão sob elevada pressão = Development of magnesium-based hybrids trough high-pressure torsion [recurso eletrônico] / Moara Marques de Castro. – 2021.
1 recurso online (xi, 150 f. : il., color.) : pdf.

Orientador: Roberto Braga Figueiredo.
Coorientadora: Augusta Cerceau Isaac Neta.

Tese (doutorado) - Universidade Federal de Minas Gerais, Escola de Engenharia.

Inclui bibliografia.
Exigências do sistema: Adobe Acrobat Reader.

1. Engenharia metalúrgica - Teses. 2. Magnésio – Teses. 3. Deformações e tensões – Teses. I. Figueiredo, Roberto Braga. II. Isaac Neta, Augusta Cerceau. III. Universidade Federal de Minas Gerais. Escola de Engenharia. IV. Título.

CDU: 669(043)

Ficha catalográfica elaborada pela Bibliotecária Letícia Alves Vieira - CRB-6/2337
Biblioteca Prof. Mário Werneck - Escola de Engenharia da UFMG

UNIVERSIDADE FEDERAL DE MINAS GERAIS
ESCOLA DE ENGENHARIA
Programa de Pós-Graduação em Engenharia Metalúrgica, Materiais e de Minas

Tese intitulada **"Development Of Magnesium-based Hybrids Through High-pressure Torsion"**, área de concentração: Metalurgia Física, apresentada pela candidata **Moara Marques de Castro**, para obtenção do grau de Doutora em Engenharia Metalúrgica, Materiais e de Minas, aprovada pela comissão examinadora constituída pelos seguintes membros:

Prof. Roberto Braga Figueiredo
Orientador - Dr. (UFMG)

Profª Augusta Cerceau Isaac Neta
Coorientadora - Drª (UFMG)

Prof. Witor Wolf
Dr. (UFMG)

Prof. Sergio Neves Monteiro
Dr. (Instituto Militar de Engenharia (IME))

Prof. Conrado Ramos Moreira Afonso
Dr. (UFSCar)

Prof. Megumi Kawasaki
Dr. (Oregon State University (OSU))

Coordenador do Programa de Pós-Graduação em Engenharia Metalúrgica, Materiais e de Minas/UFMG

Belo Horizonte, 20 de maio de 2021

Abstract

High-pressure torsion (HPT) is a well-established severe plastic deformation technique for achieving substantial grain refinement and improving mechanical resistance in metallic materials. Besides, HPT can also consolidate metallic particles into a bulk solid disc and incorporate other materials (as hard materials, bioactive materials or other metallic materials) to tailor a variety of hybrids. The present work explores the fabrication of different magnesium matrix hybrids, developed by blending Mg particles with varying kinds of reinforcement, using HPT processing for consolidation. It is shown that hybrids with mechanical integrity can be fabricated by this method. Different characterization techniques, including optical and electron microscopy, are used to analyse the microstructural evolution of the produced hybrids. Well-dispersed second phase particles within continuous and refined magnesium matrix are obtained. The distribution of phases may be controlled by the amount of rotation imposed during processing. The mechanical properties are evaluated by hardness tests and miniature-tensile tests, showing that the composites might display improved strength and tensile resistance, indicating a good bonding of particles. Evidence of a Hall-Petch break-down was identified in a Mg alloy-alumina hybrid, and higher hardness was achieved in Mg-Zn hybrids due to grain refinement, fragmentation of phases, segregation of alloying elements along grain boundaries and precipitation of intermetallics. The hybrids produced using high-pressure torsion have different potential applications, including the development of bioactive and biodegradable implants.

Keywords: Nanostructured composites, Magnesium, High-pressure torsion, Hybrids, Particles consolidation.

Resumo

A torção de alta pressão (HPT) é uma técnica de deformação plástica severa bem estabelecida para alcançar um substancial refino de grãos e melhorar a resistência mecânica em materiais metálicos. Além disso, o HPT também pode transformar partículas metálicas em um disco sólido maciço, podendo ou não conter outros materiais incorporados (ex.: materiais duros, materiais bioativos, outros materiais metálicos, etc.), possibilitando a criação de uma variedade de híbridos. Assim, o presente trabalho explora a fabricação de diferentes híbridos de matriz de magnésio desenvolvidos através do processamento por HPT para misturar e consolidar partículas de Mg com diversos tipos de reforço. É mostrado que esse método permite a fabricação de híbridos com efetiva integridade mecânica. Diferentes técnicas de caracterização, incluindo microscopia óptica e eletrônica, são utilizadas para analisar a evolução microestrutural dos híbridos produzidos. Foram observadas partículas de segunda fase bem dispersas ao longo de uma matriz íntegra e refinada de magnésio. Tal distribuição de fases pode ser controlada pela quantidade de rotações imposta durante o processamento. As propriedades mecânicas são avaliadas por ensaios de dureza e ensaios de tração em miniatura, mostrando que os compósitos podem apresentar melhor dureza e resistência à tração. Os resultados indicaram uma boa aderência das partículas de magnésio. Também foram identificadas evidências de quebra de Hall-Petch em um híbrido da liga de Mg reforçado com alumina, e uma maior dureza foi alcançada em híbridos de Mg-Zn devido ao refino de grãos, fragmentação de fases, segregação de elementos de liga ao longo dos contornos de grãos e precipitação de intermetálicos. Os híbridos de Mg produzidos por HPT têm diferentes aplicações potenciais, incluindo o desenvolvimento de implantes bioativos e biodegradáveis.

Palavras chave: Compósitos nanoestruturados, Magnésio, Torsão sob elevada pressão, Híbridos, Consolidação de partículas.

Acknowledgements

First, I would like to thank the financial support from CAPES (*Coordenação de Aperfeiçoamento Pessoal de Nível Superior*), which enabled me to pursue a doctoral degree and provided fellowships as a doctoral candidate and as a visiting research scholar at OSU.

Next, I would like to thank my supervisor, Dr Roberto Figueiredo, to provide me with thoughtful guidance and make this work possible. There are no words I can express my gratitude and appreciation for all the trust, patience and countless hours this outstanding researcher dedicated to helping me during this project. I also thank Dr Augusta Isaac, my co-supervisor, who always provided encouragement and assistance throughout the doctorate. I identify with her style and have her as inspiration to keep doing the hard work. I can say the same about Dr Megumi Kawasaki, another brilliant researcher who strongly contributed to my formation. I thank the great support during my stay in Oregon. She is also one of the most intelligent women I ever met, and I am grateful for having the opportunity to learn directly from these female models in my field.

Furthermore, I thank Dr Pedro Pereira for the collaborative effort, the help with HPT processing, and the precious insights in the qualifying exam. I also thank and all collaborators that enabled the development of this research. I cannot forget to mention my gratitude to the Metallurgical Engineering Department at UFMG and all its other members' staff. Labs, consumables, grants, and a highly qualified body of professors, I am grateful to have them all. I especially thank Professor Dagoberto and Professor Berenice for providing valuable assistance since my undergraduate. It is important to mention that I could not have completed this dissertation without my dear friends, who always gave me strength and helping me keep focused on this final lap (even from a distance, by our zoom sections).

Finally, I thank the love, support, and understanding of my family. Mom and dad, I thank you for always being there for me and making me able to pursue what I wanted to be. Leo, the new family I chose, thank you for the unconditional support throughout these four years. I am immensely grateful for having you as my partner giving me strength, sharing my dreams and aiming high with me. All in all, I must thank God for this trajectory; it definitely was not easy, but certainly the right one.

Table of Contents

Definitions and Abbreviations

ADF – Annular dark-field
BF – Bright-field
BG – Bioactive glass
BSE – Backscattered electrons
CNT – Carbon nanotubes
CP – Commercial purity
d – Grain size
ECAP – Equal channel angular pressing
FFT – Fast Fourier transform
h – Sample's thickness
HA – Hydroxyapatite
HAADF – High angular annular dark field
HBSS – Hank's balanced salt solution
HPT – High-pressure torsion
m – Strain rate sensitivity
MMC – Metal-matrix composite
N – Number of HPT revolutions
r – Distance to the centre in HPT sample
P – Pressure
PM – Powder metallurgy
RT – Room temperature
SE – Secondary electrons
SEM – Scanning electron microscope
SBF – Simulated body fluid
SPD – Severe plastic deformation
STEM – Scanning transmission electron microscopy
TEM – Transmission electron microscope
UTS – Ultimate tensile strength
XRD – X-ray diffraction
ε_{ef} – Equivalent plastic strain
σ – Flow stress
γ – Shear strain
ω – Angular velocity

Considerações iniciais

Cada vez mais, o magnésio vem despertando o interesse de pesquisadores de diversas áreas dado suas propriedades únicas. Além de ser o metal estrutural mais leve (aproximadamente 35% mais leve que o alumínio e 60% mais leve que o titânio), o Mg também apresenta boa capacidade de amortecimento e pode atingir uma alta relação resistência-peso. Tais características o tornam um material estratégico para a fabricação de componentes de veículos haja visto que menos peso proporciona não só um melhor desempenho, mas também benefícios econômicos e ambientais. Além disso, o Mg possui densidade muito semelhante a dos ossos, é biocompatível, biodegradável, e suas propriedades mecânicas são boas o suficiente para atuar como implantes temporários que auxiliam na recuperação óssea sem gerar problemas de desgaste por estresse nos tecidos adjacentes ao implante (fenômeno conhecido como "remodelação óssea proximal adaptativa", ou, "*stress shielding*"). A vantagem em fabricar implantes bioabsorvíveis é oferecer a possibilidade de dispensar uma segunda cirurgia (para a retirada do dispositivo), evitando assim custos extras, dor e riscos cirúrgicos.

Apesar do aumento significativo de estudos sobre Mg e suas ligas, esses materiais ainda apresentam sérias limitações a serem superadas. As ligas de magnésio costumam exibir alta taxa de corrosão em meio biológico e propriedades mecânicas inferiores a de outros materiais de engenharia (como, por exemplo, relativa baixa resistência à tração e natureza frágil). Neste contexto, diferentes abordagens foram desenvolvidas para superar tais limitações. Houve uma ênfase especial no desenvolvimento de novas ligas e na otimização das técnicas de processamento. Neste último caso, os pesquisadores muitas vezes visam alcançar refinamento aprimorado de grãos e endurecimento por deformação. Outra abordagem que vem recebendo grande atenção é o desenvolvimento de híbridos, sendo um híbrido uma combinação de materiais que apresenta propriedades específicas muitas vezes melhores do que as apresentadas por cada material que os compõem quando isolados. Um exemplo de uma classe comum de híbridos é o compósito de matriz metálica, que consiste em uma matriz metálica reforçada com uma fase rígida (normalmente, cerâmica) dispersa nele.

Entre as rotas de produção até agora desenvolvidas para a fabricação desses compósitos, a deformação plástica severa (SPD) permite a exploração de novos sistemas contendo Mg para uma ampla gama de aplicações. Além da grande

capacidade de promover uma microestrutura ultrafina, os processos SPD surgiram como ferramentas poderosas para consolidar compósitos a partir de cavacos metálicos, particulados ou pós. Considerando todos os processos de SPD desenvolvidos até hoje, a torção sob elevada pressão (HPT) pode impor maior deformação ao material, proporcionando não só o um refino de grãos mais expressivo, mas também a possibilidade de consolidação das partículas metálicas mesmo em temperatura ambiente. Isso é de grande importância para reter as fases metaestáveis e nanoestruturas desenvolvidas durante o processamento. Também é importante mencionar que a possibilidade de consolidação de partículas oferece a oportunidade de reciclar pós metálicos, peças quebradas ou cavacos de usinagem.

Dado o grande potencial do HPT para consolidar partículas metálicas, muitos cientistas foram atraídos pela oportunidade de criar novos híbridos com uma estrutura ultrafina e propriedades mecânicas excepcionais. Muitos trabalhos na literatura confirmam a fabricação de híbridos de matriz metálica e relatam a elevada resistência mecânica desses materiais. No entanto, devido ao tamanho reduzido das amostras, a maioria das publicações relata a utilização de ensaios de microdureza para avaliar a resistência do material fabricado. Embora esses testes sejam uma maneira rápida e eficaz de estimar a resistência, eles não avaliam verdadeiramente o nível de consolidação e integridade mecânica. Espera-se que testes de tração miniaturizados forneçam uma estimativa mais abrangente da integridade, uma vez que as áreas nas quais a consolidação foi ineficaz agiriam como trincas internas e comprometeriam a resistência à tração. Além disso, ainda existem dúvidas sobre como os materiais particulados interagem durante o HPT e quais são as condições para a efetiva união ou dispersão eficiente das fases. Por fim, pode-se notar que, apesar do estudo de múltiplos sistemas, a consolidação de sistemas de Mg por HPT permanece pouco explorada.

Dessa forma, o objetivo desta tese é estudar o desenvolvimento de híbridos à base de magnésio por meio da consolidação de partículas utilizando o processamento HPT em temperatura ambiente. Especificamente, este trabalho visa produzir diferentes híbridos de magnésio incorporando três tipos diferentes de reforços: materiais duros inertes, materiais bioativos e material metálico macio. Além disso, este trabalho também pretende fornecer maiores esclarecimentos sobre a integridade mecânica e caracterização estrutural desses materiais.

Chapter 1.

Introduction

1.1. Motivation and background

Magnesium has been attracting a renewed interest of researchers from different areas due to its unique properties. It is the lightest structural metallic material, being approximately 35% lighter than aluminium and 60% lighter than titanium. Mg also presents good dampening capacity and can achieve high specific strength, making it an interesting component for vehicles not only for better performance but also for economic and environmental benefits. Besides, Mg has a very similar density to that of the cortical bone, it is biocompatible, biodegradable, and its mechanical properties are good enough for acting as temporary implants to assist bone healing with no problems related to stress shield. The use of bioabsorbable devices is of great interest for dispensing a second surgery to remove the device, avoiding extra costs, pain, and surgical risks. Despite the significant increase in the number of studies on Mg and its alloys for a wide range of applications, these materials still present some important limitations which should be overcome. Magnesium alloys often exhibit high reactivity, brittle nature, and inferior mechanical properties compared to other engineering materials.

Different approaches have been developed to overcome the main limitations of the Mg alloys. There has been a special emphasis on the development of novel alloys and the optimization of the processing techniques. In the latter case, researchers often aim to achieve enhanced grain refinement and strain hardening. Another approach that is attracting considerable attention is the development of hybrids, which is a combination of materials to present better properties than the single materials that compose it. An example of a common class of hybrids is metal-matrix composite (MMC), which consists of a hard-reinforcing phase (typically, ceramics) dispersed in a metallic matrix.

Among the production routes hitherto developed for manufacturing MMCs, severe plastic deformation (SPD) enables the exploration of novel Mg-based systems for a wide range of applications. Besides the great capacity to achieve ultrafine microstructure, SPD processes have emerged as powerful tools to consolidate

composites from metal chips, particulates, or powders. Considering all the SPD processes developed so far, high-pressure torsion (HPT) can impose larger deformation on the material, providing not only the most expressive grain refinement but also the possibility of consolidating metal particles even at room temperature. This is particularly important for retaining metastable phases and nanostructures developed during processing. It should also be mentioned the possibility of consolidating particles offers the opportunity to recycle metallic powders, broken pieces, or machining chips.

Realising all the potential of HPT to consolidate metallic particles, many scientists have been attracted to the opportunity to create new hybrids with an ultrafine structure and unprecedented mechanical properties or functionalities. Many papers in the literature confirm the fabrication of metal matrix hybrids and report improved mechanical strength in these materials. However, due to the reduced sample sizes, the majority of these papers use microhardness tests to evaluate the strength. Although these tests provide a quick and effective way to estimate the strength, it does not truly evaluate the level of consolidation and mechanical integrity. Micro-tensile tests are expected to provide a more comprehensive estimation of the integrity since areas in which consolidation was ineffective would act as internal cracks and compromise the tensile strength. Also, there are still doubts about how particulate materials interact during HPT and the conditions for effective bonding and dispersion of phases to be achieved. Finally, it can be noticed that, despite the study of multiple systems, the consolidation of Mg-based systems by HPT remains less explored.

1.2. Objectives

The objective of the present research work is to develop magnesium-based hybrids through the consolidation of particles using HPT processing at room temperature. The specific objective of this work is to produce different magnesium hybrids by incorporating three kinds of reinforcement phases: inert hard particles, bioactive material, and a soft metallic phase. In addition to this objective, this work also aims to provide further insights into the mechanical integrity and structure characterization of these materials. Furthermore, the microstructural changes and mechanical properties of the processed samples will be compared when the materials are mixed or not with additional phases.

1.3. Thesis Structure

This doctoral thesis is composed of 9 chapters, including as-submitted versions of manuscripts that were prepared during this research. The first chapter presents an introduction of the theme and includes a brief background and motivation for this research, as well as the general aims and objectives of the work. The second chapter shows a literature review covering some properties and applications of Mg-based materials, the definition of hybrid materials, some fabrication techniques to produce metal-matrix hybrids, and the fundamental concepts of severe plastic deformation, more specifically, high-pressure torsion. Emphasis is given to their potential to produce a variety of hybrids (that includes metal-matrix composites reinforced with some hard phase, as well as combinations of metallic materials to create, for example, layered structures). It also describes the most critical aspects of Mg-based composites designed for structural or functional applications. Chapters 3 to 8 are manuscripts of papers produced as a consequence of the present work. These manuscripts report the experimental procedures, results obtained, discussion of the results, conclusions and references. A brief description of each chapter is given below.

Chapter 3: reports the initial attempts to consolidate magnesium chips and early difficulties in obtaining full consolidation;

Chapter 4: reports the consolidation of Mg chips with Al_2O_3 particles and characterization of the dispersion of the second phase;

Chapter 6: reports the consolidation of a magnesium alloy AZ91 with Al_2O_3 particles and shows evidence of inverse Hall-Petch behaviour in the hybrid;

Chapter 5: reports the consolidation of Mg and an Mg alloy with quasicrystal particles and tensile tests of some composites;

Chapter 7: reports the consolidation of Mg-based composites with the incorporation of bioactive materials and initial characterization of these materials;

Chapter 8: reports the consolidation of multiple Mg-Zn hybrids and the characterization of the structure and mechanical properties.

Finally, the last chapter presents a summary of the main conclusions obtained in this study, other original contributions and suggestions for future work.

Chapter 2.

Literature review

2.1. Magnesium: properties and applications

2.1.1. A structural light-weight material

Magnesium and its alloys present several advantageous properties for a variety of usages. With a density of 1.74 g/cm³, Mg is the lightest metal for structural applications, being approximately 33% lighter than aluminium, 60% lighter than titanium and 78% lighter than steel. As can be seen in the strength-to-density property chart in Figure 2.1, Mg and its alloys can present high specific strength when compared to other metals commonly used for structural applications, what makes them extremely attractive to producing components for vehicles, sporting goods, and portable devices [1-4].

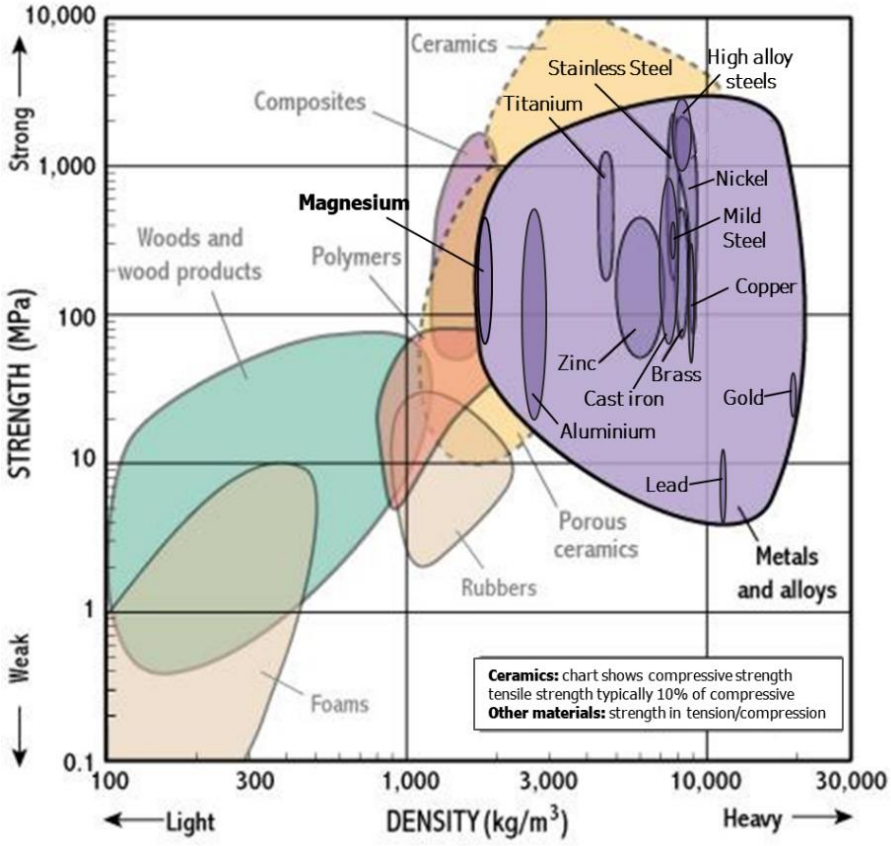

Figure 2.1 - Strength-to-density property chart of some metals and alloys [5].

Efforts have been made by academics and industrials partners to produce and improve Mg-based materials not only for achieving even higher specific strength [6-9], but also to overcome their relative low elastic modulus, low toughness, and low creep resistance [10]. Common approaches are combining Mg with other elements, either chemically to form an alloy or mechanically to build a hybrid, as well as refining the microstructure through mechanical processing. One motivation is that the weight reduction can lead not only to an increase in comfort and performance but also to positive economic impacts and environmental benefits, considering that lighter vehicles enable less fuel consumption and fewer pollution emissions [11]. Nowadays, in the transport industry, many magnesium components are being produced to be used in aircraft and automobiles [11-13]. Some magnesium components used in automobiles are illustrated in Figure 2.2.

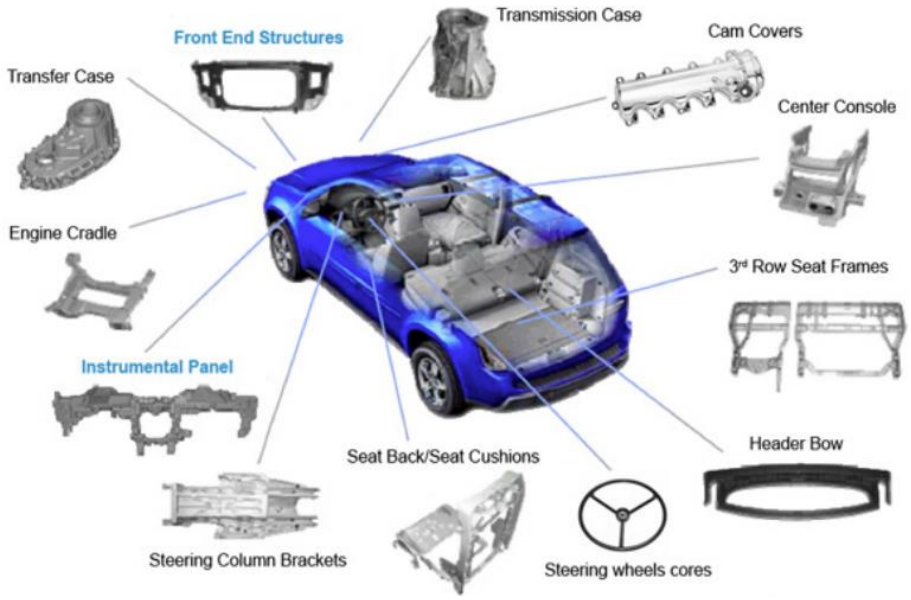

Figure 2.2 - Examples of applications for magnesium alloys in the automotive industry (from B. Gwynne and P. Lyon, 2007, apud in [11])

Together with their high specific strength, magnesium and its alloys also can present a high damping capacity and a good shielding capacity, offering good vibration absorption in high-speed vehicles and electromagnetic interference reduction in electronic devices. Additional reasons that motivate an increasing use of these materials for structural applications are that the production of Mg-based items is facilitated by their high dimensional stability, good castability and good machinability [14]. The full recyclability and ample availability of the metal also contribute to the increasing interest in this metal [13].

2.1.2. A biocompatible and biodegradable material

Magnesium also gets a lot of attention in the medical field [15-17]. It is not only biocompatible but also highly biodegradable, so it can be absorbed by the body and completely excreted by the urine with no toxic risk during degradation [17]. Therefore, Mg is a potential material for producing absorbable orthopaedic implants that would dispense a surgery to remove the device, avoiding extra surgical risks, pain, and costs. Besides its high biocompatibility, Mg appears like an asset since both its density (1.738 g/cm^3) and its tensile strength (80-280 MPa) are similar to that of the bone, with advantages as higher fracture toughness [18]. Having a similar density and smaller elastic modulus mismatch (when compared to other biocompatible metals such as titanium alloys or stainless steel) alleviates stress-shielding effects between bone and the implant material [19].

Since magnesium possesses high chemical reactivity and a high degradation rate in body fluid, much effort has been made to develop new alloys or composites with improved corrosion resistance, allowing adequate biological applicability. For that, choosing suitable alloying elements or reinforcements with no toxicity is as important as adjusting the microstructure. Although nowadays there is a variety of Mg implants being produced as bone screws, pins, nails, and vascular stents (some are illustrated in Figure 2.3), the production of Mg-based implants with a controlled corrosion rate still remains challenging.

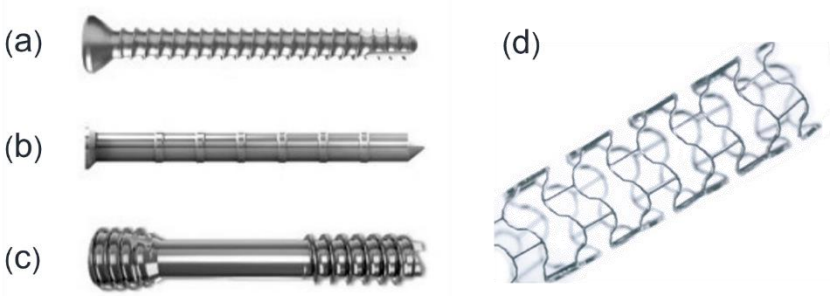

Figure 2.3 – Examples of commercial magnesium-implants: a) cortical bone screw; b) pin; c) compression screw; d) stent. (a-c) are based on the alloy MgYREZr (MAGNEZIX®, Syntellix AG, Hannover, Germany) [20], and (d) from AE21 alloy (BIOTRONIK, Berlin, Germany)[21].

2.2. Hybrids and composites

2.2.1. definition and examples

The terms "hybrids" and "composites" are used in engineering to describe an arrangement of materials structured to achieve better performance than the components would offer individually in a certain application. Generally, the term "composite" refers to a material composed of elements that have different nature (a combination of ceramic, metallic, or polymeric materials), and the harder phase is segmented and embedded in the plastic one, acting as a reinforcement [22]. "Hybrids" instead refers to combinations in general and not restricted to composites with particulate reinforcements, but also sandwich, foams, segmented, and lattice structures. As explained by Ashby (2005), and according to the research work of Ashby and Bréchet (2003) [23, 24], a hybrid is a combination of two or more monolithic materials (or a material and space) in a determined configuration and scale, assembled in a way as to have attributes not offered by either one alone (Figure 2.4).

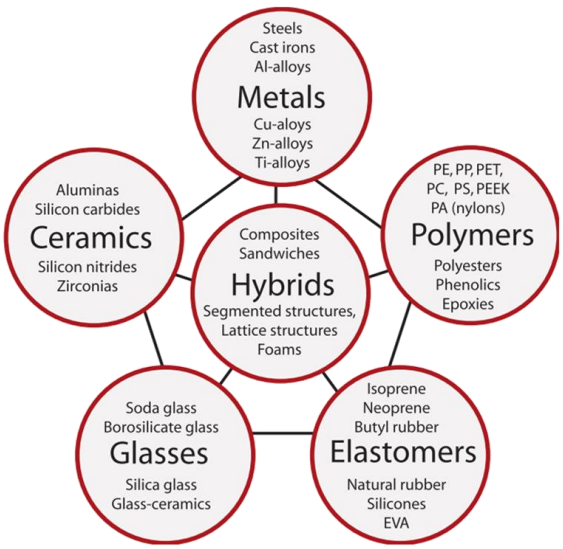

Figure 2.4 - Classes of materials, including the different types of hybrids.[23]

Even so, these terms are sometimes mixed [25, 26], and a clear definition is still not established among all research groups. The present work follows the definition proposed by Ashby, as composites being specifically the combination of monolithic materials having different natures (i.e. a metal with dispersed oxides within), and hybrid being a more general combination. That includes a mixture of metals (i.e. materials of the same nature) that, instead of forming a chemically homogeneous alloy, present distinguishable portions of each metal throughout the piece.

2.2.2. Mg-based composites

Intensive research in the field of advanced light-weight materials leads to an increasing interest in metal-matrix composites (MMCs) with a high specific strength. Specifically, several Mg-based composites have been developed to overcome Mg's poor ductility at room temperature and its poor corrosion resistance. There are now many papers discussing different processing routes and their influence on the grain size of the matrix and the 2nd phase dispersion. Also, the effect of nature and fraction of reinforcements in the final microstructure and mechanical properties of the studied MMCs (as well as their biocompatibility and degradation rate for the ones fabricated aiming biomedical applications) have been investigated.

Some studies about Mg-based composites fabricated by different processing techniques are presented in the following section. Common aspects of these studies are that the addition of reinforcement particulates usually improves the mechanical properties of Mg (such as hardness, tensile, thermal and tribological properties) considerably. That can be related to the better load sharing ability between the hard reinforcing phases and the metal matrix [27], but more importantly, to the smaller grain size attained at the matrix after secondary processing. Also, reinforcements morphology, distribution, and their interfacial bonding to the matrix have a deep impact on the structural integrity of the composite. The final grain structure, aggregation and segregation of particles and the presence of internal defects as porosity or lack of bonding are strongly related to the fabrication processes [27].

2.2.3. Processing routes to produce Mg-based composites

The fabrication methods used to produce MMCs can be divided into either liquid state (casting) or solid-state processing route (powder metallurgy). Some research works about selected Mg-based composites (reinforced with either bioactive or inert hard phases) and hybrids (combining Mg with other metals or multiple types of reinforcements) are presented in the following pages.

In routes that involve casting, the hard phase is inserted in a liquid bath of the matrix-metal, either by pumping the melted metal at high pressure into a die (which can contain the reinforcement dispersed or as a preform) or by adding the hard

phase directly into the melted metallic bath and stirring it. The solidified product usually goes through secondary processing to achieve a more refined structure with a homogeneous distribution of the 2nd phase. For example, Khanra *et al.* [28, 29] used stir casting to insert hydroxyapatite (HA) in an Mg matrix and fabricate Mg-xHA and ZM61-xHA composites having different fractions of HA (x = 0, 5, 10 and 15 wt%). Hot extrusion was performed on the casted billets. The HA addition leads to grain refinement, increases compressive strength and decreases UTS (from 187.9 MPa in Mg to 136.7 MPa in Mg-15% HA, and from 301 MPa in ZM61 to 225.5 MPa in ZM61-15% HA, respectively).

Other Mg-based composites fabricated by liquid state route were Mg-Zn-Zr matrix composites reinforced with 0.5, 1 and 1.5 wt% of HA [30, 31]. The addition of 1 wt% HA led to better improvement in mechanical properties and reduction in corrosion rate. Rahmany-Gorji *et al.* [32] fabricated ZX51-xAl_2O_3 composites (x = 0, 2.25, 4.50 and 6.75 vol%) and evaluated the effect of an increasing fraction of reinforcement in microstructural and mechanical properties of the composite. The addition of Al_2O_3 increased hardness and yield strength while reducing tensile strength, compressive strength, and ductility. It also brought grain refinement to the matrix (as can be seen in Figure 2.5), but increased the porosity [32].

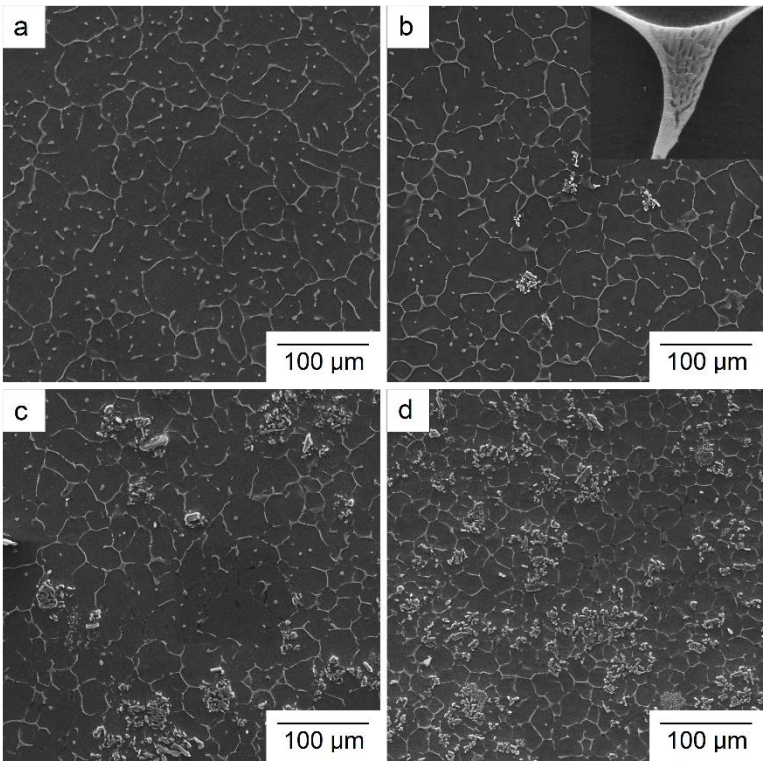

Figure 2.5 - SEM images of cast composites containing (a) 0, (b) 2.25, (c) 4.50, and (d) 6.75% Al_2O_3. Average grain sizes are 45.3, 43.5, 24.9, and 18.7 µm, respectively. Adapted from [32].

Aatthisugan *et al.* [33] also used stir casting to produce Mg-based composites, but hybrids composites reinforced with boron carbide (B_4C) and graphite (Gr) particles. Both AZ91D-1.5wt%B_4C-1.5wt%Gr and AZ91D-1.5 wt%B_4C presented better wear resistance and tensile properties than the unreinforced AZ91D alloy, with the last achieving an improvement in hardness and UTS of 32% and 60%, respectively.

In the squeeze casting technique, the molten metal is poured into the lower die, which contains a preform of the reinforcements, then pressure is applied. This method allows producing higher volume fractions of the reinforcements (up to 50%) and achieving a fine grain structure. Sankaranarayanan *et al.* [34] used disintegrated melt deposition (DMD) to fabricate Mg-5.6Ti-xB_4C hybrids. Powders were ball milled previously to DMD, and the hybrids were machined and hot extruded, leading to a good interfacial bonding and homogeneous distribution of phases. The reinforced composite presents finer grain structure and enhanced strength properties under tension and compression without losing ductility [34].

Many Mg-based hybrids are also fabricated using solid-state routes, which involve particles mixture and consolidation induced by high-temperature diffusion, intense plastic deformation, or both. Powder metallurgy (PM) techniques consist of blending powders of metals (matrix) and hard material (reinforcement), pressing the blended mixture in the desired format, then sintering the green compact at a specific temperature in a controlled atmosphere [27]. Setyadi *et al.* [35] fabricated magnesium composites reinforced with 5, 10 and 15 wt% of carbonate apatite (CA) by PM. Higher milling times and higher CA content increased hardness up to ~20% compared to pure magnesium (hardness went from 37.3 HV in pure consolidated Mg to 44.8 HV in Mg-15% CA). The composite Mg-10% CA presented the optimal composition. Salleh *et al.* [36] produce Mg6.5Zn matrix composites with 10wt% HA by mechanical milling and PM, and the composite exhibited the highest corrosion resistance in Hank's balanced salt solution (HBSS). The progressive effect of HA decelerates the Mg degradation rate. After seven days of immersion, the compressive strength for the composite and the alloy is considerably higher than the cortical bone. Jaiswal *et al.* [37] used a double-step sintering PM process at 450° to 550° C to fabricate Mg3Zn matrix composite reinforced with 2, 5 and 10wt% of HA. As presented in Figure 2.6, the addition of 5% of HA effectively reduced the corrosion rate by 42% in simulated body fluid and improved the compressive yield strength by 23%. Stüpp *et al.* [38] used ball milling and hot extrusion at 270°C to produce ZK60-xHA composites (x = 0, 10, 20 wt%). It was noticed a slight

improvement in the corrosion resistance for the composites in fetal bovine serum. Also, samples showed a slight increase in the compressive yield strength with the addition of HA.

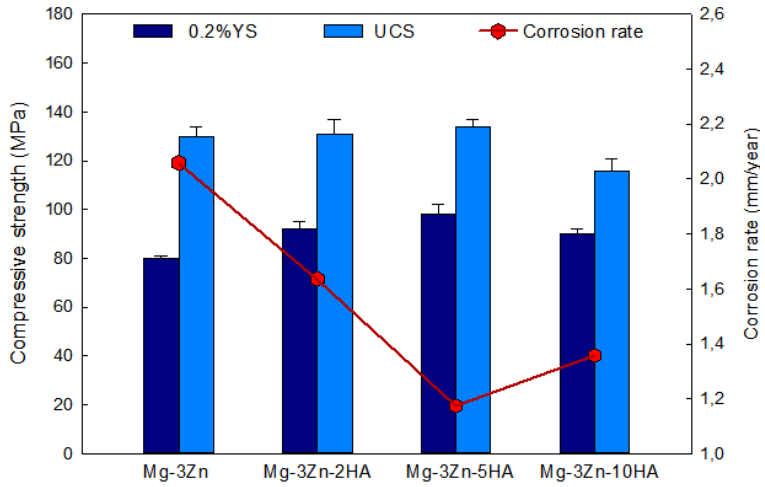

Figure 2.6 - Compressive strength and corrosion resistance of the Mg-3Zn-xHA composites produced by double-steep sintering PM process (Adapted from [37])

Usually, to ensure full densification of the composite, the majority of the solid-state techniques take place at high temperatures (but below materials' melting temperature). That is because heat, as well as pressure, enhances atomic diffusion, favouring the achievement of good mechanical integrity. Conventional powder metallurgy strongly relies on diffusional processes, that are favoured by longer sintering times and higher temperatures, leading to significant grain growth during processing. To minimize this, alternative techniques that shorten the sintering time are preferred. For instance, in microwave-assisted processing technique [39], heat is rapidly induced by electromagnetic waves in a high-frequency electric field.

Wan *et al.* [39] used microwave-assisted processing to produce Mg composites reinforced with 5, 10 and 15% bioactive glass (BG). The starting materials were ball milled and sintered in a microwave furnace at 500°C. As illustrated in Figure 2.7, the addition of BG considerably reduced hydrogen evolution, avoided significant pH change, and improved biocompatibility, and the Mg-10% BG composite presented the best mechanical and biological behaviour. The compressive strength and modulus improved 34.0% and 18.7%, respectively, compared to Mg.

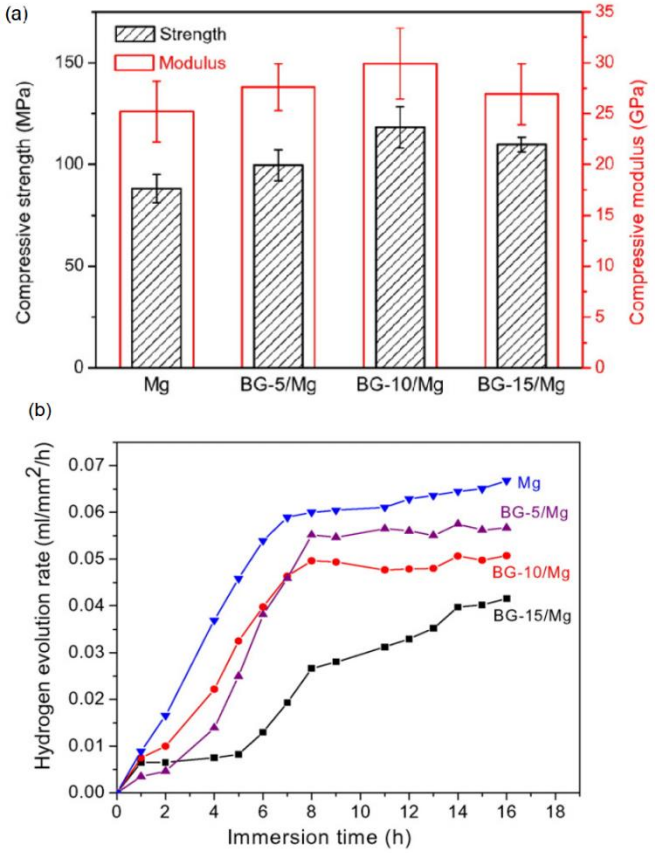

Figure 2.7 - (a) Compressive strength of Mg/Mg-BG composites and their (b) hydrogen evolution rate after immersion in SBF at 37°C [39]

Xiong *et al.* [40] produced Mg-xHA composites (x = 0, 5, 10 and 15 wt%) using the same technique. All composites presented a homogeneous microstructure with the HA well spread into the Mg matrix. The sample which presents the optimum composition (that achieves the lower corrosion rate and the better strength and modulus in compression) is the Mg-10% HA one. Kujur *et al.* [14] developed Mg composites reinforced with cerium oxide (CeO_2) nanoparticles combining microwave sintering and hot extrusion. The uniform distribution of nanoparticles with good matrix-reinforcement interfacial integrity leads to increased hardness with the progressive addition of the oxides (Mg, Mg-0.5 CeO_2, Mg-1.0 CeO_2, and Mg-1.5 CeO_2). Besides, both thermal and dimensional stability were enhanced compared to pure Mg, just as resistance to ignition, damping capacity, yield stress and ultimate compression stress [14].

Another approach is to apply high pressure to enable faster and better densification using considerably lower temperatures than in conventional sintering, leading to a more refined microstructure. Examples are spark plasma sintering (SPS) [41] and severe plastic deformation (SPD) processing [42].

Sunil *et al.* [41] used ball milling and SPS at 450° to produced Mg-xHA composites (x = 0, 8, 10 and 15 wt%). Young's modulus and fracture toughness decreased with the increase of HA content but were improved compared to the as-cast Mg. The Mg-10%HA composite presents the better corrosion resistance among the samples. On the other hand, Torabi *et al.* [43] used SPD to fabricate Mg-xHA composites (x = 0, 2, 5 and 10 wt%) at 400°C. They combined cyclic extrusion compression (CEC), equal channel angular pressing (ECAP) and conventional extrusion. Among all samples, the Mg-5% HA composite presents the finest grains and exhibits the highest hardness and strength. Also, hydrogen evolution tests and potentiodynamic polarisation tests showed that this composite has the lowest values of evolved hydrogen, weight loss and corrosion current density. Its corrosion resistance is also better than in cast and extruded pure Mg. The CECAP-FE process proved to be able to achieve a good and homogenous reinforcement dispersion until 5 wt% of HA. Adding more reinforcement deteriorate mechanical properties and corrosion resistance, that is directedly related to the development of the inhomogeneous microstructure and HA agglomerations. Friction stir processing (FSP) is another SPD method used to fabricate Mg-based composites. Lu *et al.* [44] applied FSP to incorporate nano-Al_2O_3 and carbon nanotubes (CNT) in an AZ31 matrix, while Azizieh *et al.* [45] used it to add Al particles in a pure Mg matrix and form in situ $Al_{12}Mg_{17}$ phase. Other SPD techniques will be presented in the following section.

2.2.4. Using SPD processing to produce composites

Usual metal forming process leads to a reduction of the cross-section of the sample at each processing step. In contrast, SPD methods allow straining without changing the sample's dimensions significantly after processing. Thus, continuous SPD processing can impose very high strains in a material. The severe deformation is associated with a pronounced increase in the dislocations density on the materials, and consequently, an expressive microstructural refinement [46, 47]. The development of an ultra-fine structure, in which grain sizes reach the submicrometric (< 1 μm) and nanometric (< 100 nm) range, leads to a pronounced improvement of the materials mechanical resistance, and in some cases, of corrosion resistance [48, 49].

SPD techniques include equal channel angular pressing (ECAP) [50, 51], high-pressure torsion (HPT) [52], accumulative roll-bonding (ARB) [53], twist extrusion

(TE) [54-56], friction-stir processing (FPS) [57-59] and multi-directional forging (MDF) [60, 61]. Other SPD techniques are described by Estrin and Vinogradov [46]. Common aspects of the process are the use of high pressures, the imposition of high strains, and the ability to repetitive or continuous processing, maintaining the workpiece geometry. The main differences between processes are related to dimensions of the samples, hydrostatic pressure, and efficiency in refining the microstructure.

In the last decades, SPD processes have emerged as powerful tools to fabricate metallic hybrids (i.e. lamellar structures, porous structures, reinforced composites) due to their capability of low-temperature solid-state densification under large shear strains [62, 63]. That is because the intense shear in the workpiece under elevated pressure can promote effective bonding of metallic materials due to the creation of new surfaces during processing. The hybrids can be fabricated through the following approaches: consolidating metallic particles (as powders or machined chips) [42, 64-69] or stacking and coprocessing bulk pieces together (as thin sheets, bars or discs) [70-76]. Examples of hybrids fabricated by SPD are presented in Figure 2.8.

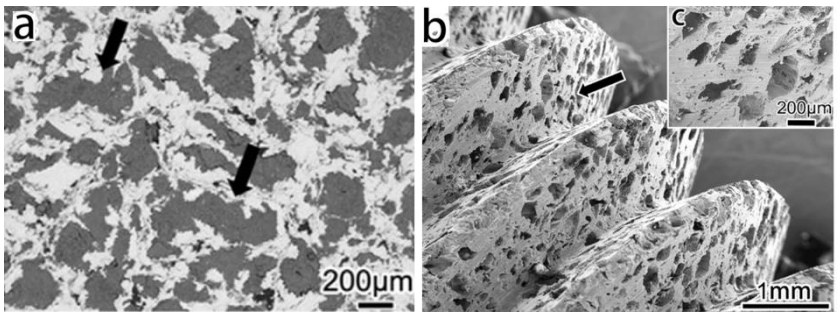

Figure 2.8 - (a) SEM of Ti/Mg/Si compact after 4 ECAP passes at 400°C; (b) Porous Ti hybrid fabricated by turning after removing the Si and Mg; (c) enlarged image of pores. Ref.[42]

Among the existing SPD processes developed so far, high-pressure torsion (HPT) is especially effective for bonding materials into a unique bulk piece. That is because HPT imposes larger hydrostatic pressure and continuous shear deformation on the processed sample, enabling the consolidation of metallic particles at room temperature and providing the most expressive grain refinement. Also, processing metallic mixtures by HPT promotes enhanced atomic diffusion, phase transformations, precipitation of intermetallics and mixing elements at the atomic scale, allowing to tailor unique hybrids with advanced functionalities [77]. Therefore, the HPT process is increasing its importance in the scientific community

to fabricate novel nanostructured hybrids with enhanced properties and open avenues for studying materials interactions, non-diffusional solid-state reactions, and strengthening mechanisms. Since consolidation is usually achieved at room temperature using a relatively short processing time, producing hybrids through HPT is an alternative that saves time and energy when compared to conventional fabrication techniques.

2.3. High-pressure torsion

2.3.1. Operational procedures

High-pressure torsion (HPT) is a well-known SPD technique in which a workpiece is subjected to torsional straining under high compressive hydrostatic stresses. A schematic illustration of the process is presented in Figure 2.9. The high imposed strains lead to the motion and multiplication of a high density of dislocations which evolve to grain boundaries, promoting substantial grain refinement even to the nanometer range [78, 79].

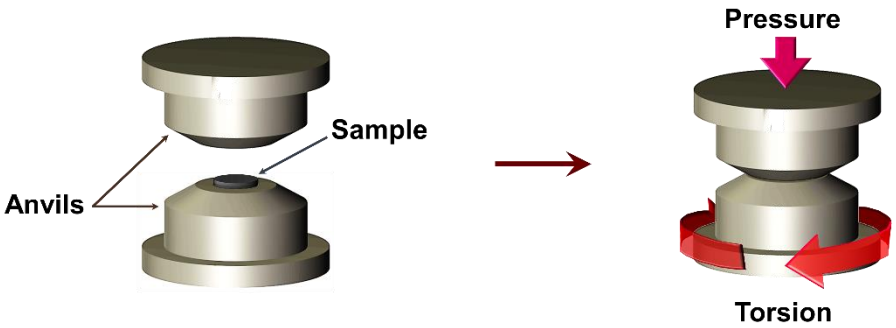

Figure 2.1 - Scheme of sample and anvils configuration in HPT processing.

The facility for HPT has two anvils vertically aligned in which one goes up and down, and the other can rotate around its axis. The workpiece is generally a solid disk, which is placed between the two anvils over the top surface of the lower one. The processing consists in, firstly, forcing one anvil against the other with the sample in between, establishing a certain pressure P at the sample, then secondly, an anvil starts to rotate until completing N revolutions twisting the sample under a constant angular velocity ω while the load is kept constant. The contact friction with the anvils forces the sample to deform.

The geometry of the anvils determines the outflow restriction that the processing sample will experiment. If the anvils are flat, the sample will experiment free lateral flow outwards and processes will be categorized as unconstrained. However, if the anvils present a cavity where the workpiece fits, it will restrict materials outflow during the torsional straining. Thus, the process will be categorized as constrained (if the anvil's cavity totally restricts any outward flow during) or quasi-constrained HPT (if the anvils have shallower cavities allowing a small amount of lateral flow between them). These conditions are illustrated in Figure 2.10.

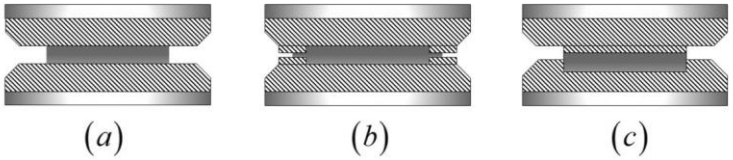

Figure 2.10 - A schematic view of the (a) unconstrained and (b and c) constrained HPT processing conditions [80].

Besides the HPT facilities to process disc samples (which dimensions go from 8 up to 60 mm diameter), some equipment can process small cylinders, rings or "u-shaped" samples [52, 81].

Typically, the HPT processing generally occurs at room temperature (RT) under quasi-constrained conditions and on disc samples with around 10 mm diameter. The pressure is in the order of 1 to 10 GPa and should be selected according to the material's strength to prevent slippage. The high compressive loads generate compressive stresses that effectively prevent cracking of the sample, enabling hard or even fragile materials to experiment a high plastic deformation in temperatures below the ones for usual processing. In fact, during deformation, some heat is generated not only by the plastic deformation itself but also by the friction between the sample and anvils. The temperature increase will be proportional to the materials strength and anvil's rotation speed [82, 83]. However, since the massive anvils are considerably bigger/heavier than the HPT samples, they act as heat sinks preventing significant temperature rise. The temperature increase will only be relevant when the sample size increases or if the rotation speed is not properly adjusted [81]. Accordingly, it is reasonable to assume that phases reactions and recrystallisation occurring during regular RT-HPT should not be triggered by thermal conditions.

Nevertheless, it is possible to implement either a liquid nitrogen cooling system or a heating system for the anvils, enabling to choose the processing temperature. For example, HPT was conducted at cryogenic temperature (-173°C) to process bulk samples of different pure metals [84] and to consolidate titanium and Ti-Al_2O_3 powders [85]. Moreover, graphene-reinforced Al-based composites were fabricated using high-pressure torsion at 100° and 200°C [86], while tungsten-cooper composites were HPT-processed at 200° and 400°C [87]. Also, SiO_2 powders were processed by HPT at 450°C [88].

2.3.2. Stress and strain distribution and the achievement of a steady-state

The stress distribution inside the sample is considerably heterogeneous, varying according to the distance from the sample's centre; the compressive stresses are higher in the centre and lower at the edge, while the shear strains on the edge are much higher than in the centre [89]. The imposed strain varies along with the radial distance according to the equivalent plastic strain (ε_{ef}) given by the relationship [52]:

$$\varepsilon_{\mathrm{ef}} = \frac{\gamma}{\sqrt{3}} = \frac{2\pi N.r}{h} \qquad \text{(Equation 3.1)}$$

where *N* is the number of revolutions, *r* is the radial distance from the sample's centre, *h* is the sample's thickness, and *γ* is the shear strain. Heterogeneities along the sample's thickness are also observed [81], but this effect is minimized in thin samples in which the radius to thickness ratio is large.

This heterogeneous distribution of strain influences microstructural refinement and mechanical properties across the samples, especially after a few turns. The evolution in mechanical strengthening and microstructure due to HPT processing can be seen in Figure 2.11 and Figure 2.12, respectively. The first shows the changes in hardness along HPT processed discs of two different Al alloys [90], while the last presents EBSD images of pure Ni subjected to different intensity of strains showing the effect in grain size [91].

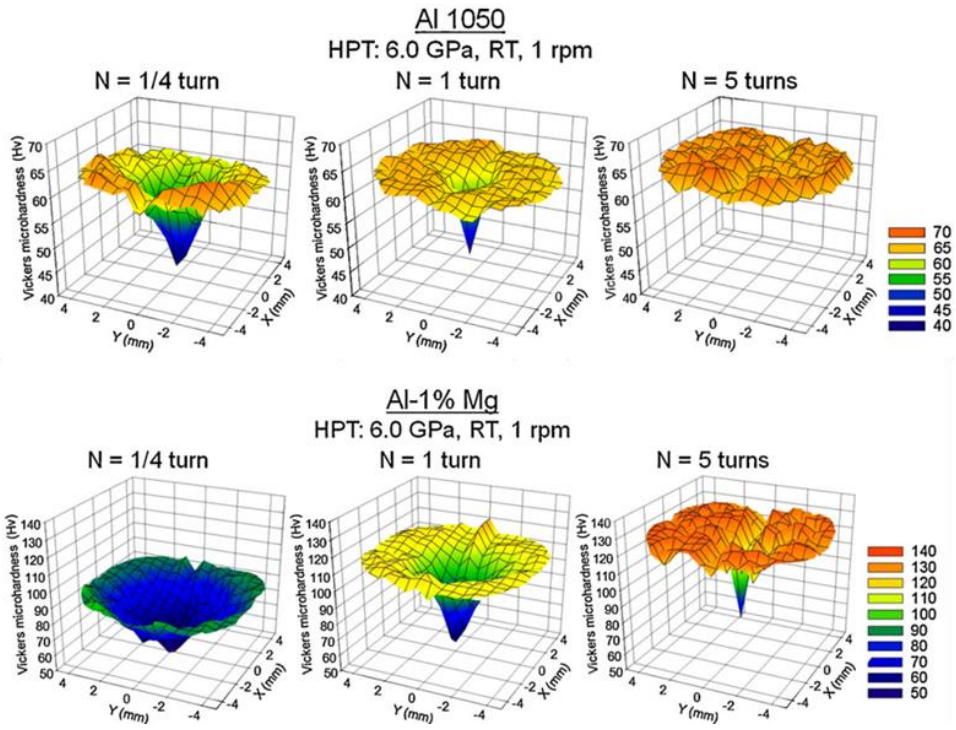

Figure 2.11 - Hardness distribution maps of HPT-processed Al alloys with different alloying content. Adapted from [90]

Although it is expected that regions that experiment higher strains (i.e., higher *r* or *N* values) present more refined grains and higher hardness values, homogeneous microstructures and hardness distributions are attained after a sufficient number of turns. This can be noticed in the Al alloys represented in Figure 2.11 when hardness tends to reach a constant value from edge to centre after a certain number of turns, and also in pure Ni in Figure 2.12, in which grain sizes remains essentially unchanged when the shear strain is increased from 16 to 32.

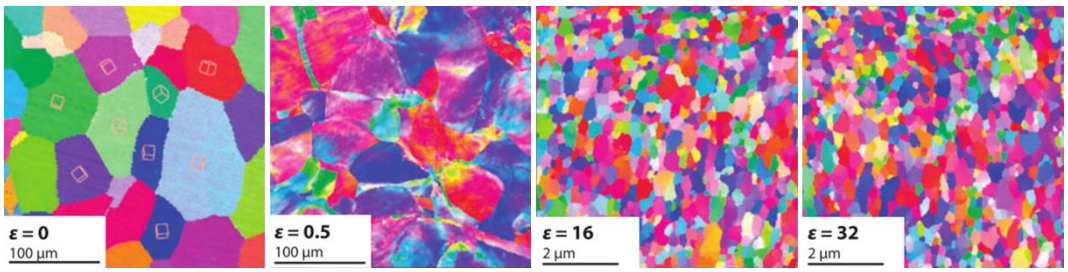

Figure 2.2 - EBSD of Ni HPT-deformed at room temperature. Adapted from [91]

It is important to note that alloying elements and second phase particles affect microstructure evolution during SPD and mechanical properties. Such effect can be observed in Figure 2.13 by comparing grain refinement in pure Ni, alloyed Ni and consolidated Ni (that will form an in-situ composite reinforced with Ni oxides)

subjected to HPT processing [91]. Alloying elements and fine disperse oxides promote a more intense strain hardening with HPT since they can hinder dislocations mobility. While alloying significantly reduces the grain structure size from approximately 200 nm in pure Ni to approximately 100 nm in a Ni-25% Fe alloy, grain sizes of about 10 nm to 30 nm can be observed in a Ni-NiO composite. The effect of dispersed NiO nanoparticles is reflected in an expressive increase in hardness from ~70 HV to ~690 HV [91, 92].

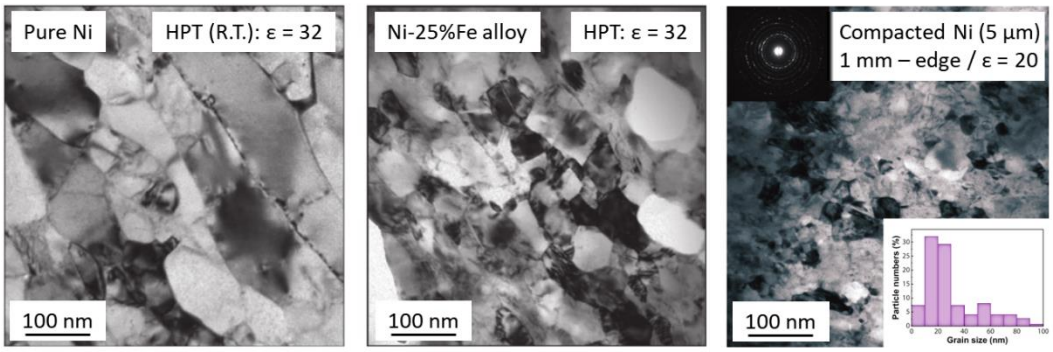

Figure 2.13 - saturation of grain refinement for pure bulk metal, alloy and compacted powder (in-situ composite). [91]

2.3.3. Consolidating particles by HPT

The high hydrostatic stresses and severe straining induced by HPT allows consolidation of particles, and a processing route is illustrated in Figure 2.14. Loose metallic particles are simply pre-compacted and then processed by HPT to obtain a fully consolidated disc.

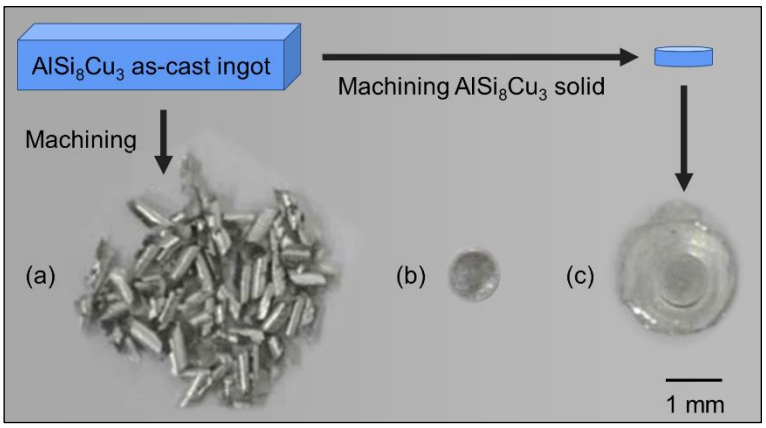

Figure 2.14 - Macrographs of the (a) as-machined chip, (b) cold compacted chip sample, and (c) HPT chip sample samples. Adapted from [67].

The imposition of high pressure and torsional strain on loose particles allows them to be consolidated through the following working principle: 1-shear deformation of each particle under high hydrostatic pressures increases the surface area of each particle; 2-the natural oxide layer at metallic particles surface must break during processing while the surface-to-area ratio grows significatively; 3-new oxide-free metallic surfaces are exposed and become available to be bonded. Besides, shearing and twisting promote a mechanical interlock of particles that favours an effective consolidation. Figure 2.15 illustrates this mechanism and compares it to the mechanism in conventional sintering.

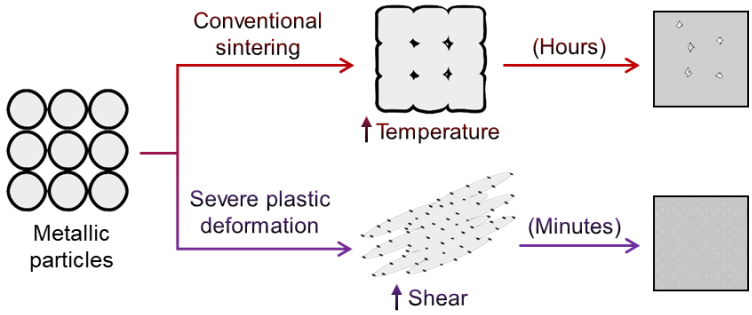

Figure 2.15 - Densification of metallic particles by shear-dependent process (SPD) or diffusion-dependent process (sintering). Adapted from [93].

Due to their high surface-to-volume ratio, ultra-fine metallic powders usually come with a considerable content of oxides on their surface. Consequently, their consolidation via HPT processing will result in an in-situ composite in which the reinforcement phase derives from their natural superficial oxidized layer, which is fractured, mixed, and entrapped within the metallic matrix. In room temperature processing, care must be taken to apply enough HPT revolutions to guarantee that most particles will deform rather than slid (so their oxidized layer can be effectively broken and clean metallic surface can be exposed to be bond). That will be determinant for achieving a successful consolidation throughout the sample. Having a certain amount of oxides during processing brings the advantage of local strain gradients caused by the difference in mechanical properties between the oxides and the metallic matrix, leading to higher deformation thus an intensive grain refinement. Additionally, fine oxides can pin dislocations and grain boundaries, contributing to strengthening the composite.

On the other hand, during the consolidation of coarse particles, the few oxides trapped in the matrix do not effectively act as reinforcement pinning enough grain

boundaries or promoting Orowan strengthening. Accordingly, saturation grain sizes and saturation hardness are usually not very different from those achieved in the bulk processed material.

The effect of oxides in smaller particles was evidenced in the research works of Panda *et al.* [62, 94] about consolidated Mg by HPT. In these research works, two different powder precursors are used, named nano-sized Mg powder (average particle size < 300 nm), presented in Figure 2.16, and micro-sized Mg powder (average particle size ~15 µm), presented in Figure 2.17. In the nano-HPT product, the densification was not completely achieved after 2 HPT turns. MgO was clearly identified by XRD. The oxide layers were sheared and fragmented into fine particles that got aligned along grain boundaries. Some parts of the microstructure present grains smaller than 100 nm. In the micro-HPT product, the average grain size of 0.5 to 1 µm was achieved. Although the presence of MgO is expected, its fraction is not enough to give rise to any XRD signal [94]. The effect of the initial particle size is then related to the amount of oxide in the consolidated product, which is strongly related to the final hardness achieved. The hardness of the nano-HPT sample (~108 HV) is considerably higher than that of the micro-HPT sample (~55 HV), which hardness is higher than in the processed bulk Mg [62]. It was suggested that the thin small oxides could pin grain boundaries and prevent recrystallisation.

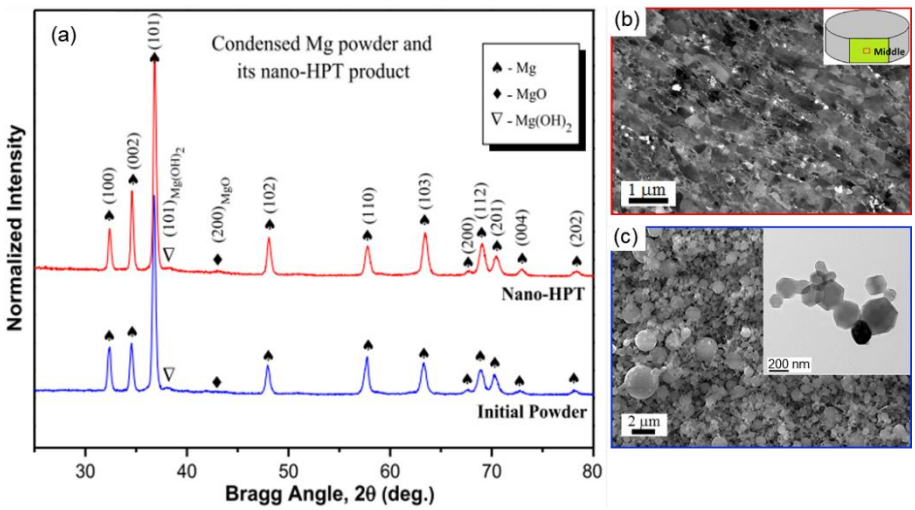

Figure 2.16 - Condensed and passivated ultrafine Mg powder and its nano-HPT product: (a) X-ray diffraction patterns; (b) MgO particles (white spots) in fine elongated domains with average thickness ~200-300 nm; (c) condensed powders before HPT. Adapted from [94].

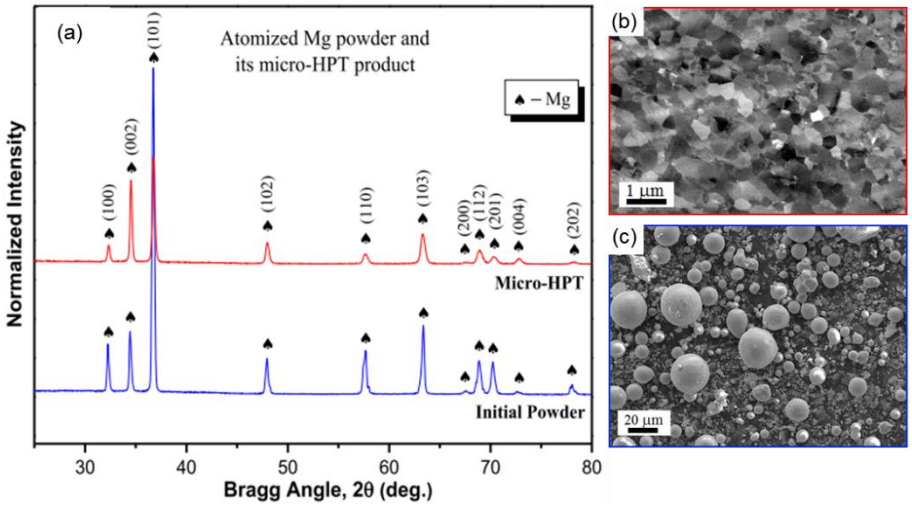

Figure 2.17 - Atomized micro-sized Mg powder and its micro-HPT product: (a) X-ray diffraction patterns; (b) microstructure after HPT: equiaxed dynamically recrystallized grains of ~0.5-1 µm; (c) atomized powders before HPT. Adapted from [94].

Despite the advantage of fabricating an in-situ composite and achieving finer microstructures, the consolidation of ultra-fine particles (or particles with a high surface-to-volume ratio) brings drawbacks as the difficulty of deforming all powders and the formation of clusters [92, 95]. Using coarser particles to produce these materials offers experimental advantages as being easy to handle and dispensing complex sample preparation. For a specific granulometry, a higher fraction of oxide (i.e. a thicker oxidized layer) can be achieved by thermal treatment. Figure 2.18 shows the hardness of Ni samples processed by HPT using different routes: processing of a bulk disc at R.T. and -196°C, or processing Ni powders which were subjected or not to thermal treatment to thick their oxidized layer. The oxidized powders achieved a higher hardness when compared to non-treated powders or bulk samples [92].

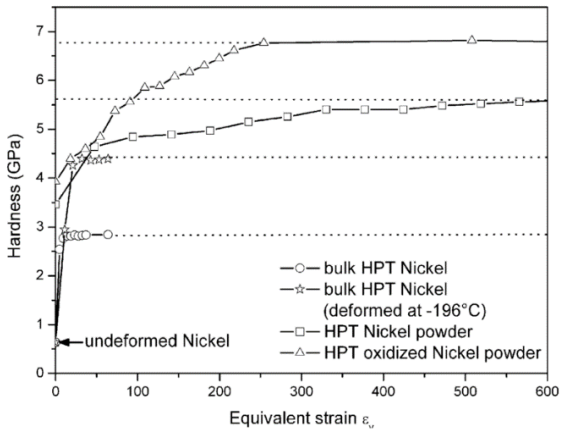

Figure 2.18 - Microhardness of HPT bulk Ni and HPT-consolidated samples of Ni powder (with and without oxidation treatment) as a function of the applied equivalent strain [92].

Besides having the option of producing an in-situ composite using oxidized particles, different phases can be added and blended to the particles before the HPT processing to fabricate a great variety of ex-situ reinforced composites or other hybrids. Evidence of this was presented by Jenei *et al.* [96] when coarse Cu powder and multi-walled CNTs were compacted and processed by HPT to fabricate pure consolidated Cu and Cu–CNT composites. It was shown that the grain size, the dislocation density and the hardness achieved in pure Cu samples by HPT-processing are not sensitive to the powder or bulk form of the initial coarse-grained material. Nevertheless, the reinforced composite presented great hardness (2.31 GPa), a fine microstructure (with an average grain size of about half of the unreinforced Cu), and an extremely high dislocation density of ~$110 \times 10^{14}\,m^{-2}$ (which is about three times larger than the one obtained in the unreinforced sample consolidated from pure Cu powder) due to the pinning effect of CNTs [96].

Thus, HPT processing enables designing nanostructured hybrids with a great variety of reinforcements since almost endless material combinations can be achieved by blending elemental powders [97]. It is possible to mix materials in different portions and inserting particles that are temperature sensitive or that would not mix well in a melting procedure. Taking advantage of that, a significant amount of research involving HPT assisted particles consolidation has been conducted on a wide range of material systems, such as metallic materials [69, 78, 98-101], metal-ceramic composites [78, 102-106], ceramic powders [107], and amorphous materials [108-113]. Specifically, many research papers report the consolidation of metallic particles by HPT (with or without the addition of an extra hard phase). Tables 2.1 to 2.4 present a summary of the fabrication of metallic hybrids by (mixing and) consolidating particles through HPT processing. It is worth noting that samples are usually small discs with ~10 mm diameter, and the most used processing parameters are a pressure of 6 GPa and 5 or 10 revolutions. Furthermore, it can be seen that copper-, aluminium-, and titanium-based systems have been systematically studied.

Table 2.1 - Summary of different metallic hybrids fabricated by particles consolidation through HPT processing, evidencing the system mixed (final composition of the hybrid), the initial particle size of the components, the diameter of HPT sample D [mm], number of turns N, average grain size d [nm], saturation hardness in higher strains and range of hardness reported.

Consolidated system	Particle size [μm]	D [mm]	P [GPa]	N	d [nm]	Hardness	Ref.
Al	Al 75 μm	20	2.5	-	~500	40-50 HV	[102, 103]
	Al ~150 μm	20	1.5	10	-	~50 (40-50) HV	[114]
	-	10	5	10	-	~87 HV	[115]
	Al ~150 nm	10	6	10	-	~30 (20-30) HV	[116]
	Al ~ 9 μm	10	6	5	-	(70-80) HV	[117]
Al-0.5% Nb_2O_5 (wt%)	Al ~9 μm	10	6	5- 10	-	65-125 HV	[117]
Al-1% Nb_2O_5 (wt%)	Al ~9 μm	10	6	5- 10	-	65-135 HV	[117]
Al-2% Nb_2O_5 (wt%)	Al ~9 μm	10	6	5- 10	-	70-125 HV	[117]
Al-3% Nb_2O_5 (wt%)	Al ~9 μm	10	6	5- 10	-	70-142 HV	[117]
Al-5% Nb_2O_5 (wt%)	Al ~9 μm	10	6	5- 10	-	70-145 HV	[117]
Al-10% Nb_2O_5 (wt%)	Al ~9 μm	10	6	5 -10	-	70-190 HV	[117]
Al-1% BNNT (wt%)*	*	10	5	10	-	~105 (105-110) HV	[115]
Al-3% BNNT (wt%)*	*	10	5	10	-	~135 (130-140) HV	[115]
Al-5% BNNT (wt%)*	*	10	5	10	-	~130 (115-145) HV	[115]
Al-5% fullerene (wt%)	Al 75 μm fullerenes (mix C60 + C70)	10	2.5	15	~80	39-118 HV	[103]
Al-5% GNP (wt%)	Al 125 μm	10	6	1 to 20	~70 to ~180	~110 HV (40-115) HV	[86]
Al-5% CNT (wt%)	Al 75 μm	10	2.5	30	~100	36 - 76 HV	[102]
Al-10% Al_2O_3 (vol%)	(Al ~ 150 μm, γ-Al_2O_3 ~30 nm) BM	20	1.5	10	-	~80 (45-80) HV	[114]
Al-20% Al_2O_3 (vol%)	(Al ~ 150 μm, γ-Al_2O_3 ~ 30 nm) BM	20	1.5	10	-	~125 (50-130) HV	[114]
Al-30% Al_2O_3 (vol%)	Al ~ 150 nm, γ-Al_2O_3 ~ 30 nm	10	6	10 to 50	550	65-128 HV	[116]
Al_{7050}-10% Al_2O_3 (vol%)	Al(7050) ~20-500 μm, Al_2O_3 ~1 μm	10	6	50	~50 to ~200	240 -300 HV	[118]
Al-10%Fe (wt%)	Al < 75 μm, Fe < 53 μm	-	6	1 to 75	145 to 1010	50-300 HV	[119]
$Al_{90}Fe_5Nd_5$	$Al_{90}Fe_5Nd_5$ alloy < 25 μm	10	5	-	-	3.1 ± 0.05 GPa	[108]
$Al_{90}Fe_7Z_3$	-	7	5	5	-	3.58 ± 0.15 GPa	[109]
$Al_{84}Y_3Ni_8Co_4Zr_1$+SiC	SiC 5-20 μm	7	5	5	-	4.6 ± 0.1 GPa	[109]

Consolidated system	Particle size [μm]	D [mm]	P [GPa]	N	d [nm]	Hardness	Ref.
Ti	Ti ≈ 21 μm	20	0.3 to 1.5	3	~75	-	[78]
	Ti < 45 μm	-	4	10 to 150	40 ± 25	376 ± 17 (356 – 399) HV	[120]
	Ti ≈ 150 μm	-	6	5	125-275	285-315 HV	[121]
Ti-0.3% CNT (wt%) **	Ti ≈ 20 μm	7.5	7.5	5 to 30	25-250	504 ± 15	[122]
Ti-0.5% CNT (wt%) **	Ti ≈ 20 μm	7.5	7.5	5 to 30	-	-	[122]
Ti-0.7% CNT (wt%) **	Ti ≈ 20 μm	7.5	7.5	5 to 30	-	400-595 MPa	[122]
Ti-1.0% CNT (wt%) **	Ti ≈ 20 μm	7.5	7.5	5 to 30	10-150	585 ± 10	[122]
Ti-5% TiO_2 (vol%) ***	Ti ≈ 21 μm, TiO_2 ~36 nm	20	1.5	3	~75	-	[78]
Ti-10% TiO_2 (vol%)	Ti ≈ 21 μm, TiO_2 ~36 nm	-	-	-	-	-	[78]
Ti-18% Al_2O_3 (vol%)	Ti ≈ 70 μm, α-Al_2O_3 ~1 μm	20	6	10	d_{Ti} ≈ 100; $d_{Al_2O_3}$ ≈ 400	350 HV	[123]
Ti-10% Nb (at%)	Ti < 45 μm, Nb < 45 μm	-	4	Up to 150	30 ± 22	387-432 (423 ± 1) HV	[120]
Ti-20% Nb (at%)	Ti < 45 μm, Nb < 45 μm	-	4	10 to 150	35 ± 36	313-380 (314 ± 1) HV	[120]
Ti-25% Nb (at%)	Ti < 45 μm, Nb < 45 μm	-	4	10 to 150	40 ± 20	~380 (378 -396) HV	[120]
Ti-35% Nb (at%)	Ti < 45 μm, Nb < 45 μm	-	4	10 to,150	35 ± 20	368 ± 10 HV	[120]
Ti-47% Al (at%)	-	-	6	1 5	~15-125	180-515 HV	[124]
Cu	-	-	-	-	~214	1.22 ± 0.04 GPa	[125]
	Cu ≈ 13 μm	20	10	15	950	190.9 HV	[126]
	Cu < 44 μm	20	2.5	10	174 ± 20	1.45-1.75 GPa	[96, 106]
	(machining chips)	-	6	5	308	1.59 – 1.81 GPa	[69]
	-	10	6	5	29	2.8-3.0 GPa	[127]
Cu-1% CNT (wt%)	Cu 0.5-1.5 μm	10	6	5	22	3.5-3.7 GPa	[127]
Cu-3% CNT (vol%)	Cu < 44 μm	20	2.5	10	74 ± 8 -	~2.12 GPa 1.25-2.25 GPa	[106] [96]
Cu-5% G (wt%)	-	20	1.5	4	-	2.14 ± 0.06 GPa	[125]
Cu-10% G (wt%)	-	20	1.5	4	~158	2.67 ± 0.08 GPa	[125]
Cu-0.5% NbC (vol%)	Cu ≤ 180 μm, Nb, C ≤ 10 μm	20	5	20	-	190 HV	[128]
Cu-1% NbC (vol%)	Cu ≤ 180 μm, Nb, C ≤ 10 μm	20	5	20	-	210 HV ~145 ± 3 HV	[128] [129]
Cu-2% NbC (vol%)	Cu ≤ 180 μm, Nb, C ≤ 10 μm	20	5	20	-	270 HV	[128]

Consolidated system	Particle size [μm]	D [mm]	P [GPa]	N	d [nm]	Hardness	Ref.
Cu-5% NbC (vol%)	Cu ≤ 180 μm, Nb, C ≤ 10 μm	20	5	20	-	310 HV ~250 ± 3 HV	[128] [129]
Cu-15% NbC (vol%)	Cu ≤ 180 μm, Nb, C ≤ 10 μm	20	1.25	10	-	191Hv – 367HV	[128]
Cu-10% SiC	Cu ≈ 13 μm, SiC ≈ 25.5 μm	10	10	15	90	276.1	[126, 130]
Cu-20% SiC	Cu ≈ 13 μm, SiC ≈ 25.5 μm	10	10	15	78	328.5	[126]
Cu-30% Cr_3C_2 (vol%)	-	-	6	1	poor bonding	4.4 GPa	[131]
Cu-14% Fe (wt%)	Cu: 34- 88 μm, Fe:74- 149 μm	-	5	100	-	1st ~150 HV, 2nd ~190 HV	[132]
Fe-0.4% C (wt%)	Fe ≈ 10 μm	10	6	2 to 50	~20	7.16-11.47 GPa	[133]
CoCrFeMnNi	Co, Cr, Fe, Mn, Ni < 10 μm	10	5	1, 10, 100		4-4-7.3 (6.75) GPa	[134]
Co	Co (Ball-milled) Co < 44 μm (unmilled) Co < 44 μm	-	6	5		7.35 GPa 4.3 GPa 5 GPa	[98] [98] [104, 105]
Co-5% Al_2O_3 (wt%)	Co < 44 μm	12	6	5		6 GPa	[104]
Co-10% Al_2O_3 (wt%)	Co < 44 μm	12	6	5		6.9 GPa	[104]
Co-20% Al_2O_3 (wt%)	Co < 44 μm	12	6	5		7.8 GPa	[104]
Co-30% Al_2O_3 (wt%)	Co < 44 μm	12	6	5		6.7 GPa	[104]
Co-40% Al_2O_3 (wt%)	Co < 44 μm	12	6	5		5.8 GPa	[104]
Co-50% Al_2O_3 (wt%)	Co < 44 μm	12	6	5		5.5 GPa	[104]
Co-NiO (50%wt)	Co < 44 μm, NiO < 100 μm		6	5		9 GPa	[105]
Ni	Ni 70-100 μm Ni 3-7 μm	8-14	2.5-6	$\varepsilon_V \approx 250$	- 29.8 ± 20.6	5.5 GPa 6.8 GPa	[92]
Mg	-	20	1.2	2	-	-	[62]
Mg-MgO****	Mg 50-600 nm	20	0.4	2	~45	70 HV	[135]
Mg-Zr (50%at)	Mg, Zr < 44 μm	14	1.5 3	1 to 1000 1 to 1200	40 ± 30	~80 to 145 HV	[136] [137]

*Notes: *BNNT: Boron nitride nanotube - BNNT external diameter of 30-50 nm and a length of up to dozens of micrometres; Nb_2O_5 diameter of 7-10 nm; GNP = Graphene nanoplates; **CNT: multi-walled carbon nanotubes, diameter ~6-13 nm, length ~2.5-20 μm; ***HPT processing at 450ºC [78]; ****MgO comes from the natural oxidized Mg, MgO layer is 1-2 nm thick.*

2.3.4. Fabricating hybrids from metallic mixtures

Some papers present the potential of HPT for leading to greater grain refinement and higher hardness when different metallic systems are mixed, enabling solid-state reactions as phase transformation, precipitation of intermetallics or solubilisation of phases. The deformation process of the particles is complex and will vary according to materials mechanical characteristics. Kormout *et al.* [97] studied series of composites produced by the consolidation of metallic particles and compared the microstructural evolution with the increasing strain with the final hardness achieved by the hybrid. They observed that the structure and hardness evolution depend not only on the phases present but also on the difference in strength between the phases. They proposed the model depicted in Figure 2.19 to explain the basic features of structure and hardness evolution [97]. Basically, it was reported that the phases with either fragment or co-deform according to the difference in mechanical resistance among the second phase and the matrix. The initial arrangement of phases plays a key role in composites because geometrical changes dominate the microstructural evolution and the deformation behaviour [97]. The volume fraction and mechanical properties of the constituent phases determine if co-deformation or predominant fracture of hard phases and localised plastic deformation of soft phases are the dominating deformation processes.

Although it is possible to promote an effective mechanical mixing by HPT, enormous strains are required to achieve this condition in atomic scales. The process that leads to effective solubilisation of phases is complex due to the difference in materials properties such as hardness, shear resistance, ductility, and effective viscosity [97, 138-140], leading to mechanical instabilities throughout the sample. Such mechanical instabilities will act localising the deformation in specific regions and creating vortex structures, postponing the homogenisation of the microstructure. However, in a certain strain, the chunks of metals start to thinner progressively. The finer the phases get, the more favourable is the occurrence of solubilisation of thermodynamically immiscible elements. At the same time, as presented in Figure 2.19, a significant increase of hardness can be achieved due to the co-presence of two immiscible phases since it also diminishes the occurrence of dynamic recrystallisation or grain boundary migration

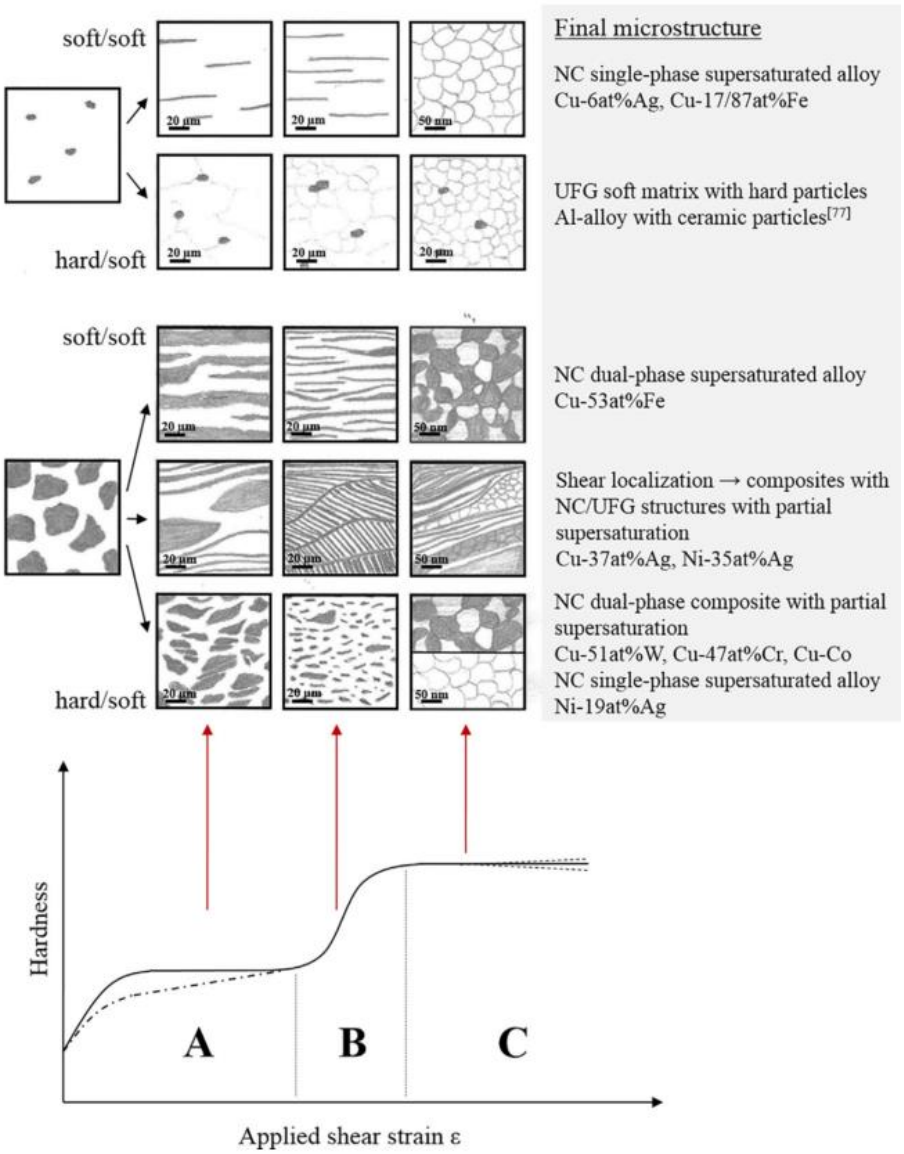

Figure 2.19 - Schematic of the microstructural and hardness evolution as a function of applied strain depending on hardness differences and volume fraction of the constituent phases [97].

Edalati et al. [136] fabricated a Mg-Zr hybrid by consolidating elemental powders of Mg and Zr and processing the blend by HPT up to 1000 turns. Although Mg and Zr are thermodynamically immiscible in each other, a supersaturated solid solution occurred by mechanical alloying, and several metastable nanostructured phases are formed. Figure 2.20 shows the appearance of the different phases after a different number of turns. It is observed that a very large number of turns is required to promote effective mixing of the elements.

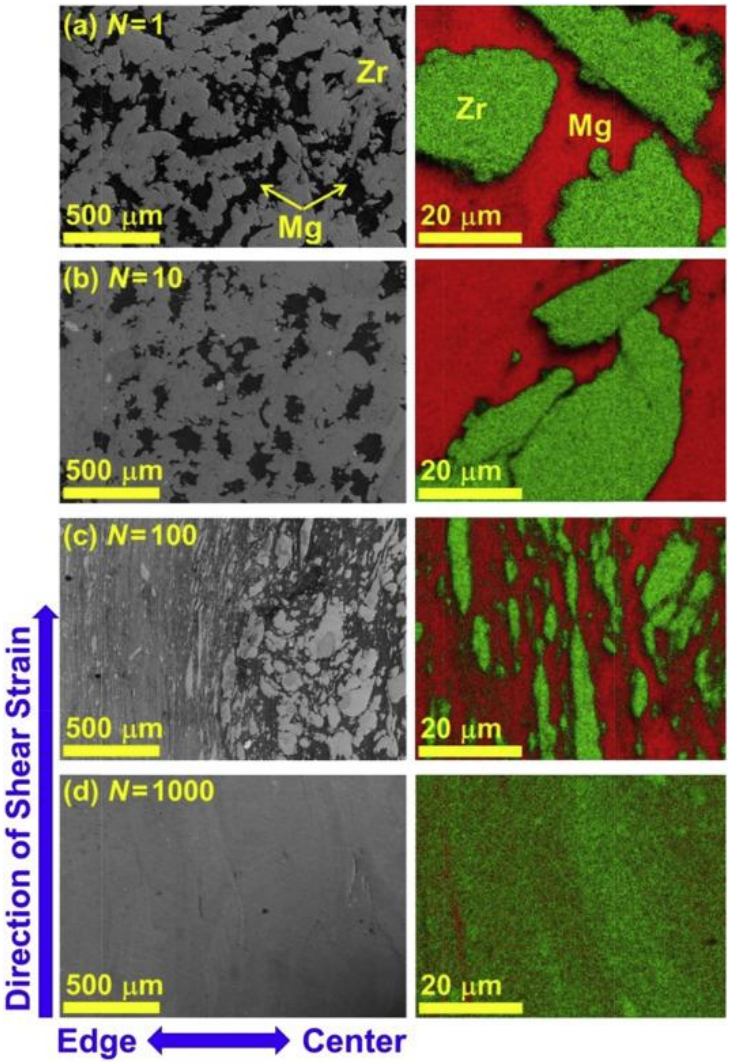

Figure 2.20 - SEM micrographs (left) and EDS mapping (right) from the Mg-Zr hybrids processed by HPT at RT for (a) N = 1, (b) N = 10, (c) N = 100, and (d) N = 1000 turns. [136]

2.4. References

1. Morishige, T., et al., Effect of Impurity Fe Concentration on the Corrosion Behavior of Mg-14 mass% Li-1 mass% Al Alloy. Materials Transactions, 2014. **55**(9): p. 1506-1509.
2. Alaneme, K.K. and E.A. Okotete, Enhancing plastic deformability of Mg and its alloys—A review of traditional and nascent developments. Journal of magnesium and alloys, 2017. **5**(4): p. 460-475.
3. Yang, Z., et al., Review on Research and Development of Magnesium Alloys. Acta Metallurgica Sinica (English Letters), 2008. **21**(5): p. 313-328.
4. Froes, F.H., D. Eliezer, and E. Aghion, The science, technology, and applications of magnesium. JOM, 1998. **50**(9): p. 30-34.
5. Material selection and processing. 02/25/2002 [cited 2018 05/22]; Material Selection Charts]. Available from: http://www-materials.eng.cam.ac.uk/mpsite/interactive_charts/default.html.
6. Sillekens, W.H., et al., The ExoMet project: EU/ESA research on high-performance light-metal alloys and nanocomposites. Vol. 45. 2014. 1-13.
7. AGENCY, E.S. Final Report Summary - EXOMET (Physical processing of molten light alloys under the influence of external fields). 2018-02-05 [cited 2018 2018-05-30]; Available from: https://cordis.europa.eu/result/rcn/218648_en.html.
8. GMBH, E.D. Final Report Summary - AEROMAG (Aeronautical application of wrought magnesium). 2011-04-14 [cited 2018 2018-05-30]; Available from: https://cordis.europa.eu/result/rcn/52107_en.html.
9. GMBH, R. Final Report Summary - IDEA (Integrated design and product development for the eco-efficient production of low-weight aeroplane equipment). 2011-04-14 [cited 2018 2018-05-30]; Available from: https://cordis.europa.eu/result/rcn/47872_en.html.
10. Bettles, C. and M. Gibson, Current wrought magnesium alloys: Strengths and weaknesses. JOM, 2005. **57**(5): p. 46-49.
11. Dziubińska, A., et al., THE FORMING OF MAGNESIUM ALLOY FORGINGS FOR AIRCRAFT AND AUTOMOTIVE APPLICATIONS. Advances in Science and Technology Research Journal, 2016. **10**(31): p. 158-168.
12. Luo, A.A., Magnesium casting technology for structural applications. Journal of Magnesium and Alloys, 2013. **1**(1): p. 2-22.
13. Mordike, B.L. and T. Ebert, Magnesium: Properties — applications — potential. Materials Science and Engineering: A, 2001. **302**(1): p. 37-45.

14. Kujur, M.S., et al., Enhancement of thermal, mechanical, ignition and damping response of magnesium using nano-ceria particles. Ceramics International, 2018.

15. Bowen, P.K. and W.H. Sillekens, Overview: Magnesium-Based Biodegradable Implants. JOM, 2016. **68**(4): p. 1175-1176.

16. Henderson, S.E., et al., Magnesium alloys as a biomaterial for degradable craniofacial screws. Acta Biomaterialia, 2014. **10**(5): p. 2323-2332.

17. Pogorielov, M., et al., Magnesium-based biodegradable alloys: Degradation, application, and alloying elements. Interventional Medicine & Applied Science, 2017. **9**(1): p. 27-38.

18. Kuśnierczyk, K. and M. Basista, Recent advances in research on magnesium alloys and magnesium–calcium phosphate composites as biodegradable implant materials. Journal of Biomaterials Applications, 2016. **31**(6): p. 878-900.

19. Brar, H.S., et al., Magnesium as a biodegradable and bioabsorbable material for medical implants. JOM, 2009. **61**(9): p. 31-34.

20. Köhler, N.M.S., J. M.; Forssmann, K.; Kirschner, M. H., Magnesium-based implants: indications and results, in AitogOggi. 2020, Periodico dell'Associazione Italiana di Traumatologia ed Ortopedia Geriatrica. p. 62-67.

21. Erbel, R., et al., Temporary scaffolding of coronary arteries with bioabsorbable magnesium stents: a prospective, non-randomised multicentre trial. The Lancet, 2007. **369**(9576): p. 1869-1875.

22. Rich, M., G. Ridgley, and D. Lowry, Application of composites to helicopter airframe and landing gear structures. 1973.

23. Ashby, M.F., Hybrids to fill holes in material property space. Philosophical Magazine, 2005. **85**(26-27): p. 3235-3257.

24. Ashby, M.F. and Y.J.M. Bréchet, Designing hybrid materials. Acta Materialia, 2003. **51**(19): p. 5801-5821.

25. Hardaker, K.M. and M.O.W. Richardson, Trends in Hybrid Composite Technology. Polymer-Plastics Technology and Engineering, 1980. **15**(2): p. 169-182.

26. Zweben, C., Tensile strength of hybrid composites. Journal of Materials Science, 1977. **12**(7): p. 1325-1337.

27. Eacherath, S. and S. Murugesan, Synthesis and characterization of magnesium-based hybrid composites – A review. International Journal of Materials Research, 2018. **109**(7): p. 661-672.

28. Khanra, A.K., et al., Comparative property study on extruded Mg–HAP and ZM61–HAP composites. Materials Science and Engineering: A, 2010. **527**(23): p. 6283-6288.

29. Khanra, A.K., et al., Microstructure and mechanical properties of Mg-HAP composites. Vol. 33. 2010, Bulletin of Materials Science. 43-47.

30. Ye, X., et al., In vitro corrosion resistance and cytocompatibility of nano-hydroxyapatite reinforced Mg–Zn–Zr composites. Journal of Materials Science: Materials in Medicine, 2010. **21**(4): p. 1321-1328.

31. Sun, J.e., et al., The effect of nano-hydroxyapatite on the microstructure and properties of Mg–3Zn–0.5 Zr alloy. Journal of Composite Materials, 2014. **48**(7): p. 825-834.

32. Rahmany-Gorji, R., A. Alizadeh, and H. Jafari, Microstructure and mechanical properties of stir cast ZX51/Al2O3p magnesium matrix composites. Materials Science and Engineering: A, 2016. **674**: p. 413-418.

33. Aatthisugan, I., A. Razal Rose, and D. Selwyn Jebadurai, Mechanical and wear behaviour of AZ91D magnesium matrix hybrid composite reinforced with boron carbide and graphite. Journal of Magnesium and Alloys, 2017. **5**(1): p. 20-25.

34. Sankaranarayanan, S., et al., Microstructural evolution and mechanical properties of Mg composites containing nano-B4C hybridized micro-Ti particulates. Materials Chemistry and Physics, 2014. **143**(3): p. 1178-1190.

35. Setyadi, I., et al., Microstructure and microhardness of carbonate apatite particle-reinforced Mg composite consolidated by warm compaction for biodegradable implant application. Materials Research Express, 2020.

36. Salleh, E.M., et al., In Vitro Biodegradation and Mechanical Properties of Mg-Zn Alloy and Mg-Zn-Hydroxyapatite Composite Produced by Mechanical Alloying for Potential Application in Bone Repair. Metallurgical and Materials Transactions A, 2018. **49**(11): p. 5888-5903.

37. Jaiswal, S., et al., Mechanical, corrosion and biocompatibility behaviour of Mg-3Zn-HA biodegradable composites for orthopaedic fixture accessories. Journal of the Mechanical Behavior of Biomedical Materials, 2018. **78**: p. 442-454.

38. Stüpp, C.A., et al. Powder Metallurgical Synthesis of Biodegradable Mg-Hydroxyapatite Composites for Biomedical Applications. Trans Tech Publ.

39. Wan, Y., et al., Mechanical and biological properties of bioglass/magnesium composites prepared via microwave sintering route. Materials & Design, 2016. **99**: p. 521-527.

40. Xiong, G., et al., Characterization of biomedical hydroxyapatite/magnesium composites prepared by powder metallurgy assisted with microwave sintering. Current Applied Physics, 2016. **16**(8): p. 830-836.

41. Ratna Sunil, B., et al., Processing and mechanical behavior of lamellar structured degradable magnesium–hydroxyapatite implants. Journal of the Mechanical Behavior of Biomedical Materials, 2014. **40**: p. 178-189.

42. Qi, Y., et al., Ultrafine-grained porous titanium and porous titanium/magnesium composites fabricated by space holder-enabled severe plastic deformation. Materials Science and Engineering: C, 2016. **59**: p. 754-765.

43. Torabi, H., et al., Microstructure, mechanical properties and bio-corrosion properties of Mg-HA bionanocomposites fabricated by a novel severe plastic deformation process. Ceramics International, 2020. **46**(3): p. 2836-2844.

44. Lu, D., Y. Jiang, and R. Zhou, Wear performance of nano-Al2O3 particles and CNTs reinforced magnesium matrix composites by friction stir processing. Wear, 2013. **305**(1): p. 286-290.

45. Azizieh, M., et al., Fabrication of Mg/Al12Mg17 in-situ surface nanocomposite via friction stir processing. Materials Science and Engineering: A, 2018. **712**: p. 655-662.

46. Estrin, Y. and A. Vinogradov, Extreme grain refinement by severe plastic deformation: A wealth of challenging science. Acta Materialia, 2013. **61**(3): p. 782-817.

47. Valiev, R.Z., et al., Producing bulk ultrafine-grained materials by severe plastic deformation. JOM, 2006. **58**(4): p. 33-39.

48. Silva, C.L.P., et al., Effect of severe plastic deformation on the biocompatibility and corrosion rate of pure magnesium. Journal of Materials Science, 2017. **52**(10): p. 5992-6003.

49. Lopes, D.R., et al., Cytotoxicity and Corrosion Behavior of Magnesium and Magnesium Alloys in Hank's Solution after Processing by High-Pressure Torsion. Advanced Engineering Materials, 2019. **21**(8): p. 1900391.

50. Figueiredo, R.B., P.R. Cetlin, and T.G. Langdon, The processing of difficult-to-work alloys by ECAP with an emphasis on magnesium alloys. Acta Materialia, 2007. **55**(14): p. 4769-4779.

51. Valiev, R.Z. and T.G. Langdon, Principles of equal-channel angular pressing as a processing tool for grain refinement. Progress in Materials Science, 2006. **51**(7): p. 881-981.

52. Zhilyaev, A.P. and T.G. Langdon, Using high-pressure torsion for metal processing: Fundamentals and applications. Progress in Materials Science, 2008. **53**(6): p. 893-979.

53. del Valle, J.A., M.T. Pérez-Prado, and O.A. Ruano, Accumulative roll bonding of a Mg-based AZ61 alloy. Materials Science and Engineering: A, 2005. **410-411**: p. 353-357.

54. Jahedi, M. and M.H. Paydar, Study on the feasibility of the torsion extrusion (TE) process as a severe plastic deformation method for consolidation of Al powder. Materials Science and Engineering: A, 2010. **527**(20): p. 5273-5279.

55. Beygelzimer, Y., et al., Twist Extrusion as a Potent Tool for Obtaining Advanced Engineering Materials: A Review Advanced Engineering Materials, 2017. **19**(8): p. 1600873.

56. Mohammed Iqbal, U., S. Muralidharan, and P.V. Abhishek, Experimental studies on magnesium metal matrix composites processed by Twist Extrusion. IOP Conference Series: Materials Science and Engineering, 2020. **912**: p. 032055.

57. Yang, Q., et al., Influence of texture on superplastic behavior of friction stir processed ZK60 magnesium alloy. Materials Science and Engineering: A, 2012. **556**: p. 671-677.

58. Arokiasamy, S. and B. Anand Ronald, Experimental investigations on the enhancement of mechanical properties of magnesium-based hybrid metal matrix composites through friction stir processing. The International Journal of Advanced Manufacturing Technology, 2017. **93**(1): p. 493-503.

59. Luo, X., et al., Ductility improvement of an AZ61 magnesium alloy through two-pass submerged friction stir processing. Materials, 2017. **10**(3): p. 253.

60. Ansarian, I., et al., Microstructure evolution and mechanical behaviour of severely deformed pure titanium through multi directional forging. Journal of Alloys and Compounds, 2019. **776**: p. 83-95.

61. Huang, H. and J. Zhang, Microstructure and mechanical properties of AZ31 magnesium alloy processed by multi-directional forging at different temperatures. Materials Science and Engineering: A, 2016. **674**: p. 52-58.

62. Panda, S., et al., Effect of Strain Heterogeneities on Microstructure, Texture, Hardness, and H-Activation of High-Pressure Torsion Mg Consolidated from Different Powders. Materials (Basel, Switzerland), 2018. **11**(8): p. 1335.

63. Bazarnik, P., et al., Superior strength of tri-layered Al–Cu–Al nano-composites processed by high-pressure torsion. Journal of Alloys and Compounds, 2020. **846**: p. 156380.

64. Rezaei, M.R., S.H. Razavi, and S.G. Shabestari, Development of a novel Al–Cu–Ti metallic glass reinforced Al matrix composite consolidated through equal channel angular pressing (ECAP). Journal of Alloys and Compounds, 2016. **673**: p. 17-27.

65. Ramesh Kumar, S., et al., Effect of Mechanically Alloyed Graphene-Reinforced Aluminium by Equal Channel Angular Pressing (ECAP). Transactions of the Indian Institute of Metals, 2019. **72**(6): p. 1437-1441.

66. Casati, R., et al., ECAP consolidation of Al matrix composites reinforced with in-situ γ-Al2O3 nanoparticles. Materials Science and Engineering: A, 2015. **648**: p. 113-122.

67. Abd El Aal, M.I.Y.Y., Eun; Seop Kim, Hyoung., Recycling of AlSi8Cu3 alloy chips via high pressure torsion. Materials Science and Engineering: A, 2013. **560**: p. 121-128.

68. Khajouei-Nezhad, M., et al., Microstructure and Tensile Behavior of Al7075/Al Composites Consolidated from Machining Chips Using HPT: A Way of Solid-State Recycling. Metals and Materials International, 2019.

69. Zhilyaev, A.P.G., A.A.; Raab, G.I.; Langdon, T.G., Using high-pressure torsion for the cold-consolidation of copper chips produced by machining. Materials Science and Engineering: A, 2008. **486**(1): p. 123-126.

70. Anne, G., et al., Development and properties evaluation of Mg–6% Zn/Al multilayered composites processed by accumulative roll bonding. Journal of Materials Research, 2017. **32**(12): p. 2249-2257.

71. de Andrade Mendes Filho, A., et al., Interface Formation in Copper-Steel Multilayered Sheets under Severe Shear Strain. Advanced Engineering Materials, 2019. **21**(7): p. 1900029.

72. Medvedev, A.E., et al., Shear-induced, solid-state joining of Ti-6Al-4V and Ti17 titanium alloys. Materials Science and Engineering: A, 2018. **737**: p. 253-264.

73. Mendes, A., et al., Role of shear in interface formation of aluminium-steel multilayered composite sheets. Materials Science and Engineering: A, 2017. **705**: p. 142-152.

74. Ebrahimi, S.H.S., et al., Investigation on microstructure and mechanical properties of Al/Al-Zn-Mg–Cu laminated composite fabricated by accumulative roll bonding (ARB) process. Materials Science and Engineering: A, 2018. **718**: p. 311-320.

75. Wu, K., et al., Microstructure and mechanical properties of the Mg/Al laminated composite fabricated by accumulative roll bonding (ARB). Materials Science and Engineering: A, 2010. **527**(13): p. 3073-3078.

76. Beygelzimer, Y., et al., Vortex flow in twist extrusion. 2015.

77. Edalati, K., et al., Formation of metastable phases in magnesium–titanium system by high-pressure torsion and their hydrogen storage performance. Acta Materialia, 2015. **99**: p. 150-156.

78. Stolyarov, V.V., et al., Processing nanocrystalline Ti and its nanocomposites from micrometer-sized Ti powder using high pressure torsion. Materials Science and Engineering: A, 2000. **282**(1): p. 78-85.

79. Kawasaki, M. and T. Langdon, Review: achieving superplasticity in metals processed by high-pressure torsion. Journal of Materials Science, 2014. **49**(19): p. 6487-6496.

80. Marina Borodachenkova, Wei Wen, and A.M.d.B. Pereira, High-Pressure Torsion: Experiments and Modeling, in Severe Plastic Deformation Techniques, M. Cabibbo, Editor. 2017, IntechOpen.

81. Hohenwarter, A. and R. Pippan, Sample Size and Strain-Rate-Sensitivity Effects on the Homogeneity of High-Pressure Torsion Deformed Disks. Metallurgical and Materials Transactions A, 2019. **50**(2): p. 601-608.

82. Figueiredo, R.B., et al., Using finite element modeling to examine the temperature distribution in quasi-constrained high-pressure torsion. Acta Materialia, 2012. **60**(6): p. 3190-3198.

83. Pereira, P.H., et al., Modeling the temperature rise in high-pressure torsion. Vol. 593. 2014. 185-188.

84. Edalati, K., et al., Influence of severe plastic deformation at cryogenic temperature on grain refinement and softening of pure metals: Investigation using high-pressure torsion. Materials Science and Engineering: A, 2014. **613**: p. 103-110.

85. Edalati, K., et al., High-pressure torsion of titanium at cryogenic and room temperatures: Grain size effect on allotropic phase transformations. Acta Materialia, 2014. **68**: p. 207-213.

86. Huang, Y., et al., The fabrication of graphene-reinforced Al-based nanocomposites using high-pressure torsion. Acta Materialia, 2019. **164**: p. 499-511.

87. Sabirov, I. and R. Pippan, Formation of a W–25%Cu nanocomposite during high pressure torsion. Scripta Materialia, 2005. **52**(12): p. 1293-1298.

88. Wang, Q., et al., High-pressure torsion of SiO2 quartz sand: Phase transformation, optical properties, and significance in geology. Journal of the American Ceramic Society, 2020. **103**(11): p. 6594-6602.

89. Xu, C., Z. Horita, and T.G. Langdon, The evolution of homogeneity in processing by high-pressure torsion. Acta Materialia, 2007. **55**(1): p. 203-212.

90. Kawasaki, M., et al., The development of hardness homogeneity in pure aluminum and aluminum alloy disks processed by high-pressure torsion. Materials Science and Engineering: A, 2011. **529**: p. 345-351.

91. Pippan, R., et al., Saturation of Fragmentation During Severe Plastic Deformation. Annual Review of Materials Research, 2010. **40**(1): p. 319-343.

92. Bachmaier, A., A. Hohenwarter, and R. Pippan, New procedure to generate stable nanocrystallites by severe plastic deformation. Scripta Materialia, 2009. **61**(11): p. 1016-1019.

93. Castro, M.M.d. and R.B. Figueiredo. O uso de deformação plástica severa para a fabricação de compósitos de matriz metálica. in Congresso de Engenharia da Rede PDIMat. 2020. Online: Brasil.

94. Panda, S., et al., Effect of initial powder type on the hydrogen storage properties of high-pressure torsion consolidated Mg. International Journal of Hydrogen Energy, 2017. **42**(35): p. 22438-22448.

95. Xia, K., Consolidation of Particles by Severe Plastic Deformation: Mechanism and Applications in Processing Bulk Ultrafine and Nanostructured Alloys and Composites. Advanced Engineering Materials, 2010. **12**(8): p. 724-729.

96. Jenei, P., et al., Microstructure and hardness of copper–carbon nanotube composites consolidated by High Pressure Torsion. Materials Science and Engineering: A, 2011. **528**(13): p. 4690-4695.

97. Kormout, K.S., R. Pippan, and A. Bachmaier, Deformation-Induced Supersaturation in Immiscible Material Systems during High-Pressure Torsion Advanced Engineering Materials, 2017. **19**(4).

98. Sort, J., et al., Microstructural effects and large microhardness in cobalt processed by high pressure torsion consolidation of ball milled powders. Acta Materialia, 2003. **51**(20): p. 6385-6393.

99. Lee, Z., et al., Microstructure and microhardness of cryomilled bulk nanocrystalline Al–7.5%Mg alloy consolidated by high pressure torsion. Scripta Materialia, 2004. **51**(3): p. 209-214.

100. Jenei, P., et al., X-ray diffraction study on the microstructure of a Mg–Zn–Y alloy consolidated by high-pressure torsion. Journal of Alloys and Compounds, 2012. **539**: p. 32-35.

101. Yoon, E.Y., et al., Microstructures and mechanical properties of Mg–Zn–Y alloy consolidated from gas-atomized powders using high-pressure torsion. Journal of Materials Science, 2012. **47**(20): p. 7117-7123.

102. Tokunaga, T., K. Kaneko, and Z. Horita, Production of aluminum-matrix carbon nanotube composite using high pressure torsion. Materials Science and Engineering: A, 2008. **490**(1): p. 300-304.

103. Tokunaga, T., et al., Microstructure and mechanical properties of aluminum–fullerene composite fabricated by high pressure torsion. Scripta Materialia, 2008. **58**(9): p. 735-738.

104. Menéndez, E., et al., Cold Consolidation of Metal–Ceramic Nanocomposite Powders with Large Ceramic Fractions. Advanced Functional Materials, 2008. **18**(20): p. 3293-3298.

105. Menéndez, E., et al., Cold compaction of metal–ceramic (ferromagnetic–antiferromagnetic) composites using high pressure torsion. Journal of Alloys and Compounds, 2007. **434-435**: p. 505-508.

106. Jenei, P., et al., High temperature thermal stability of pure copper and copper–carbon nanotube composites consolidated by High Pressure Torsion. Composites Part A: Applied Science and Manufacturing, 2013. **51**: p. 71-79.

107. Edalati, K. and Z. Horita, Application of high-pressure torsion for consolidation of ceramic powders. Scripta Materialia, 2010. **63**(2): p. 174-177.

108. Yavari, A.R., et al., Nanostructured bulk Al90Fe5Nd5 prepared by cold consolidation of gas atomised powder using severe plastic deformation. Scripta materialia, 2002. **46**(10): p. 6.

109. Botta Filho, W.J., et al., Consolidation of partially amorphous aluminium-alloy powders by severe plastic deformation. Materials Science and Engineering: A, 2004. **375-377**: p. 936-941.

110. Czeppe, T., et al., Microstructure and properties of cold consolidated amorphous ribbons from (NiCu)ZrTiAlSi alloys. Journal of Alloys and Compounds, 2009. **483**(1): p. 74-77.

111. Boucharat, N., et al., Synthesis routes for controlling the microstructure in nanostructured Al88Y7Fe5 alloys. Journal of Alloys and Compounds, 2007. **434-435**: p. 252-254.

112. Kovács, Z., et al., Deformation induced primary crystallization in a thermally non-primary crystallizing amorphous Al85Ce8Ni5Co2 alloy. Scripta Materialia, 2006. **54**(10): p. 1733-1737.

113. Sort, J., et al., Cold-consolidation of ball-milled Fe-based amorphous ribbons by high pressure torsion. Scripta Materialia, 2004. **50**(9): p. 1221-1225.

114. Edalati, K., et al., Wear resistance and tribological features of pure aluminum and Al–Al2O3 composites consolidated by high-pressure torsion. Wear, 2014. **310**(1): p. 83-89.

115. Xue, Y., et al., Aluminum matrix composites reinforced with multi-walled boron nitride nanotubes fabricated by a high-pressure torsion technique. Materials & Design, 2015. **88**: p. 451-460.

116. Ashida, M., et al., Production of Al/Al2O3 Nanocomposites through Consolidation by High-Pressure Torsion. MATERIALS TRANSACTIONS, 2012. **53**(1): p. 13-16.

117. Silva, C., et al., Interface structures in Al-Nb2O5 nanocomposites processed by high-pressure torsion at room temperature. Materials Characterization, 2020. **162**: p. 110222.

118. Milhorato, F.R., et al., Development of an Al 7050-10 vol.% alumina nanocomposite through cold consolidation of particles by high-pressure torsion. Journal of Materials Research and Technology, 2020. **9**(6): p. 12626-12633.

119. Cubero-Sesin, J.M. and Z. Horita, Powder consolidation of Al–10wt% Fe alloy by High-Pressure Torsion. Materials Science and Engineering: A, 2012. **558**: p. 462-471.

120. Campos-Quirós, A., J.M. Cubero-Sesín, and K. Edalati, Synthesis of nanostructured biomaterials by high-pressure torsion: Effect of niobium content on microstructure and mechanical properties of Ti-Nb alloys. Materials Science and Engineering: A, 2020. **795**: p. 139972.

121. Zhilyaev, A.P., et al., Mechanical behavior and microstructure properties of titanium powder consolidated by high-pressure torsion. Materials Science and Engineering: A, 2017. **688**: p. 498-504.

122. Li, F.X., et al., Microstructure and strength of nano-/ultrafine-grained carbon nanotube-reinforced titanium composites processed by high-pressure torsion. Materials Science and Engineering: A, 2018. **722**: p. 122-128.

123. Edalati, K., et al., Unusual hardening in Ti/Al2O3 nanocomposites produced by high-pressure torsion followed by annealing. Materials Science and Engineering: A, 2011. **529**: p. 435-441.

124. Sun, Y., et al., High-pressure torsion-induced phase transformations and grain refinement in Al/Ti composites. Journal of Materials Science, 2017. **52**(20): p. 12170-12184.

125. Khobragade, N., et al., Mechanical and electrical properties of copper-graphene nanocomposite fabricated by high pressure torsion. Journal of Alloys and Compounds, 2019. **776**: p. 123-132.

126. Abd El Aal, M.I. and H.S. Kim, Effect of the fabrication method on the wear properties of copper silicon carbide composites. Tribology International, 2018. **128**: p. 140-154.

127. Li, H., et al., Processing and characterization of nanostructured Cu-carbon nanotube composites. Materials Science and Engineering: A, 2009. **523**(1): p. 60-64.

128. Long, B.D., et al., Fabrication of high strength Cu–NbC composite conductor by high pressure torsion. Materials Science and Engineering: A, 2011. **528**(3): p. 1750-1756.

129. Long, B.D., et al., Comparison of Two Powder Processing Techniques on the Properties of Cu-NbC Composites. Advances in Materials Science and Engineering, 2014. **2014**: p. 6.

130. Abd El Aal, M.I., Effect of high-pressure torsion processing on the microstructure evolution and mechanical properties of consolidated micro size Cu and Cu-SiC powders. Advanced Powder Technology, 2017. **28**(9): p. 2135-2150.

131. Eremina, M.A., et al., Effect of compaction method on the structure and properties of bulk Cu + Cr3C2 composites. The Physics of Metals and Metallography, 2016. **117**(5): p. 510-517.

132. Stückler, M., et al., Intermixing of Fe and Cu on the atomic scale by high-pressure torsion as revealed by DC- and AC-SQUID susceptometry and atom probe tomography. Acta Materialia, 2020.

133. Borchers, C., et al., Nanocrystalline steel obtained by mechanical alloying of iron and graphite subsequently compacted by high-pressure torsion. Acta Materialia, 2015. **97**: p. 207-215.

134. Kilmametov, A., et al., High-pressure torsion driven mechanical alloying of CoCrFeMnNi high entropy alloy. Scripta Materialia, 2019. **158**: p. 29-33.

135. Zou, J.X., et al., Nanostructured bulk Mg+MgO composite synthesized through arc plasma evaporation and high pressure torsion for H-storage application. Materials Science and Engineering: B, 2014. **183**: p. 1-5.

136. Edalati, K., et al., New nanostructured phases with reversible hydrogen storage capability in immiscible magnesium–zirconium system produced by high-pressure torsion. Acta Materialia, 2016. **108**: p. 293-303.

137. Edalati, K., et al., Ultra-severe plastic deformation: Evolution of microstructure, phase transformation and hardness in immiscible magnesium-based systems. Materials Science and Engineering: A, 2017. **701**: p. 158-166.

138. Pouryazdan, M., et al., Mixing instabilities during shearing of metals. Nature Communications, 2017. **8**(1): p. 1611.

139. Rogachev, S.O., et al., Features of Structure Formation in Layered Metallic Materials Processed by High Pressure Torsion. Metallurgical and Materials Transactions A, 2020. **51**(4): p. 1781-1788.

140. Qi, Y., et al., Plastic flow and microstructural instabilities during high-pressure torsion of Cu/ZnO composites. Materials Characterization, 2018. **145**: p. 389-401.

Chapter 3.

Consolidation of Magnesium and Magnesium Alloy Machine Chips Using High-Pressure Torsion

Moara M. de Castro[1], Amanda P. Carvalho[2], Pedro Henrique R. Pereira[3], Augusta C. Isaac Neta[1], Roberto B. Figueiredo[1], Terence G. Langdon[3,4]

1 Department of Metallurgical and Materials Engineering, Universidade Federal de Minas Gerais, Belo Horizonte 31270-901, Brazil
2 Department of Mechanical Engineering, Universidade Federal de Minas Gerais, Belo Horizonte 31270-901, Brazil
3 Materials Research Group, Faculty of Engineering and the Environment, University of Southampton, Southampton SO17 1BJ, UK
4 Departments of Aerospace and Mechanical Engineering & Materials Science, University of Southern California, Los Angeles, CA 90089-1453, U.S.A.

Abstract: High-pressure torsion processing technique was used to consolidate and process magnesium-based chips. Chips were prepared by machining commercially pure magnesium and a magnesium alloy AZ91 separately. Optical microscopy and microhardness measurements showed good consolidation of pure magnesium. The magnesium alloy still exhibited the boundaries between the chips even after 5 turns of HPT suggesting poor bonding. The results show that soft chips are easier to consolidate through HPT than harder alloys.

Keywords: High-pressure torsion; Consolidation of machine chips; Magnesium; Composite.

3.1. Introduction

Severe plastic deformation (SPD) techniques [1] have been widely used to refine the grain structure of metallic materials, including magnesium and its alloys, to the submicron range. Exceptional mechanical properties including high strength [2-4], high ductility [5-7] and superplasticity [8-11] are developed in these materials. Recent papers have also shown that severe plastic deformation can also improve the corrosion resistance of magnesium [12-14]. SPD processing can is also used for the consolidation of metallic particles due to the concurrent compressive stresses and high shear strain. There are reports of successful consolidation of aluminium [15], copper [16] and also magnesium [17] by equal-channel angular pressing (ECAP) [18]. This processing technique also enables the production of composites by the consolidation of ceramic and metallic particles [19].

Nevertheless, significantly higher compressive stresses and shear strains are developed in high-pressure torsion (HPT) [20] which offers superior conditions for consolidation of metallic particles. Thus, HPT has been used for the consolidation of copper [21], titanium [22], aluminium [23], molybdenum [24], tungsten [25] and other metallic materials. Metal matrix composites have also been produced by HPT through the consolidation of metallic particles. For example, aluminum/carbon nanotube [26], aluminum/iron [27] and aluminum/magnesium [28, 29] composites were produced by HPT. Successful consolidation of magnesium particles was also reported [30, 31]. However, the consolidation of machine chips of magnesium has not been reported in the literature. Machine chips of copper [21] and aluminium alloy [32] were successfully consolidated by HPT and thus the present paper aims to study the consolidation of magnesium chips. Also, HPT consolidation of metallic particles is usually performed in pure metals and the present paper will evaluate the consolidation of a magnesium AZ91 alloy. A hard ceramic phase will be added to evaluate the potential to develop a magnesium alloy based composite.

3.2. Experimental Procedure

Machine chips of commercially pure magnesium (CP-Mg) and a magnesium alloy AZ91 were produced by dry milling of cast ingots of these materials. The milling machine was completely cleaned to avoid contamination of the chips which were collected using a paper box placed below the worktable. The first attempt to consolidate the chips employed an external barrier to facilitate the production of

the disc-shaped samples. CP-Mg chips were placed inside a copper tube with 10 mm external diameter, pre-compacted and then sliced into 1 mm thick discs using a diamond saw cutter. The second attempt did not use an external barrier. The AZ91 chips were placed inside a hard steel channel with 10 mm diameter and cold-pressed to 200 MPa using a hydraulic press. The pre-compacted cylinders were then sliced into 1 mm thickness discs. To produce an alumina reinforced magnesium composite, alumina particles with ~1 μm diameter were manually mixed with the AZ91 alloy chips at a proportion of 10% in volume. The mixed particles were cold pressed at 300 MPa using a steel channel and plunger and then sliced into 1 mm discs using a diamond saw cutter.

The discs were placed in the lower anvil of a quasi-constrained HPT machine and processed up to 5 turns at a nominal pressure of 6 GPa at 1 rpm. It is worth noting that the discs had initially a larger thickness than the usual samples for HPT processing (~0.8 mm). These larger samples were produced to account for the porosity of the cold compacted material. The number of turns and the pressure was selected since previous papers reported successful consolidation of copper chips [21] and titanium powder [22] with these parameters. Figure 3.1 shows the appearance of the machine chips, the pre-compact and HPT processed sample.

After processing, the discs were ground and polished using conventional metallographic procedures and observed in an optical microscope to evaluate the homogeneity of the structure. The surface perpendicular to the torsion axis and a longitudinal surface were observed. Also, Vickers microhardness tests were used to evaluate the homogeneity of the disc of CP-Mg.

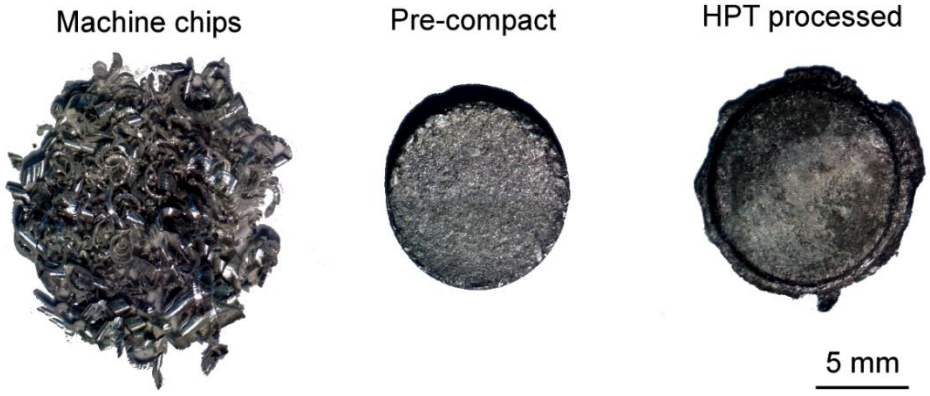

Figure 3.1 – Appearance of the machine chips, the pre-compact and the HPT processed sample.

3.3. Results and discussion

All the discs appeared fully dense after HPT processing to 5 turns. However, close inspection using optical microscopy after polishing revealed large pores and incomplete bonding of the machine chips of the AZ91 alloy. Figure 3.2 shows the appearance of a quarter of the discs of CP-Mg chips, AZ91 chips and AZ91 chips with 10% Al_2O_3 particles. The CP-Mg chips exhibit good bonding and uniform microstructure. Some pores are still present but the boundaries of the original chips are not recognizable. The AZ91 chips show fair consolidation and only a few pores are easily observed. However, the boundaries of the original chips are still clear which suggests poor bonding. The AZ91 chips with alumina reinforcement show a lack of consolidation. Large pores are observed and the original chips did not consolidate well.

The longitudinal section of the discs is shown in Figure 3.3. The consolidation is homogeneous in the CP-Mg but not in the samples of the AZ91 alloy. Also, the consolidation is poorer near the centre which is attributed to the lower shear strain in this area. The disc with ceramic particles reinforcement clearly shows a lack of bonding between the original machine chips. This can be explained by the formation of a layer of ceramic particles around the chips and sliding of the chips during HPT instead of plastic deformation. Shear plastic deformation is required to create new surfaces and bonding.

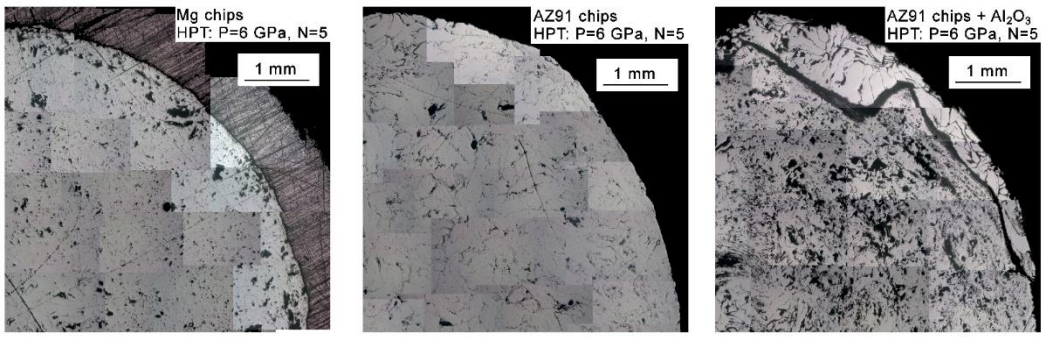

Figure 3.2 – Optical microscopy images of the discs on the plane normal to the torsional axis after HPT processing to 5 turns.

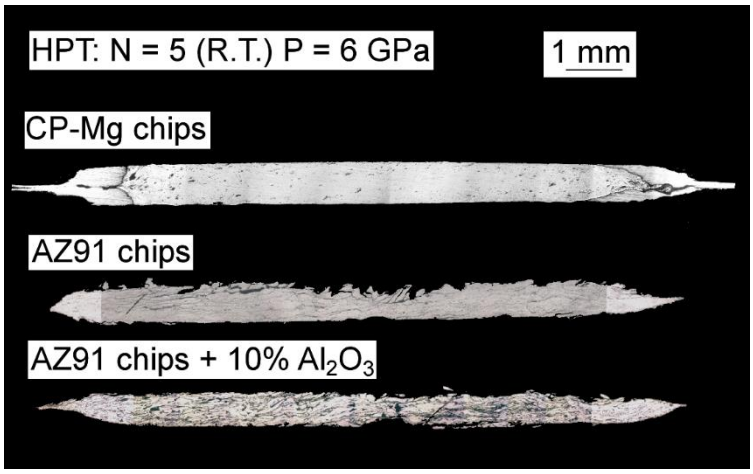

Figure 3.3 – Optical microscopy images of the longitudinal plane of the discs of CP-Mg chips, AZ91 chips and AZ91+10% Al_2O_3 processed by HPT.

Figure 3.4 shows the appearance of the longitudinal section of the discs of CP-Mg chips at $^1/_8$, 1 and 5 turns. This clearly shows the initial shaping of the chips followed by gradual bonding until a fully dense microstructure is obtained.

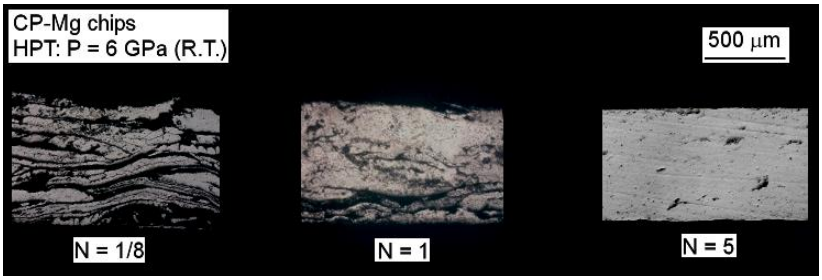

Figure 3.4 – Optical microscopy images of the centre of the disc of CP-Mg chips processed by a different number of turns of HPT.

Microhardness tests were carried out along the longitudinal section of the disc of CP-Mg chips consolidated by 5 turns of HPT. The average of the hardness is plotted as a function of the distance to the centre in Figure 3.5. The hardness range (~40-45 Hv) is similar to the values observed after HPT processing of bulk samples [33, 34] of pure magnesium confirming successful consolidation. A higher hardness was observed at one edge of the sample and it is attributed to some limited mixing of copper with magnesium in this region. The large shear strain leads to the mixing of materials.

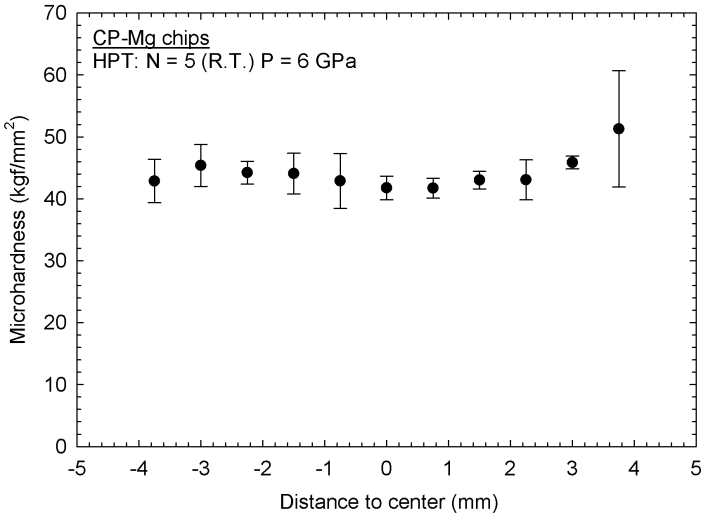

Figure 3.5 – Microhardness of the CP-Mg chips consolidated by HPT and plotted as a function of the distance to the centre.

3.4. Summary and conclusions

1. Machine chips of CP-Mg and AZ91 alloy were pre-compacted and processed by HPT up to 5 turns under a pressure of 6 GPa. The CP-Mg chips were fully consolidated while the boundaries of the chips of the AZ91 alloy remained visible.
2. The use of Al_2O_3 particles as reinforcement leads to a lack of bonding between the machine chips which is attributed to the sliding of chips during HPT.
3. The hardness of the fully-dense disc of CP-Mg is in the range of bulk magnesium processed by HPT. Localized mixing of metals takes place near the edge of the disc when using a container for the machine chips.

3.5. Author contributions

M.M.C. contributed to sample preparation, carried out hardness tests, microstructure analysis, and prepared the first draft of the manuscript.

3.6. Acknowledgements

The authors acknowledge support from FAPEMIG under grants APQ-02786-14 and APQ00580-15, CAPES-Proex and CNPq under grant 400407/2016-7. MMC and PHRP acknowledge support from CAPES.

3.7. References

1. Valiev RZ, Islamgaliev RK, Alexandrov IV. Bulk nanostructured materials from severe plastic deformation. Progress in Materials Science. 2000;45:103-87.

2. Zheng RX, Bhattacharjee T, Shibata A, Sasaki T, Hono K, Joshi M, *et al.* Simultaneously enhanced strength and ductility of Mg-Zn-Zr-Ca alloy with fully recrystallized ultrafine-grained structures. Scripta Materialia. 2017;131:1-5.

3. Lukyanova EA, Martynenko NS, Shakhoya I, Belyakov AN, Rokhlin LL, Dobatkin SV, *et al.* Strengthening of age-hardenable WE43 magnesium alloy processed by high-pressure torsion. Materials Letters. 2016;170:5-9.

4. Balogh L, Figueiredo RB, Ungár T, Langdon TG. The contributions of grain size, dislocation density and twinning to the strength of a magnesium alloy processed by ECAP. Materials Science and Engineering A. 2010;528(1):533-8.

5. Mukai T, Yamanoi M, Watanabe H, Higashi K. Ductility enhancement in AZ31 magnesium alloy by controlling its grain structure. Scripta Materialia. 2001;45:89-94.

6. Figueiredo RB, Poggiali FSJ, Silva CLP, Cetlin PR, Langdon TG. The influence of grain size and strain rate on the mechanical behavior of pure magnesium. Journal of Materials Science. 2016;51(6):3013-24.

7. Figueiredo RB, Sabbaghianrad S, Giwa A, Greer JR, Langdon TG. Evidence for exceptional low temperature ductility in polycrystalline magnesium processed by severe plastic deformation. Acta Materialia. 2017;122:322-31.

8. Figueiredo RB, Langdon TG. Strategies for achieving high strain rate superplasticity in magnesium alloys processed by equal-channel angular pressing. Scripta Materialia. 2009;61(1):84-7.

9. Figueiredo RB, Langdon TG. Developing superplasticity in a magnesium AZ31 alloy by ECAP. Journal of Materials Science. 2008;43(23-24):7366-71.

10. Figueiredo RB, Langdon TG. Record Superplastic Ductility in a Magnesium Alloy Processed by Equal-Channel Angular Pressing. Advanced Engineering Materials. 2008;10:37-40.

11. Figueiredo RB, Langdon TG. The development of superplastic ductilities and microstructural homogeneity in a magnesium ZK60 alloy processed by ECAP. Materials Science and Engineering A. 2006;430(1-2):151-6.

12. Silva CLP, Oliveira AC, Costa CGF, Figueiredo RB, de Fátima Leite M, Pereira MM, *et al.* Effect of severe plastic deformation on the biocompatibility and corrosion rate of pure magnesium. Journal of Materials Science. 2017;52(10):5992-6003.

13. Zhang CZ, Guan SK, Wang LG, Zhu SJ, Chang L. The microstructure and corrosion resistance of biological Mg-Zn-Ca alloy processed by high-pressure torsion and subsequently annealing. Journal of Materials Research. 2017;32(6):1061-72.

14. Gao JH, Guan SK, Ren ZW, Sun YF, Zhu SJ, Wang B. Homogeneous corrosion of high pressure torsion treated Mg-Zn-Ca alloy in simulated body fluid. Materials Letters. 2011;65(4):691-3.

15. Xia K, Wu X. Back pressure equal channel angular consolidation of pure Al particles. Scripta Materialia. 2005;53(11):1225-9.

16. Haouaoui M, Karaman I, Maier HJ, Hartwig KT. Microstructure evolution and mechanical behavior of bulk copper obtained by consolidation of micro- and nanopowders using equal-channel angular extrusion. Metallurgical and Materials Transactions a-Physical Metallurgy and Materials Science. 2004;35A(9):2935-49.

17. Lee HC, Chao CG, Liu TF, Lin CY, Wang HC. Effect of Temperature and Extrusion Pass on the Consolidation of Magnesium Powders Using Equal Channel Angular Extrusion. Materials Transactions. 2013;54(5):765-8.

18. Valiev RZ, Langdon TG. Principles of equal-channel angular pressing as a processing toold for grain refinement. Progress in Materials Science. 2006;51:881-981.

19. Xu W, Wu X, Honma T, Ringer SP, Xia K. Nanostructured Al–Al_2O_3 composite formed in situ during consolidation of ultrafine Al particles by back pressure equal channel angular pressing. Acta Materialia. 2009;57(14):4321-30.

20. Zhilyaev AP, Langdon TG. Using high-pressure torsion for metal processing: Fundamentals and applications Progress in Materials Science. 2008;53(6):893-979.

21. Zhilyaev AP, Gimazov AA, Raab GI, Langdon TG. Using high-pressure torsion for the cold-consolidation of copper chips produced by machining. Materials Science and Engineering: A. 2008;486(1):123-6.

22. Zhilyaev AP, Ringot G, Huang Y, Maria Cabrera J, Langdon TG. Mechanical behavior and microstructure properties of titanium powder consolidated by high-pressure torsion. Materials Science and Engineering: A. 2017;688:498-504.

23. Khajouei-Nezhad M, Paydar MH, Ebrahimi R, Jenei P, Nagy P, Gubicza J. Microstructure and mechanical properties of ultrafine-grained aluminum consolidated by high-pressure torsion. Materials Science and Engineering: A. 2017;682:501-8.

24. Li P, Lin Q, Wang X, Tian Y, Xue K-M. Recrystallization behavior of pure molybdenum powder processed by high-pressure torsion. International Journal of Refractory Metals and Hard Materials. 2018;72:367-72.

25. Li P, Wang X, Xue K-M, Tian Y, Wu Y-C. Microstructure and recrystallization behavior of pure W powder processed by high-pressure torsion. International Journal of Refractory Metals and Hard Materials. 2016;54:439-44.

26. Tokunaga T, Kaneko K, Horita Z. Production of aluminum-matrix carbon nanotube composite using high pressure torsion. Materials Science and Engineering: A. 2008;490(1):300-4.

27. Cubero-Sesin JM, Horita Z. Powder consolidation of Al–10wt% Fe alloy by High-Pressure Torsion. Materials Science and Engineering: A. 2012;558:462-71.

28. Han JK, Lee HJ, Jang JI, Kawasaki M, Langdon TG. Micro-mechanical and tribological properties of aluminum-magnesium nanocomposites processed by high-pressure torsion. Materials Science and Engineering a-Structural Materials Properties Microstructure and Processing. 2017;684:318-27.

29. Kawasaki M, Ahn B, Lee H, Zhilyaev AP, Langdon TG. Using high-pressure torsion to process an aluminum-magnesium nanocomposite through diffusion bonding. Journal of Materials Research. 2016;31(1):88-99.

30. Panda S, Fundenberger J-J, Zhao Y, Zou J, Toth LS, Grosdidier T. Effect of initial powder type on the hydrogen storage properties of high-pressure torsion consolidated Mg. International Journal of Hydrogen Energy. 2017;42(35):22438-48.

31. Grosdidier T, Fundenberger JJ, Zou JX, Pan YC, Zeng XQ. Nanostructured Mg based hydrogen storage bulk materials prepared by high pressure torsion consolidation of arc plasma evaporated ultrafine powders. International Journal of Hydrogen Energy. 2015;40(47):16985-91.

32. Abd El Aal MI, Yoo Yoon E, Seop Kim H. Recycling of AlSi8Cu3 alloy chips via high pressure torsion. Materials Science and Engineering: A. 2013;560:121-8.

33. Edalati K, Yamamoto A, Horita Z, Ishihara T. High-pressure torsion of pure magnesium: Evolution of mechanical properties, microstructures and hydrogen storage capacity with equivalent strain. Scripta Materialia. 2011;64(9):880-3.

34. Qiao XG, Zhao YW, Gan WM, Chen Y, Zheng MY, Wu K, *et al.* Hardening mechanism of commercially pure Mg processed by high pressure torsion at room temperature. Materials Science and Engineering a-Structural Materials Properties Microstructure and Processing. 2014;619:95-106.

Chapter 4.

Development of a magnesium-alumina composite through cold consolidation of machining chips by high-pressure torsion

Moara M. de Castro[1], Pedro Henrique R. Pereira[1,2], Augusta C. Isaac Neta[1], Roberto B. Figueiredo[1], Terence G. Langdon[2]

[1] Department of Metallurgical and Materials Engineering,
Universidade Federal de Minas Gerais, Belo Horizonte, MG 31270-901, Brazil
[2] Materials Research Group, Department of Mechanical Engineering,
University of Southampton, Southampton SO17 1BJ, UK

Abstract: High pressure torsion offers unique conditions for the consolidation of metallic particles at room temperature owing to the high hydrostatic compressive stresses combined with the high shear strain. A Mg-Al_2O_3 composite was produced by consolidation of machining chips of pure magnesium with 10% in volume of alumina particles. The consolidation process was investigated by optical and scanning electron microscopy and X-ray microtomography. It is shown that shear deformation concentrates along thick alumina particle layers in the initial stage of deformation. A significant fraction of the hard phase particles are pushed into the outflow in quasi-constrained HPT and a homogeneous composite is achieved after significant straining. The composite exhibits a refined microstructure, a higher hardness and improved resistance against room temperature creep compared to pure magnesium.

Keywords: Alumina; Consolidation; Metal matrix composite; Magnesium; High-pressure torsion;

4.1. Introduction

Magnesium, the lightest structural metallic material, has attracted renewed interest in the automotive and aerospace sectors owing to the increasing worldwide demand for reducing fuel consumption and CO_2 emissions. Nevertheless, any replacement of the currently dominant steels and aluminum alloys has proven difficult because of the inherent low strength. Different approaches have been developed to overcome these limitations but generally there has been special emphasis on alloy development and/or an optimization of the processing techniques for achieving enhanced grain refinement and strain hardening. Another potential strengthening route that has begun to attract significant attention is the addition of a hard-reinforcing phase, typically a ceramic, to produce the so-called metal matrix composites (MMCs).

Among the different production routes hitherto developed for the manufacturing of MMCs, severe plastic deformation (SPD) processes have emerged as powerful tools for the consolidation of composites from metal chips, particles or powders [1]. In particular, equal-channel angular pressing (ECAP) [1] has been used for the consolidation of different metals [2] including magnesium [3]. Due to the high pressure and high shear strain exerted in the ECAP processing technique, a binding of the particles is achieved which leads to the production of bulk samples. In practice, it is found that the application of ECAP at higher temperatures, and with the simultaneous aid of a back-pressure, provides the optimum conditions for achieving consolidation.

Processing by high-pressure torsion (HPT) [4] offers an alternative procedure for consolidating metal particles at room temperature because of the ability in HPT to impose extremely high hydrostatic pressures. In the HPT process, the nominal pressure is usually in the range of ~2 – 8 GPa which is well above the flow stress of most metallic materials. This means that the particles will be plastically deformed to an almost fully-dense bulk solid. Furthermore, the torsional straining of the particles increases their surface area to promote the binding of the particles and the application of SPD will lead to a refined microstructure in the matrix. For example, it was shown earlier that milled Al-7.5% Mg powders may be consolidated by applying 5 turns of HPT at a pressure of 6 GPa [5].

There are now several reports documenting the production of MMCs using HPT processing. Thus, a Co-NiO composite was produced by 5 turns of HPT at 6 GPa [6], an Al-fullerene composite was produced by 15 turns at 2.5 GPa [7] and an Al-Al_2O_3 nanocomposite was fabricated by using 10 turns at 6 GPa [8]. There are also reports of the use of HPT for the consolidation of machining chips: for example, copper machining chips were consolidated by 5 turns of HPT at a pressure of 6 GPa at room temperature [9] and Al-8% Si-3% Cu chips were consolidated by 10 turns at a pressure of 8 GPa [10].

Earlier studies demonstrated that Mg powders are effectively consolidated by HPT [11-13] leading to the formation of Mg-MgO composites in which an oxide layer forms naturally around the Mg particles and acts as a reinforcing phase. Nevertheless, despite the very great potential for using HPT in producing Mg-based MMCs at room temperature, investigations on magnesium reinforced with higher contents of ceramic particles has remained essentially unexplored. Accordingly, the present research was initiated with the objective of fabricating Mg-based MMCs by using HPT for the consolidation of magnesium machining chips using alumina as the reinforcing phase.

4.2. Experimental materials and procedures

Commercial purity magnesium was machined by dry milling and the chips were collected. Care was taken to clean the machine before milling and to avoid the use of a lubricant in order to prevent any contamination of the chips. The machining chips were mixed with alumina (Al_2O_3) powder in a 9 to 1 ratio in weight and pre-compacted using a pressure of ~250 MPa into 10 mm diameter discs with ~1.0 mm thickness. The pre-compacted discs were then processed by HPT at room temperature using a quasi-constrained facility [14] operating at a nominal pressure of 6.0 GPa and using a rotation speed of 1 rpm. Samples were processed to 1/8, 1 and 5 turns in order to rigorously track the evolution of consolidation. For comparison purposes, a disc of bulk pure magnesium was also processed by HPT to 5 turns.

The three-dimensional (3D) distributions of alumina particles and voids in the processed samples were evaluated using a SkyScan 1174 micro-CT scanner (Bruker, Germany). This system is equipped with a 50 KeV/40 W tungsten x-ray source and a cooled 1.3-megapixel CCD camera coupled to a scintillator by a lens

with a 1:6 zoom range. Approximately 1000 projections were recorded at angular increments of 1/4° between 0° and 360°. Samples of about 10 mm in diameter were recorded at 70 kV and 140 µm using an aluminum filter of 0.5 mm thickness to reduce any beam hardening artifacts. An X-ray magnification of 6× and a lens magnification of 4× were used to give a field of view of about 10 mm. A pixel size of about 7 µm was achieved. Although the spatial resolution of the X-ray images was about 14 µm, and therefore nearly twice the pixel size, this was larger than the size of the individual alumina particles and this method was therefore effective to distinguish any large pores and alumina agglomerates.

The longitudinal sections of the discs were ground and polished and observed using optical and scanning electron microscopy and the discs processed through 5 turns of HPT were also analysed by X-ray diffraction. MAUD software was used to estimate the crystal structure parameters, the crystallite sizes and the lattice microstrains. Microhardness testing, with a load of 200 gf and a dwell time of 10 s, was used to determine and compare the hardness of pure magnesium and the magnesium-based composite. Dynamic hardness testing was used to determine the room temperature creep properties on longitudinal sections of the consolidated discs. For the creep tests, a constant load of 300 mN was applied during 500 s and the penetration depth was tracked. The creep data were obtained by converting the instantaneous hardness into flow stress and converting the depth and time data into strain rate [15, 16].

4.3. Experimental results

4.3.1 Nature of the consolidation process

Figure 4.1 shows representative X-ray microtomography images of the plan views and side sections of the discs processed through 1/8, 1 and 5 turns of HPT. Any agglomerated alumina shows up in a dark colour with an irregular shape and it is present throughout the sample processed to 1/8 turn. Further processing to 1 turn leads to the formation of a large agglomeration arranged concentrically in the disc sample where the spiral shape of the track suggests that the rotation occurring during HPT gradually pushes the alumina towards the edge of the sample. A small volume of the material occurs as an outflow around the periphery of the disc in quasi-constrained HPT and it is likely that this outflow contained a significant fraction of the reinforcement particles that had flowed together within the disc. The

disc processed to 5 turns exhibits only limited alumina agglomeration and any agglomeration tends to be concentrated in isolated spots near the edge of the disc.

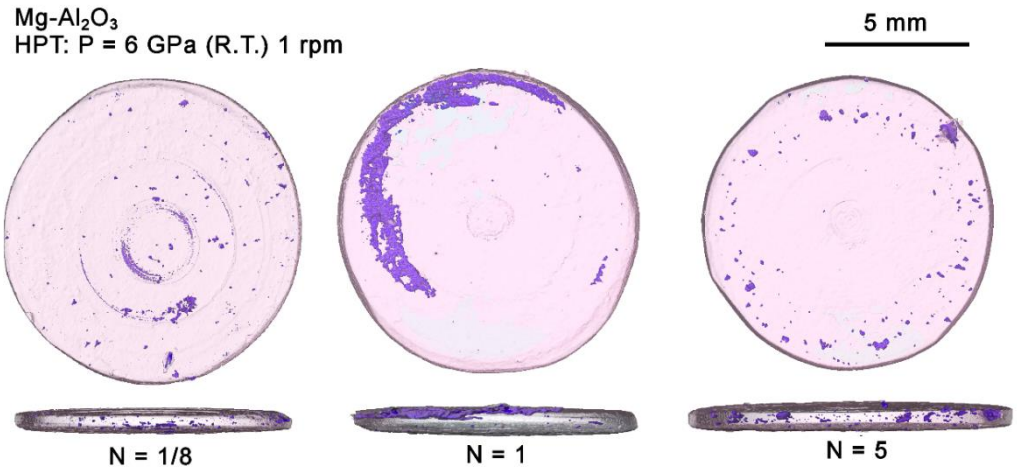

Figure 4.1 – X-ray microtomography images of discs processed to 1/8, 1 and 5 turns of HPT.

The consolidation of the chips and the distributions of the alumina particles were also evaluated along longitudinal sections of the discs using optical and scanning electron microscopy. Figure 4.2 shows low magnification images of the processed discs where pores and any separation between the chips are visible as dark areas. The disc processed to 1/8 turn is characterised by a severe lack of bonding between the chips and the area near the disc centre appears even less consolidated so that a small number of chips was removed from the disc during grinding and polishing.

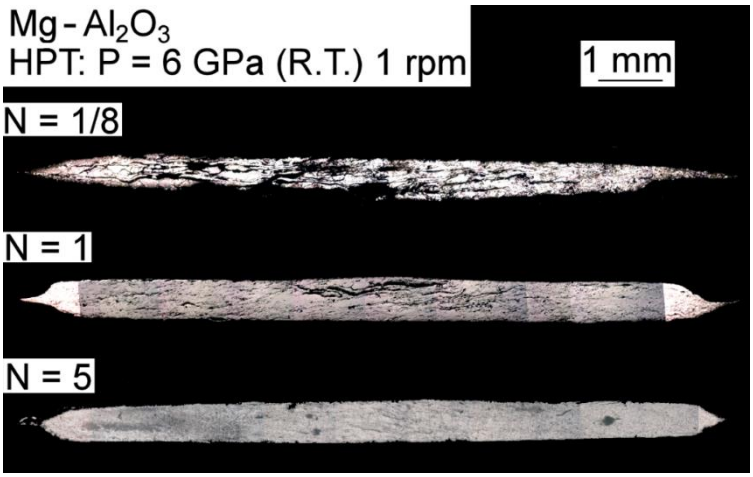

Figure 4.2 – Optical microscopy images of the longitudinal sections of discs processed to 1/8, 1 and 5 turns of HPT.

This image conclusively demonstrates that processing through 1/8 turn is insufficient to achieve a reasonable level of consolidation. The disc processed to 1 turn displays improved consolidation especially near the edge regions although some pores are visible near the centre. Finally, processing to 5 turns lead to an apparent full consolidation of the machining chips throughout the sample although a small amount of ceramic particle agglomeration may remain in the vicinity of the disc centre.

4.3.2 Microstructural characterization after HPT processing

Details of the microstructures near the edges of the processed discs are depicted in Fig. 4.3 where the upper images are after 1/8 and 1 turn and the lower images are after 5 turns at two different magnifications. There is a clear distinction between the large magnesium volumes and the alumina particles which are concentrated between these areas in the sample processed to 1/8 turn.

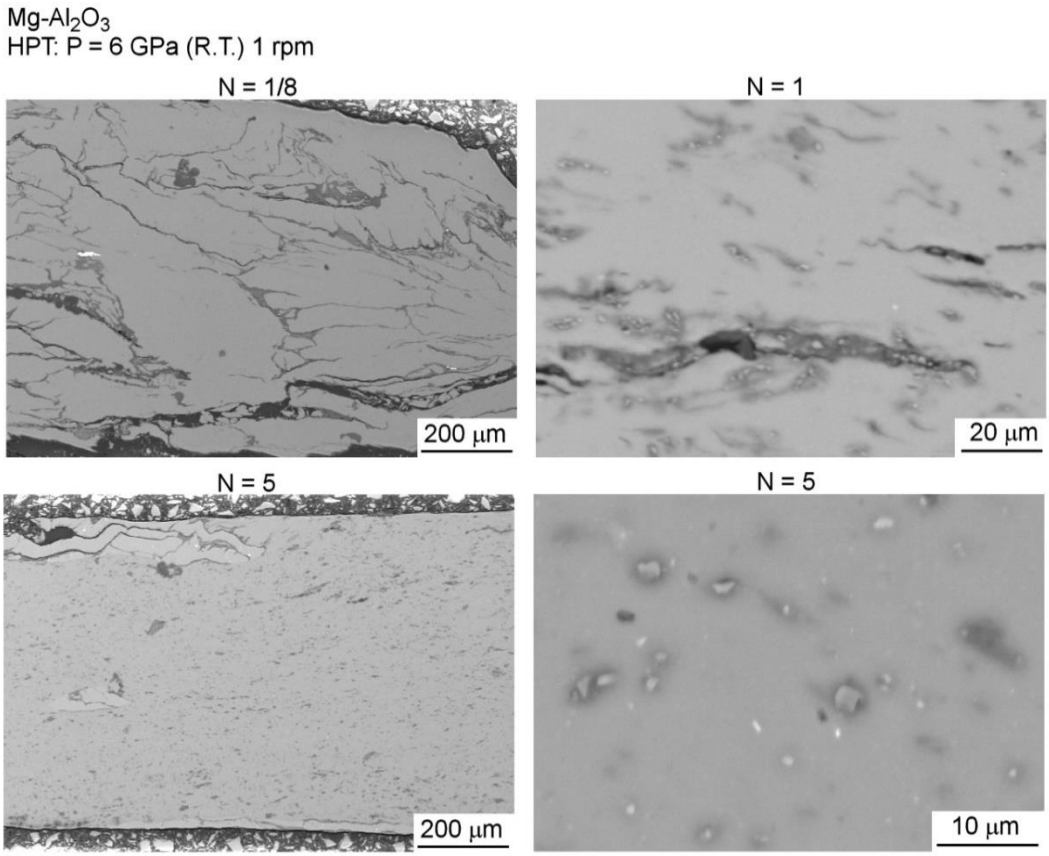

Figure 4.3 – Scanning electron microscopy images of the microstructures of discs processed to different numbers of HPT turns.

Thus, the alumina-rich areas prevent bonding of the magnesium chips and an elongated gap is visible at the bottom of the image. Increasing the shear straining to 1 turn of HPT leads to the formation of bonding between the magnesium chips and the dispersion of the alumina particles although some tracks of alumina are again visible. Further processing to 5 turns leads to a complete bonding of the magnesium chips as shown in the lower images. Thus, although some ceramic particles may remain partially agglomerated near the disc centre, there is a homogeneous distribution near the edges and throughout almost all of the disc. Detailed inspection of the microstructure near the centre of the disc processed to 5 turns revealed some distinct particles of alumina but the total amount of the ceramic particles was significantly less than the initial value of 10%. Image analysis of the longitudinal section of the disc processed through 5 turns revealed that a surface fraction of Al_2O_3 of ~3.5% near the centre of the disc but a fraction of only ~0.5% near the edge.

Figure 4.4 shows the X ray diffraction (XRD) patterns of the discs of pure magnesium (upper) and the Mg-Al_2O_3 composite (lower) after processing through 5 turns. The relative intensities of the peaks appear similar in both discs suggesting the presence of similar textures. A few small peaks associated with the Al_2O_3 were identified in the lower pattern. The low intensities of these Al_2O_3 peaks suggest that only a minor fraction of the composite is composed of this phase and this is consistent with the microtomography that provided evidence for alumina agglomerates appearing in the outflow around the periphery of the disc during processing in HPT. The lattice parameters, crystallite size and lattice microstrain were estimated using Rietveld refinement method. The experimental points (symbols), simulated profiles (lines) and the difference between them are also depicted in Fig. 4.4 and these data are summarised in Table 4.1. Thus, the crystal parameters are generally similar in the bulk magnesium and the magnesium composite although the crystallite size is smaller and the lattice microstrain is larger in the composite. The similar crystal parameters discard the formation of solid solution in the magnesium matrix.

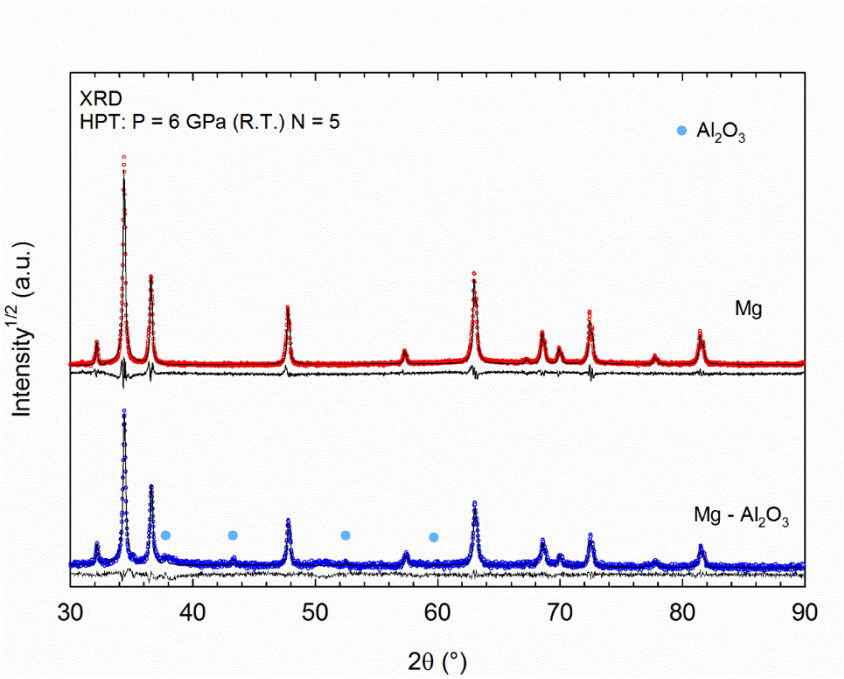

Figure 4.4 – X-ray diffraction patterns and simulated patterns of discs processed by 5 HPT turns of HPT.

Table 4.1 – Crystallite size, d_{XRD}, unit cell parameters, *a* and *c*, and lattice microstrain, ε, for pure magnesium and the Mg-Al_2O_3 composite.

	d_{XRD} (nm)	a (nm)	c (nm)	$\varepsilon \times 10^4$
Mg	206	0.32138	0.52152	4.10
Mg-Al_2O_3	158	0.32111	0.52128	7.17

4.3.3 Hardness values and creep data after HPT processing

The distribution of hardness values in the radial directions of discs of bulk magnesium and of the Mg-Al_2O_3 composite are depicted in Fig. 4.5. Pure magnesium exhibits a saturation in hardness at ~48 kgf/mm^2 after 5 turns of HPT and this value remains essentially constant across the disc. This saturation value is in agreement with other reports of the HPT processing of pure magnesium [17, 18]. By contrast, the magnesium composite shows no evidence of a hardness saturation and instead the hardness increases and reaches a maximum at the edge of the disc. Initially, the microhardness values near the centre of the Mg-Al_2O_3 disc are lower than for the pure metal after processing under equivalent conditions and this indicates that the grain refinement kinetics in the composite are initially delayed due to the occurrence of particle binding. It also appears that a full

consolidation was not achieved in this region of the Mg-Al_2O_3 composite after 5 revolutions of HPT. Conversely, the hardness in the Mg composite is significantly larger than for pure magnesium at the edge of the disc which shows the hardness saturation in the composite will require a higher level of shear strain although the maximum attainable hardness is then at a higher value.

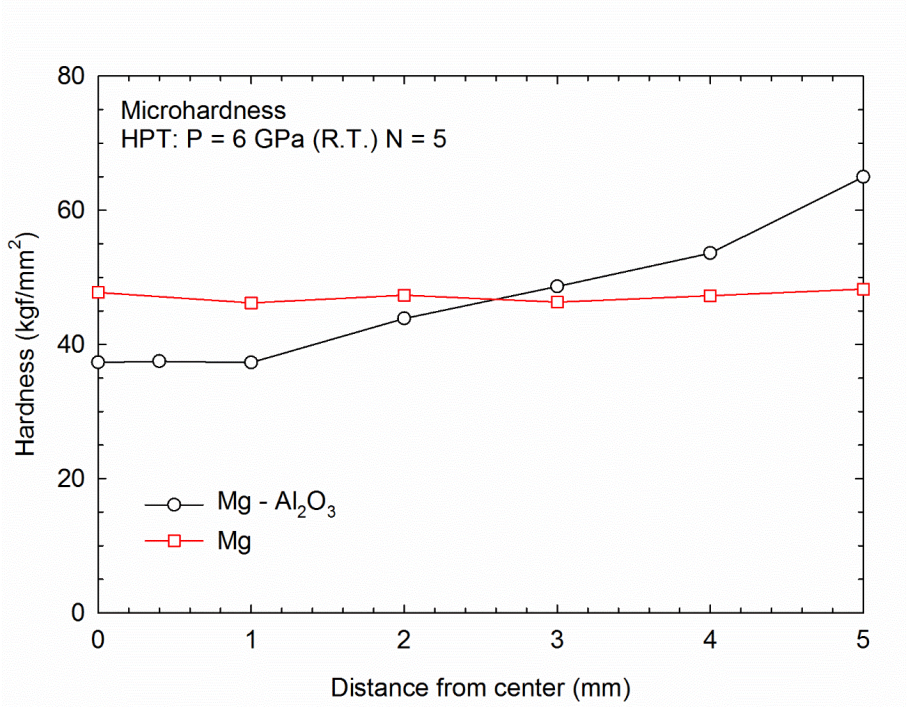

Figure 4.5 – Microhardness plotted as a function of the distance from the centre of discs of pure magnesium and magnesium composite processed to 5 turns of HPT.

Dynamic hardness testing was used to evaluate creep at room temperature in the magnesium matrix. Figure 4.6(a) shows the depth versus time data and trend curves for indentations near the edge of the discs of pure magnesium and the composite processed by 5 turns of HPT. The depth increases with time for application of a constant load due to the occurrence of room temperature creep and it is apparent that this effect is more pronounced in the pure material. These data were converted into the flow stress versus strain rate and the relevant curves are plotted in Fig. 4.6(b). The results show that the flow stresses for the Mg-Al_2O_3 composite are higher than for pure magnesium but the strain rate sensitivity is lower. It is readily apparent that the hard particles are more effective in increasing the low strain rate flow stress. It was noted earlier that an increase in strain rate sensitivity is associated with a change in deformation mechanism at room temperature in pure magnesium [16,19]. It is worth noting also that the strain rate sensitivity of the composite in this investigation is high compared to conventional coarse-grained magnesium where earlier results showed $m \approx 0.03$ [16].

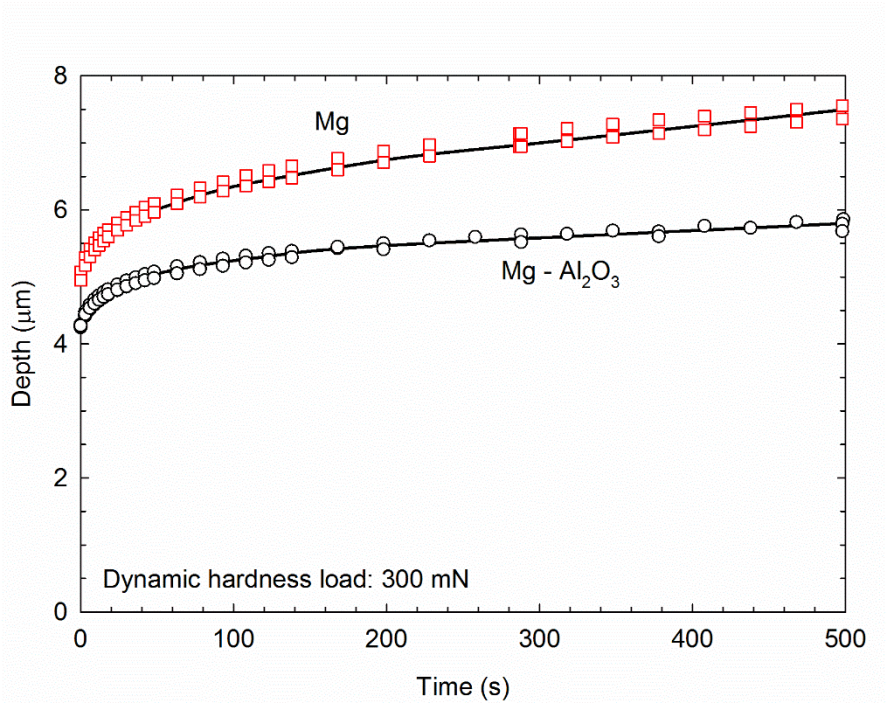

(a)

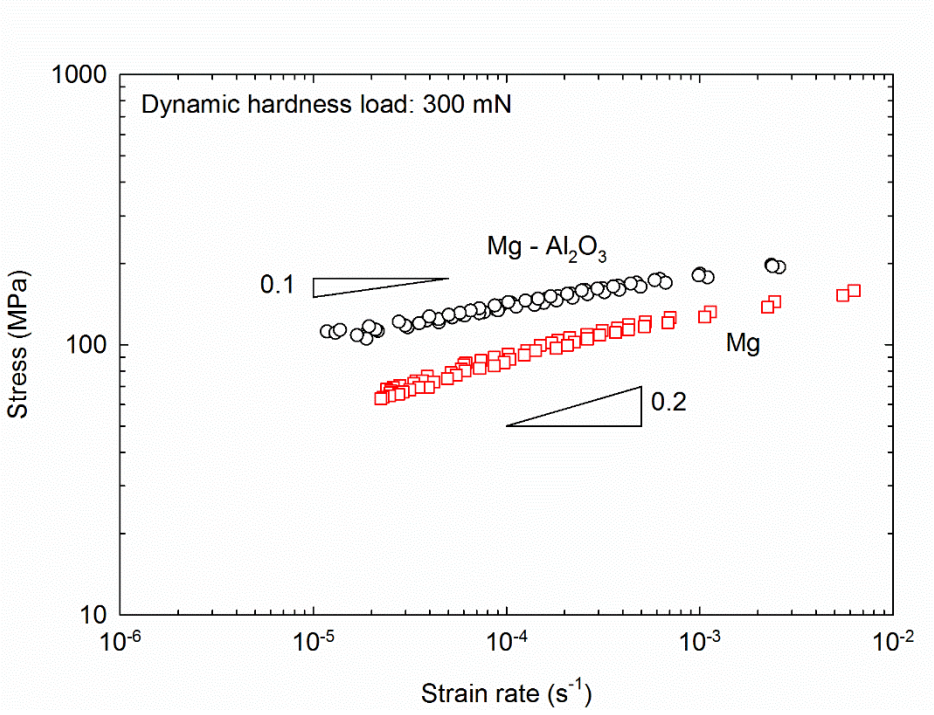

(b)

Figure 4.6 – (a) Depth vs time data and (b) room temperature stress vs strain rate curves determined by dynamic hardness testing; data for pure magnesium processed by HPT is also shown for comparison.

4.4. Discussion

The consolidation of metallic particles [11, 12, 20, 21] and chips [9, 10] into bulk samples was reported earlier and there are also reports of the incorporation of metallic particles and hard phase particles into metal matrix composites by HPT [7, 8, 13, 22]. Nevertheless, the present results demonstrate that it is feasible to mix magnesium chips and hard ceramic particles in order to produce bulk nano-composites by HPT. It is noted, however, that the larger size of the chips increases the difficulty both of bonding the metallic phase and of achieving a homogeneous mixing of the phases.

The initial division of phases leads to the build up of a thick layer of a hard ceramic phase between the large chips. These layers then prevent full contact between the metallic phase during the early stage of processing. As a consequence, the chips initially slide over the loose ceramic particles without incurring any significant plastic deformation. The thickness of the ceramic particle layer gradually decreases as this phase is pushed towards the edge of the sample and binding between the chips then starts to develop. Accordingly, a dense metallic matrix network is only observed in some areas of the disc after a full turn of HPT. The microstructure at this stage remains heterogeneous since there is a clear distinction between the areas rich in ceramic particles and the areas of pure magnesium. The mixing of these phases is only achieved after additional significant straining up to 5 turns of HPT. It is important to note that an earlier consolidation of pure magnesium particles and powders was achieved with a total shear strain of only ~42 [11] while the composite in the current investigation required a total shear strain of ~196 at the edge of the disc.

Observations of the microstructure of the disc processed to 5 turns of HPT suggest that the total volume of alumina particles decreases during processing. Thus, the initial sample was prepared with 10% of total volume of alumina particles but a smaller fraction was observed after HPT processing. It is reasonable to anticipate that a small fraction of alumina particles may be removed from the surface of the sample during metallographic preparation but this effect cannot account for the significant difference. The evidence from X-ray diffraction also suggests that only a few percent of alumina particles are present in the sample after 5 turns of HPT. This reduction in the volume fraction of the hard phase is attributed to the preferential outflow which occurs in quasi-constrained HPT at the edges of the

sample. Furthermore, this is in agreement with the observation of a spiral of alumina in the microtomography image in Fig. 4.1 after 1 turn.

Although a large fraction of the reinforcement phase was lost during processing, a homogeneous distribution of alumina particles was attained within the magnesium matrix at the edge of the sample processed to 5 turns. The reinforcement phase led to a decrease in the crystallite size and an increase in the lattice microstrain compared to the bulk pure magnesium. As a consequence, the composite displays different mechanical behavior.

It is known that pure magnesium exhibits a saturation in hardness at low levels of strain when processing by HPT. Typical values of hardness for HPT-processed pure magnesium are within the range ~35 - 55 kgf mm^{-2} [17, 18, 23]. By contrast, the hardness at the edge of the Mg-Al_2O_3 composite in these experiments was ~75 kgf mm^{-2}. In addition, the composite exhibits a higher resistance against room temperature creep. Recent reports have shown that pure magnesium changes the deformation behavior with grain refinement [16, 19, 24-26] and becomes extremely ductile, where this change in behavior is attributed to the onset of room temperature creep by grain boundary sliding [19]. The flow stress versus strain rate curve of the Mg-Al_2O_3 composite in Fig. 4.6(b) shows an increase in the low strain rate flow stress and a decrease in the strain rate sensitivity. This suggests that the presence of hard particles in the present experiments serves to hinder the occurrence of grain boundary sliding. It is known that a fine dispersion of hard particles promotes a local strain gradient in the metallic matrix which increases hardening rate and strengthening [27]. This is in agreement with the larger lattice microstrain and higher hardness observed in the Mg-Al_2O_3 composite in this investigation.

4.5. Summary and conclusions

1. A Mg-Al_2O_3 composite was produced by consolidation of pure magnesium chips and alumina particles using high-pressure torsion. The microstructural evolution was determined by optical microscopy, scanning electron microscopy and X-ray microtomography.

2. The initial segregation of phases leads initially to the sliding of magnesium chips along thick layers of loose alumina particles. The thickness of these alumina

particles layers decreases gradually as this phase is preferentially pushed into the outflow which occurs around the periphery of the disc in quasi-constrained HPT. The results show the bonding between the magnesium chips and the mixing of the phases requires a large amount of shear strain.

3. The Mg-Al_2O_3 composite exhibits a smaller crystallite size, a higher lattice microstrain and a higher hardness by comparison with bulk pure magnesium processed by HPT. The Mg-Al_2O_3 composite also displays enhanced resistance against room temperature creep compared to bulk magnesium.

4.6. Author contributions

M.M.C. carried out hardness and dynamic hardness tests and micro-CT analysis, contributed to sample preparation and microstructure analysis and prepared the first draft of the manuscript.

4.7. Acknowledgements

The authors thank the Microscopy Centre of UFMG for experimental assistance. This work was supported by the Serrapilheira Institute (grant number Serra-1709-17750), CNPq, FAPEMIG and CAPES-Proex. One of the authors was supported by the European Research Council under ERC Grant Agreement No. 267464-SPDMETALS (TGL).

4.8. References

1. R.Z. Valiev, R.K. Islamgaliev, I.V. Alexandrov, Bulk nanostructured materials from severe plastic deformation, Progress in Materials Science 45 (2000) 103-187.
2. X.L. Wu, K. Xia, Synthesis of Bulk Materials by Equal Channel Angular Consolidation of Particles, Materials Science Forum 503-504 (2006) 233-238.
3. H.C. Lee, C.G. Chao, T.F. Liu, C.Y. Lin, H.C. Wang, Effect of Temperature and Extrusion Pass on the Consolidation of Magnesium Powders Using Equal Channel Angular Extrusion, Materials Transactions 54 (2013) 765-768.
4. A.P. Zhilyaev, T.G. Langdon, Using high-pressure torsion for metal processing: Fundamentals and applications Progress in Materials Science 53 (2008) 893-979.

5. Z. Lee, F. Zhou, R.Z. Valiev, E.J. Lavernia, S.R. Nutt, Microstructure and microhardness of cryomilled bulk nanocrystalline Al–7.5%Mg alloy consolidated by high pressure torsion, Scripta Materialia 51 (2004) 209-214.

6. E. Menéndez, J. Sort, V. Langlais, A. Zhilyaev, J.S. Muñoz, S. Suriñach, J. Nogués, M.D. Baró, Cold compaction of metal–ceramic (ferromagnetic–antiferromagnetic) composites using high pressure torsion, Journal of Alloys and Compounds 434-435 (2007) 505-508.

7. T. Tokunaga, K. Kaneko, K. Sato, Z. Horita, Microstructure and mechanical properties of aluminum–fullerene composite fabricated by high pressure torsion, Scripta Materialia 58 (2008) 735-738.

8. M. Ashida, Z. Horita, T. Kita, A. Kato, Production of Al/Al_2O_3 Nanocomposites through Consolidation by High-Pressure Torsion, Materials Transactions 53 (2012) 13-16.

9. A.P. Zhilyaev, A.A. Gimazov, G.I. Raab, T.G. Langdon, Using high-pressure torsion for the cold-consolidation of copper chips produced by machining, Materials Science and Engineering: A 486 (2008) 123-126.

10. M.I. Abd El Aal, E. Yoo Yoon, H. Seop Kim, Recycling of AlSi8Cu3 alloy chips via high pressure torsion, Materials Science and Engineering: A 560 (2013) 121-128.

11. S. Panda, J.-J. Fundenberger, Y. Zhao, J. Zou, L.S. Toth, T. Grosdidier, Effect of initial powder type on the hydrogen storage properties of high-pressure torsion consolidated Mg, International Journal of Hydrogen Energy 42 (2017) 22438-22448.

12. T. Grosdidier, J.J. Fundenberger, J.X. Zou, Y.C. Pan, X.Q. Zeng, Nanostructured Mg based hydrogen storage bulk materials prepared by high pressure torsion consolidation of arc plasma evaporated ultrafine powders, International Journal of Hydrogen Energy 40 (2015) 16985-16991.

13. J.X. Zou, C.F. Pérez-Brokate, R. Arruffat, B. Bolle, J.J. Fundenberger, X.Q. Zeng, T. Grosdidier, W.J. Ding, Nanostructured bulk Mg+MgO composite synthesized through arc plasma evaporation and high pressure torsion for H-storage application, Materials Science and Engineering: B 183 (2014) 1-5.

14. R.B. Figueiredo, P.R. Cetlin, T.G. Langdon, Using finite element modeling to examine the flow processes in quasi-constrained high-pressure torsion, Materials Science and Engineering A 528 (2011) 8198-8204.

15. H. Somekawa, T. Mukai, Effect of grain boundary structures on grain boundary sliding in magnesium, Materials Letters 76 (2012) 32-35.

16. R.B. Figueiredo, F.S.J. Poggiali, C.L.P. Silva, P.R. Cetlin, T.G. Langdon, The influence of grain size and strain rate on the mechanical behavior of pure magnesium, Journal of Materials Science 51 (2016) 3013-3024.

17. X.G. Qiao, Y.W. Zhao, W.M. Gan, Y. Chen, M.Y. Zheng, K. Wu, N. Gao, M.J. Starink, Hardening mechanism of commercially pure Mg processed by high pressure torsion at room temperature, Materials Science and Engineering A 619 (2014) 95-106.

18. K. Edalati, A. Yamamoto, Z. Horita, T. Ishihara, High-pressure torsion of pure magnesium: Evolution of mechanical properties, microstructures and hydrogen storage capacity with equivalent strain, Scripta Materialia 64 (2011) 880-883.

19. R.B. Figueiredo, S. Sabbaghianrad, A. Giwa, J.R. Greer, T.G. Langdon, Evidence for exceptional low temperature ductility in polycrystalline magnesium processed by severe plastic deformation, Acta Materialia 122 (2017) 322-331.

20. M. Khajouei-Nezhad, M.H. Paydar, R. Ebrahimi, P. Jenei, P. Nagy, J. Gubicza, Microstructure and mechanical properties of ultrafine-grained aluminum consolidated by high-pressure torsion, Materials Science and Engineering A 682 (2017) 501-508.

21. J.M. Cubero-Sesin, Z. Horita, Powder consolidation of Al–10wt% Fe alloy by High-Pressure Torsion, Materials Science and Engineering A 558 (2012) 462-471.

22. T. Tokunaga, K. Kaneko, Z. Horita, Production of aluminum-matrix carbon nanotube composite using high pressure torsion, Materials Science and Engineering A 490 (2008) 300-304.

23. L.R.C. Malheiros, R.B. Figueiredo, T.G. Langdon, Processing different magnesium alloys through HPT, Materials Science Forum 783-786 (2014) 2617-2622.

24. C.L.P. Silva, A.C. Oliveira, C.G.F. Costa, R.B. Figueiredo, M. de Fátima Leite, M.M. Pereira, V.F.C. Lins, T.G. Langdon, Effect of severe plastic deformation on the biocompatibility and corrosion rate of pure magnesium, Journal of Materials Science 52 (2017) 5992-6003.

25. H. Somekawa, T. Mukai, Hall–Petch Breakdown in Fine-Grained Pure Magnesium at Low Strain Rates, Metallurgical and Materials Transactions A 46A (2015) 894-902.

26. Z. Zeng, J.-F. Nie, S.-W. Xu, C. H. J. Davies, N. Birbilis, Super-formable pure magnesium at room temperature, Nature Communications 8 (2017) 972.

27. N. A. Fleck, G. M. Muller, M. F. Ashby, J. W. Hutchinson, Strain gradient plasticity: theory and experiment, Acta Metallurgica et Materialia 42 (1994) 475-487.

Chapter 5.

Inverse Hall-Petch behaviour in an AZ91 alloy and in an AZ91 – Al_2O_3 composite consolidated by high-pressure torsion

Moara M. Castro[1], Pedro Henrique R. Pereira[1], Augusta Isaac[1], Terence G. Langdon[2], Roberto B. Figueiredo[1]

[1] Department of Metallurgical and Materials Engineering,
Universidade Federal de Minas Gerais, Belo Horizonte, MG 31270-901, Brazil
[2] Materials Research Group, Department of Mechanical Engineering,
University of Southampton, Southampton SO17 1BJ, UK

Abstract: High-pressure torsion (HPT) is a significant procedure for achieving substantial grain refinement but it may be used also to consolidate metallic particles to form bulk samples or composites where two (or more) different phases are mixed and consolidated. An investigation was initiated to examine the consolidation of particles of the magnesium AZ91 alloy and a composite with an AZ91 matrix combined with 1% alumina powder. The results show that a large number of turns is necessary in order to fully consolidate this alloy compared to pure magnesium. As a consequence of the severe plastic deformation, the grain structure was significantly refined with average grain sizes of ~120 and ~100 nm in the unreinforced alloy or ~80 nm in the composite after 20 or 50 HPT turns, respectively. This grain refinement is associated with a decrease in hardness and an increase in the strain rate sensitivity due to the onset of a grain boundary diffusion-assisted creep mechanisms at room temperature. The results are consistent with the theoretical prediction of a breakdown in the Hall-Petch relationship at very small grain sizes.

Keywords: Composites; Hall-Petch breakdown; High-pressure torsion; Magnesium; Particle consolidation.

5.1. Introduction

High-pressure torsion (HPT) is a severe plastic deformation technique that has been widely used to process bulk metallic materials promoting grain refinement and increased strength. In addition to the processing of bulk samples, HPT has been used also to process particles and powders by promoting their consolidation. Early reports examined the consolidation of pure aluminum and copper [1, 2], a nanocrystalline alloy [3, 4] and amorphous alloys [4-8]. It is also possible to incorporate hard phase particles into the metals producing metal-matrix composites [1, 2, 9-13] which usually display improved strength compared to their metal counterparts.

There are recent reports on the consolidation of magnesium by HPT [14-18] and a Mg-10% Al_2O_3 composite with improved hardness compared to pure magnesium [19]. Nevertheless, the hardness of the Mg-Al_2O_3 composite (~65 Hv) was relatively low compared to conventional magnesium-based alloys. The low strength of pure magnesium matrix composites may be attributed to the existence of an inverse Hall-Petch behavior in this material [20] which limits the increase in strength due to grain refinement. Such break in the Hall-Petch relationship has not been reported in a magnesium alloy so far. A recent review of the HPT processing of magnesium and its alloys showed that hardness values in the range of ~120 – 130 Hv are obtained in commercial alloys after HPT processing [21]. Thus, higher hardness is expected in a reinforced composite with a magnesium alloy matrix. In fact, a Mg-2% Zn alloy matrix composite, produced by melting, and then processed by HPT [22], displayed a higher hardness than a pure magnesium matrix composite. Accordingly, the present research was designed to investigate the potential for producing a magnesium alloy matrix composite reinforced with hard particles using cold-consolidation by HPT and to evaluate the validity of the Hall-Petch relationship in the ultrafine-grained range in a representative magnesium alloy.

5.2. Experimental material and procedures

The materials used in the present experiments were an AZ91 alloy and Al_2O_3 as coarse and fine particles, respectively. Figure 5.1 shows scanning electron microscopy (SEM) images of the two starting materials and this shows that the particles of AZ91 were elongated with the major axis having hundreds of microns

whereas the individual Al_2O_3 particles were much finer than 1 micron but with the presence of some agglomeration.

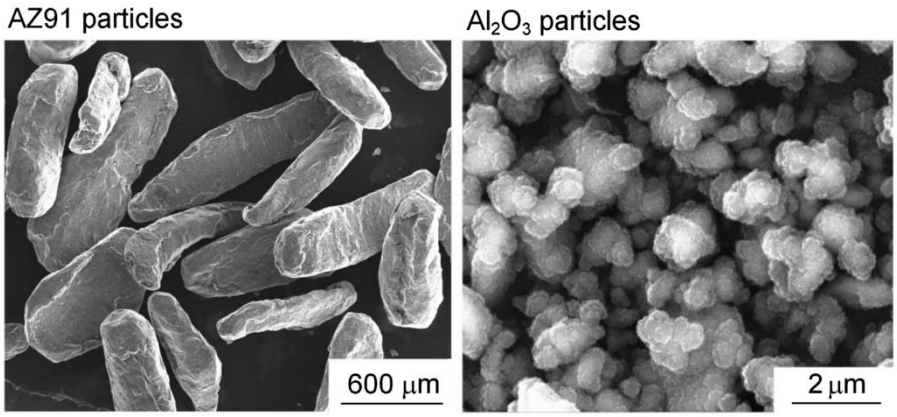

Figure 5.1 – Particles of AZ91 and Al_2O_3 used to produce the composites.

Initial attempts to produce a composite with 10% (in weight) of the reinforcement phase led to significant agglomeration of the alumina phase and generally a poor consolidation of the AZ91 matrix. Therefore, an AZ91-1% Al_2O_3 mix was prepared using a rotating container, and then cold pressing at ~400 MPa into discs of ~1 mm thickness and ~10 mm diameter. These discs were processed through a total *N*, of 50 turns of HPT under a nominal pressure of 6.0 GPa using quasi-constrained anvils [23]. A similar procedure was used to produce discs of AZ91 without a reinforcement phase which were processed to either 20 or 50 turns of HPT, respectively.

The consolidation was evaluated by observing the polished longitudinal sections of the discs using optical microscopy (OM) and SEM. The discs were ground using abrasive papers (#600, #1000 and #4000), polished using diamond pastes (3 μm and 1 μm) and a final polishing step using colloidal silica solution (OPS) provided mirror-like finishes Dynamic hardness tests (using Shimadzu DUH-211 equipment) were used to determine the hardness and the overall creep behaviour at room temperature. A Berkovich indenter was used in these tests and the load, time and penetration depth were tracked. The hardness was determined without any dwell time using a maximum load of 100 mN. The creep behaviour was evaluated using a dwell time of 1000 s. The indenter depth, the time and the instantaneous hardness were used to estimate the instantaneous stress and strain rate. Detailed descriptions of the procedures are given elsewhere [24-26]. Additional Vickers hardness tests were carried out using a load of 50 gf and a dwell time of 10 s.

These hardness tests were performed along the longitudinal plane and care was taken to track the distance of each indentation to the disc centre and bottom of the disc.

The microstructures of the HPT-processed discs were examined using transmission electron microscopy (TEM). Transparent lamellae were prepared using focus ion beam (FIB) milling and they were extracted at areas ~4 mm from the disc centres. The grain size distributions were determined by measuring the mean diameter of at least 150 individual grains.

5.3. Experimental results

Observations using OM revealed full consolidation of the AZ91-1% Al_2O_3 composite and the pure AZ91 discs. The boundaries between the initial AZ91 coarse particles, which were visible after low numbers of turns of HPT, became indistinguishable after 20 turns of HPT processing for the pure AZ91 discs and after 50 turns for the composite. Figure 5.2 shows SEM images of the longitudinal sections at areas near the mid-radius positions of the AZ91 and the AZ91-1% Al_2O_3 work-pieces after processing through 50 HPT turns. Both materials display a continuous matrix with β-phase precipitates but the composite also exhibits dispersed alumina particles. Some agglomeration of the alumina particles takes place in isolated areas. Both the β-phase and the alumina particles are reasonably dispersed throughout the metallic matrix and the separations between them are within the range of several microns.

Figure 5.3 shows representative TEM images of the grain structure of the AZ91 samples processed to 20 and 50 turns and the AZ91-1% Al_2O_3 composite processed to 50 turns. The grain refinement in the AZ91 alloy does not saturate after 20 turns and there is a slight additional decrease in grain size with further processing to 50 turns. The distribution of grain sizes for these materials is presented in Fig. 3.4 in terms of the number frequency plotted against the grain diameter. The AZ91 alloy and the composite contain grains within the range of ~20-220 nm but there is a clear trend of decreasing grain size with increasing numbers of rotations in the AZ91 alloy. The majority of grains lies within the range of ~80-140 nm after 20 turns and within the range of ~60-120 nm after 50 turns. The AZ91-1% Al_2O_3 composite exhibits the finest structure with most of the individual grain diameters within the interval of ~40-100 nm. The average grain sizes were ~120

and ~100 nm for the AZ91 alloy after 20 and 50 turns of HPT and ~80 nm for the composite after processing through 50 turns of HPT, respectively.

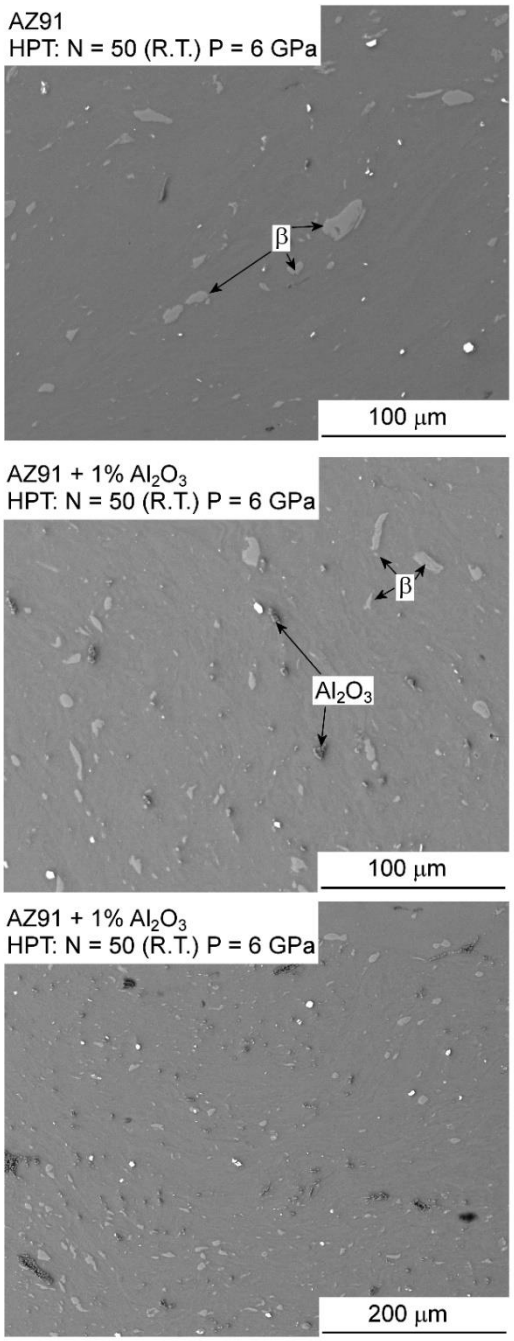

Figure 5.2 – SEM images of the mid-radius area of the AZ91 alloy and the AZ91 + 1% Al_2O_3 composite processed to 50 turns of HPT.

Figure 5.5 presents colour-coded displays of the hardness distributions along longitudinal sections of the discs for different experimental conditions. These distributions tend to be reasonably homogeneous with isolated areas of hardness slightly different from their surroundings. A comparison of the two upper

distributions shows that the hardness of the AZ91 alloy decreases after 50 turns compared to the 20 turns material. This is unexpected due to the higher imposed strain and the finer grain size after 50 turns. Also unexpectedly, the hardness of the composite is significantly lower than the unreinforced alloy.

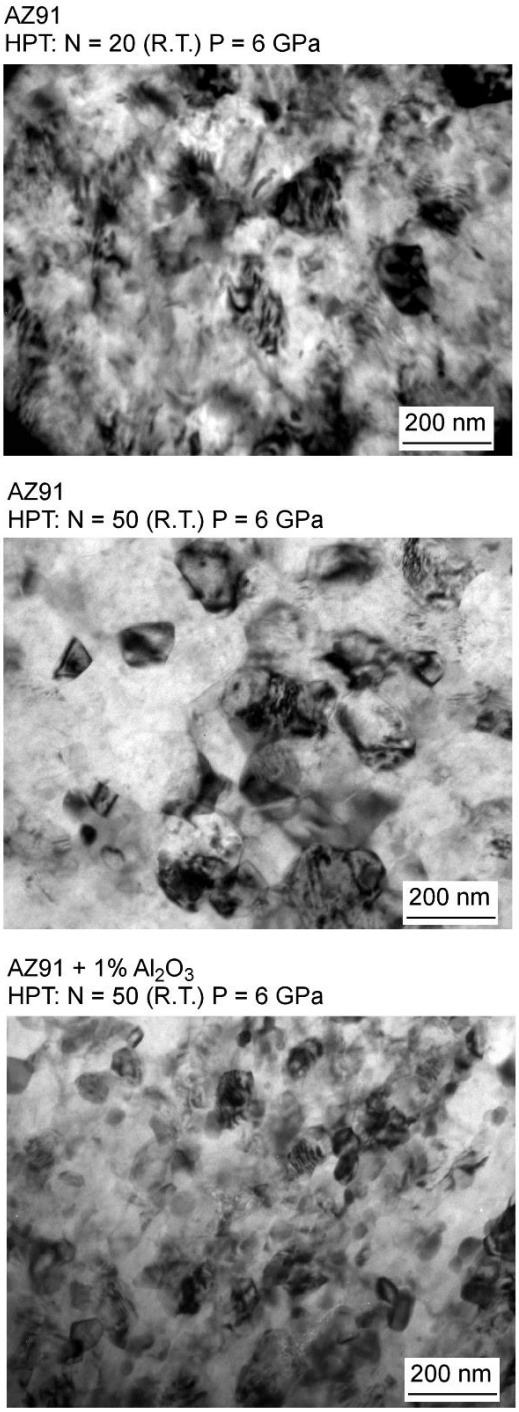

Figure 5.3 – Representative TEM images of the grain structure of the AZ91 alloy processed to 20 and 50 turns and the AZ91 + 1% Al_2O_3 composite processed to 50 turns of HPT.

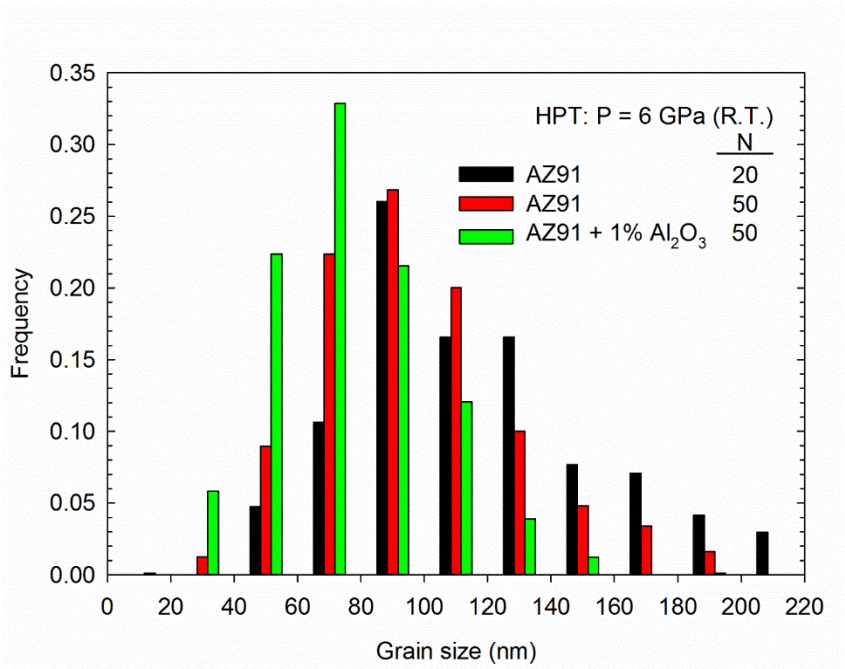

Figure 5.4 – Grain size distribution of the AZ91 alloy and the AZ91 + 1% Al_2O_3 composite after HPT consolidation and processing.

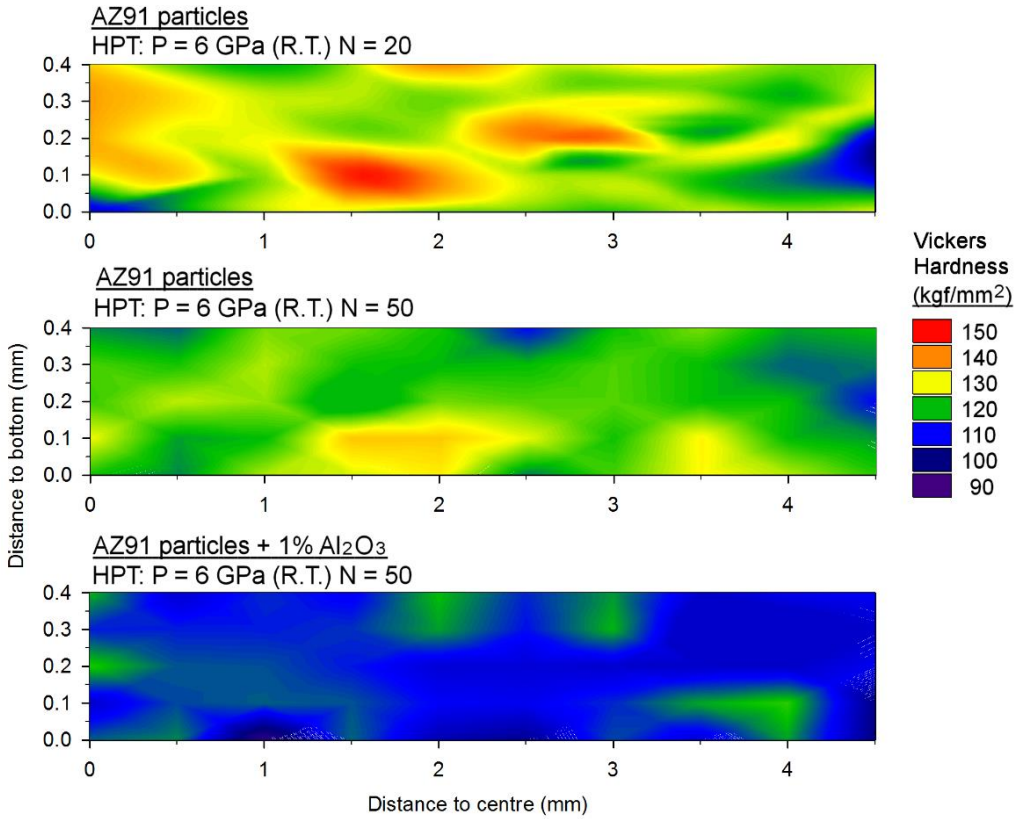

Figure 5.5 – Hardness distribution along the longitudinal section of the AZ91 alloy and the AZ91 + 1% Al_2O_3 composite.

In order to ease the observation of any trends in the hardness evolution with increasing torsional straining, the hardness values determined using Vickers hardness and dynamic hardness testing are plotted as a function of the strain as shown in Fig. 5.6 where the strain was estimated as the effective strain in torsion [27]. From these plots, there is a clear trend of decreasing hardness with increasing strain for both the alloy and the composite and this tendency is observed in both (a) the dynamic testing and (b) the Vickers hardness measurements. Furthermore, the hardness of the composite is consistently lower than the unreinforced alloy at all strains.

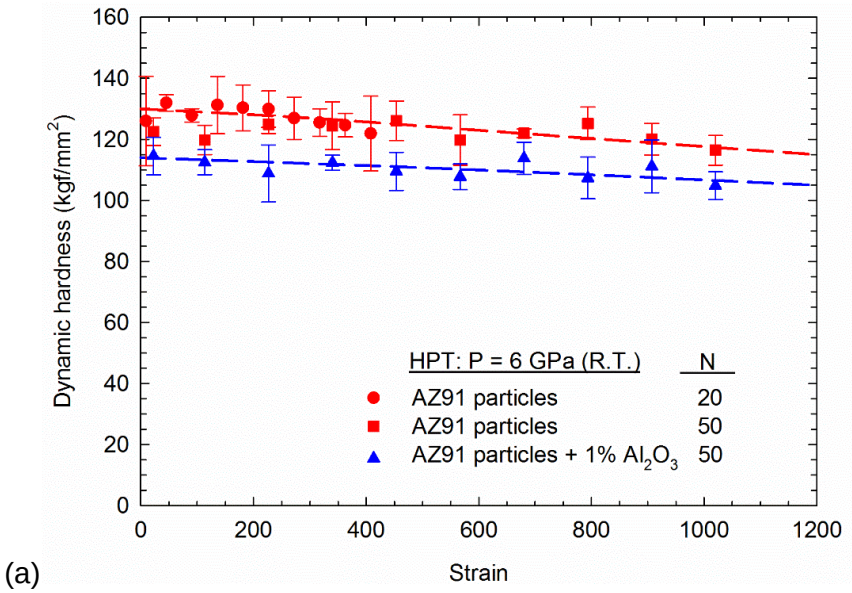

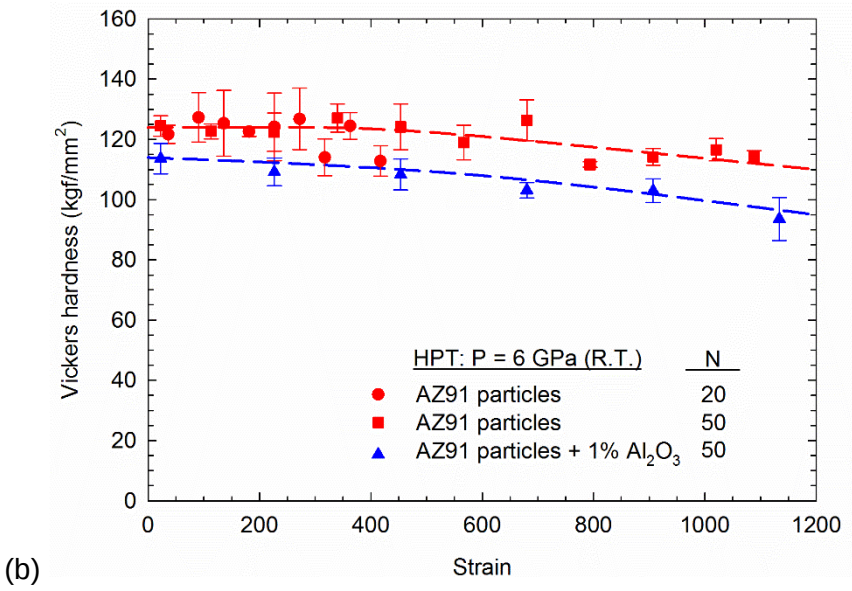

Figure 5.6 – (a) Dynamic hardness and (b) Vickers hardness plotted as a function of the effective strain for the AZ91 alloy and the AZ91 + 1% Al_2O_3 composite.

The flow stress is plotted as a function of the strain rate in Fig. 5.7 for room temperature indentation creep tests in the AZ91 alloy processed to 20 turns and for the composite processed to 50 turns. The flow stress of the composite is lower compared to the AZ91 alloy which is consistent with the hardness tests despite the finer grain structure in the composite. Both materials exhibit high strain rate sensitivities, *m*, with values over 0.060. An earlier report documented a value of *m* ≈ 0.004 for the room temperature strain rate sensitivity of the AZ91 alloy [28] which is over one order of magnitude lower than the values observed in the nanostructured materials in the present investigation.

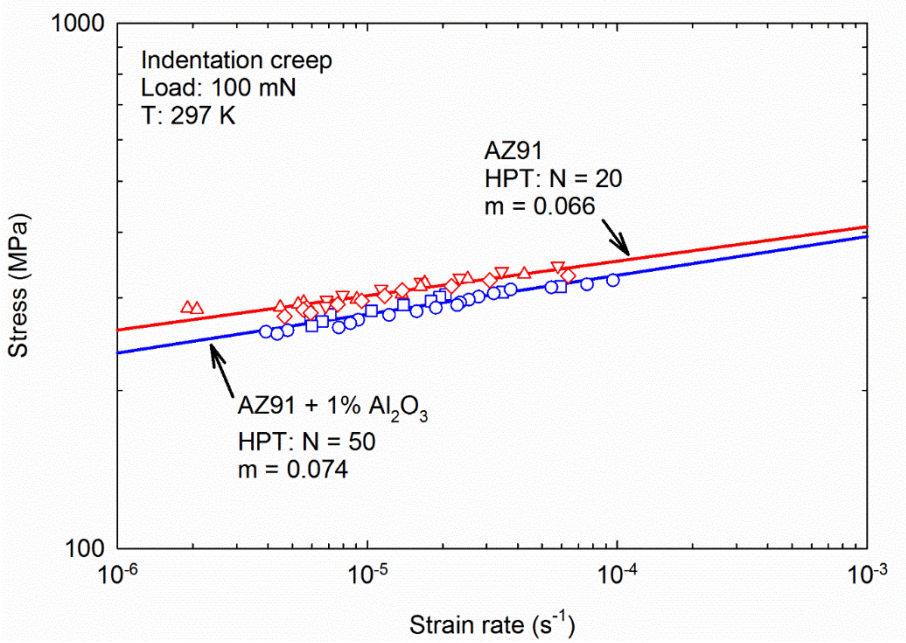

Figure 5.7 – Flow stress as a function of the strain rate determined by room temperature creep testing of the AZ91 alloy and the AZ91 + 1% Al_2O_3 composite.

5.4. Discussion

The results from these tests show that it is feasible to consolidate particles of a magnesium AZ91 alloy into a bulk disc after 20 turns and to incorporate hard ceramic particles to produce a composite after 50 turns of HPT. Earlier attempts to consolidate machining chips of the AZ91 alloy combined with 10% Al_2O_3 particles failed to produce dense billets after only 5 turns of HPT [17]. However, in a later investigation, it was shown that pure magnesium chips and alumina particles can be consolidated into a bulk sample after 5 turns of HPT [19]. In practice, there are many reports of the consolidation of aluminium and copper powders, with and without reinforcement particles, after 5 turns of HPT [1, 2, 29, 30]. This

demonstrates, therefore, that the AZ91 alloy is more difficult to consolidate than pure magnesium, pure aluminium and pure copper, but a full consolidation may be attained by imposing larger numbers of HPT turns.

It is generally accepted that the grain refinement in magnesium alloys saturates after a few turns and this is associated with saturation in the hardness evolution. However, the present results show that grain refinement continues even after 20 turns of HPT in the AZ91 alloy. Moreover, the grain size in the composite is smaller than in the unreinforced metal processed to the same number of turns. It is known that the presence of hard particles induces the formation of local flow heterogeneities [31, 32] and strain gradients [33] which may increase the overall deformation in the matrix. Therefore, the matrix in the AZ91 + 1% Al_2O_3 composite undergoes a larger plastic deformation than the unreinforced alloy counterpart despite the similar numbers of turns in HPT. As a consequence, the composite exhibits a finer grain structure which agrees with the tendency for increasing grain refinement with increasing strain in the AZ91 alloy.

The widely known Hall-Petch relationship states that the material strength increases with grain refinement. Nevertheless, the current experiments, as documented in Figs 5.5 and 5.6, clearly show the opposite trend. Specifically, the hardness of the AZ91 alloy decreased after 50 turns compared to the sample processed to 20 turns and the former displayed a finer grain size than the latter. Also, the composite, although having the finest grain structure, displays the lowest hardness. This clearly demonstrates a breakdown in the conventional Hall-Petch relationship. It is worth noting that the incorporation of hard ceramic particles was expected to increase the strength of the material. However, the distance between the particles is many times larger than the grain size in the processed composite. Therefore the grain boundaries are the major barrier to slip propagation and the Al_2O_3 particles are not expected to significantly affect the hardness.

Such a breakdown at room temperature has been reported in pure magnesium for much larger grain sizes and attributed to the onset of grain boundary sliding [20, 24]. For example, it was found that the activation energy for grain boundary diffusion was significantly lower than expected and this gave an enhanced grain boundary diffusivity. Furthermore, a decreasing hardness with decreasing grain size is expected in nanocrystalline materials due to the occurrence of diffusional creep [34] but this effect has not been observed in a magnesium alloy processed

by HPT. A recent review showed that Hall-Petch holds for magnesium alloys and a reverse Hall-Petch was not considered due to the difficulties in obtaining magnesium with very fine grains [35].

In order to evaluate the occurrence of a Hall-Petch breakdown due to grain boundary sliding and/or diffusional creep, the flow stress, σ, of the AZ91 alloy was collected from numerous reports [36-44] and then plotted as a function of the grain size, d, in Fig. 5.8 for a broad range of grain sizes. With the objective of comparing the Vickers hardness values, *Hv*, and the flow stress, σ, determined by tensile tests, the relationship of $\sigma = Hv/3$ was used to convert hardness to stress [45]. Although this relationship may tend to overestimate the flow stress calculated from hardness data for large grains, this discrepancy decreases with decreasing grain size and there tends to be an excellent agreement for grain sizes <1 μm [40].

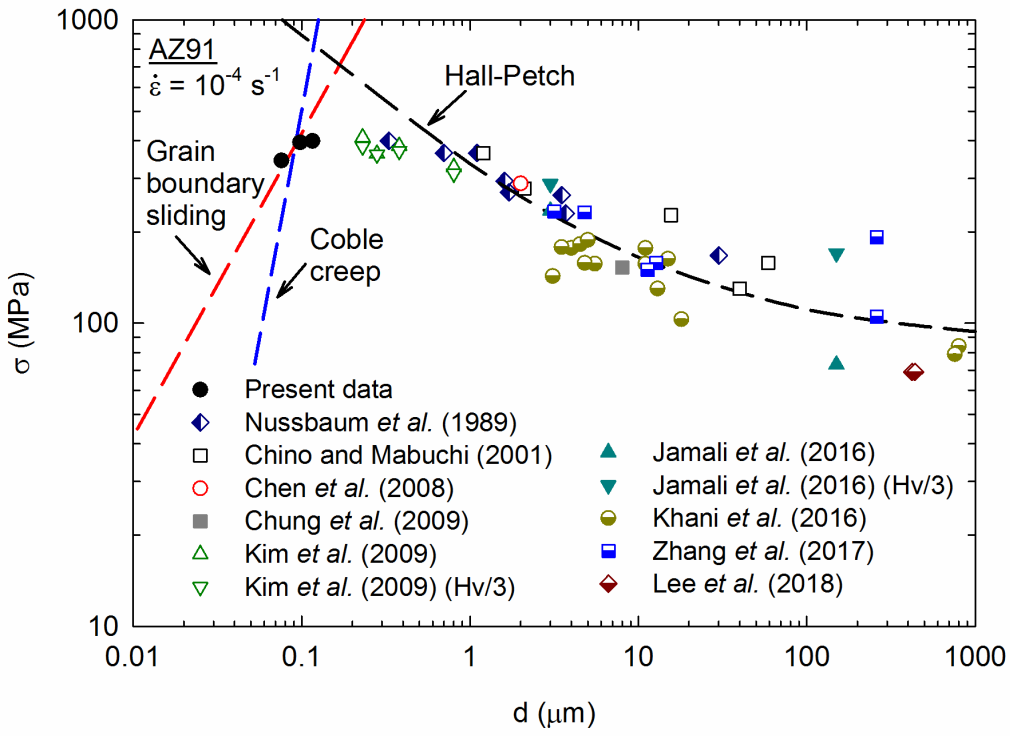

Figure 5.8 – Flow stress plotted as a function of the grain size [36-44].

As shown in Fig. 5.8, there is a general trend of decreasing flow stress with increasing grain size for large grain sizes and this is in agreement with the Hall-Petch relationship. Accordingly, a trend line for this relationship was plotted in Fig. 5.8 using the following expression:

$$\sigma = 86\ MPa + 250\ MPa\ \mu m^{1/2}\ d^{-1/2} \qquad \text{(eq. 1)}$$

Thus, the Hall-Petch relationship is no longer followed for grain sizes <1 μm where the slope changes in Fig. 5.8. It is worth noting that a decrease in the Hall-Petch slope for grain sizes < 2 μm was reported for an AZ31 alloy [46]. Moreover, a deviation from the Hall-Petch trend for a sample with the finest grain size (0.33 μm) was reported in an AZ91 alloy processed by rapid solidification [44]. The data in Fig. 5.8 shows the flow stress does not vary significantly for grain sizes in the range from ~0.1 to 1.0 μm and instead there is an inverse trend of decreasing flow stress with decreasing grain size for grain sizes that are smaller than ~100 nm.

The theoretical predictions for these mechanisms are also included at the smaller grain sizes in Fig. 5.8 for comparison purpose. These predictions were based on creep mechanisms developed for Coble diffusion creep where vacancy flow occurs along the grain boundaries [41] and grain boundary sliding [42] and the relevant relationships are given as follows:

$$\sigma = \dot{\varepsilon}_{Coble}\left(\frac{kT}{66.8\delta D_{gb}}\right)\left(\frac{d}{b}\right)^3 \qquad \text{(eq. 2)}$$

$$\sigma = \left(\frac{\dot{\varepsilon}_{gbs}kTG}{10\delta D_{gb}}\right)^{1/2}\left(\frac{d}{b}\right) \qquad \text{(eq. 3)}$$

where k is Boltzmann's constant, T is the absolute temperature, δ is the grain boundary width, D_{gb} is the grain boundary diffusion coefficient, b is the Burgers vector modulus and G is the shear modulus, and $\dot{\varepsilon}_{Coble}$ and $\dot{\varepsilon}_{gbs}$ are the strain rates for the Coble and grain boundary sliding mechanisms, respectively. A reasonable and relevant strain rate of 10^{-4} s^{-1} was taken for both mechanisms and for this strain-rate the Hall-Petch relationship is expected to be valid for grain sizes of ~200 nm and larger. The flow stresses for the creep mechanisms are lower for nanostructured alloys and this directly explains the inverse trends observed in the present experiments.

Also, although coarse-grained magnesium displays a low strain-rate sensitivity at room temperature, the creep mechanisms are associated with relatively high values of m. The present experiments show there is a significant increase in the strain rate sensitivity which also corroborates the contribution of creep to room temperature plastic deformation for the nanostructured alloy.

A similar trend was reported in pure magnesium processed by ball milling and consolidated through hot extrusion [43]. Thus, compression tests showed that the Hall-Petch relationship was valid for grains larger than ~1 μm but there was a reduction in slope for grains within the range of ~100 nm – 1 μm and then a negative slope for grain sizes below ~100 nm. An increase in the strain rate sensitivity was reported up to ~0.08 with decreasing grain size.

The continuous decrease in hardness with increasing deformation in HPT is associated with the continuous decrease in grain size which activates grain boundary diffusion assisted creep mechanisms such as grain boundary sliding and Coble creep. A similar reduction in hardness after very high straining in HPT was reported in a Mg-3.4% Zn alloy with a grain size of ~140 nm [47]. This suggests that the breakdown in the Hall-Petch relationship at grain sizes in the range of ~100 nm is also valid for other magnesium alloys. By contrast, a higher strength was reported in a Mg-2% Zn alloy / 14% SiC composite processed by HPT despite a very small grain size of ~64 nm compared to the unreinforced alloy with a grain size of ~105 nm [22]. Although this appears to contradict the present results, the composite displayed a homogeneous distribution of nano-precipitates which may hinder grain boundary sliding and thereby extend the range for conventional Hall-Petch behaviour. The composite in the current investigation contained fewer hard particles and the separation between them was very high. This suggests they were not effective in restraining any grain boundary sliding. Thus, it appears that the major effect of the hard particles in the present experiments is to increase the amount of deformation imposed to the matrix due to local flow heterogeneities.

5.5. Summary and conclusions

1. Bulk discs of AZ91 and AZ91 + 1% Al_2O_3 were successfully produced by consolidation of particles through high-pressure torsion. The number of turns required for consolidation was higher than in pure magnesium and other metallic materials.

2. The grain size decreases continuously with increasing deformation and a minimum grain size of ~80 nm was achieved in the composite after 50 turns of HPT.

3. The hardness decreases with increasing strain and the strain rate sensitivity increases. It is shown that these effects are associated with the onset at room temperature of a grain boundary diffusion-assisted creep mechanisms such as Coble diffusion creep or grain boundary sliding.

5.6. Author contributions

M.M.C. contributed to sample preparation and microstructure analysis, carried out hardness and dynamic hardness tests, and prepared the first draft of the manuscript.

5.7. Acknowledgements

The authors would like to acknowledge the Center of Microscopy at the Universidade Federal de Minas Gerais (http://www.microscopia.ufmg.br) for providing the equipment and technical support for experiments involving electron microscopy. RBF acknowledges financial support from CNPq (grant #400407/2016-7), FAPEMIG (grant #APQ-00580-15) and Serrapilheira Institute (grant #Serra-1709-17750). PHRP acknowledges support from CNPq (grant #443736/2018-9).

5.8. References

1. I.V. Alexandrov, Y.T. Zhu, T.C. Lowe, R.K. Islamgaliev, R.Z. Valiev, Nanostructured Materials, 10 (1998) 45-54.
2. I.V. Alexandrov, R.K. Islamgaliev, R.Z. Valiev, Y.T. Zhu, T.C. Lowe, Metallurgical and Materials Transactions A, 29 (1998) 2253-2260.
3. Z. Lee, F. Zhou, R.Z. Valiev, E.J. Lavernia, S.R. Nutt, Scripta Materialia, 51 (2004) 209-214.
4. W.J. Botta, J.B. Fogagnolo, C.A.D. Rodrigues, C.S. Kiminami, C. Bolfarini, A.R. Yavari, Materials Science and Engineering: A, 375-377 (2004) 936-941.
5. J. Sort, D.C. Ile, A.P. Zhilyaev, A. Concustell, T. Czeppe, M. Stoica, S. Suriñach, J. Eckert, M.D. Baró, Scripta Materialia, 50 (2004) 1221-1225.
6. K. Edalati, Y. Yokoyama, Z. Horita, Materials Transactions, 51 (2010) 23-26.
7. H. Asgharzadeh, S.-H. Joo, J.-K. Lee, H.S. Kim, Journal of Materials Science, 50 (2015) 3164-3174.

8. A.R. Yavari, W.J. Botta, C.A.D. Rodrigues, C. Cardoso, R.Z. Valiev, Scripta Materialia, 46 (2002) 711-716.

9. T. Tokunaga, K. Kaneko, K. Sato, Z. Horita, Scripta Materialia, 58 (2008) 735-738.

10. K. Edalati, M. Ashida, Z. Horita, T. Matsui, H. Kato, Wear, 310 (2014) 83-89.

11. H. Asgharzadeh, H.S. Kim, 62 (2017) 1109.

12. H. Asgharzadeh, H. Faraghi, H.S. Kim, Acta Metallurgica Sinica (English Letters), 30 (2017) 973-982.

13. Y. Huang, P. Bazarnik, D. Wan, D. Luo, P.H.R. Pereira, M. Lewandowska, J. Yao, B.E. Hayden, T.G. Langdon, Acta Materialia, 164 (2019) 499-511.

14. T. Grosdidier, J.J. Fundenberger, J.X. Zou, Y.C. Pan, X.Q. Zeng, International Journal of Hydrogen Energy, 40 (2015) 16985-16991.

15. S. Panda, J.-J. Fundenberger, Y. Zhao, J. Zou, L.S. Toth, T. Grosdidier, International Journal of Hydrogen Energy, 42 (2017) 22438-22448.

16. S. Panda, L.S. Toth, J.X. Zou, T. Grosdidier, Materials, 11 (2018) 1335.

17. M.M. de Castro, A.P. Carvalho, P.H.R. Pereira, A.C. Isaac Neta, R.B. Figueiredo, T.G. Langdon, Materials Science Forum, 941 (2019) 851-856.

18. E.Y. Yoon, D.J. Lee, T.-S. Kim, H.J. Chae, P. Jenei, J. Gubicza, T. Ungár, M. Janecek, J. Vratna, S. Lee, H.S. Kim, Journal of Materials Science, 47 (2012) 7117-7123.

19. M.M. Castro, P.H.R. Pereira, A. Isaac, R.B. Figueiredo, T.G. Langdon, Journal of Alloys and Compounds, 780 (2019) 422-427.

20. H. Somekawa, T. Mukai, Metallurgical and Materials Transactions A, 46 (2015) 894-902.

21. R.B. Figueiredo, T.G. Langdon, Advanced Engineering Materials, 21 (2019) 1801039.

22. J. Cheng, S. Ghosh, International Journal of Plasticity, 67 (2015) 148-170.

23. R.B. Figueiredo, P.R. Cetlin, T.G. Langdon, Materials Science and Engineering A, 528 (2011) 8198-8204.

24. R.B. Figueiredo, S. Sabbaghianrad, A. Giwa, J.R. Greer, T.G. Langdon, Acta Materialia, 122 (2017) 322-331.

25. R.B. Figueiredo, F.S.J. Poggiali, C.L.P. Silva, P.R. Cetlin, T.G. Langdon, Journal of Materials Science, 51 (2016) 3013-3024.

26. H. Somekawa, T. Mukai, Materials Letters, 76 (2012) 32-35.

27. R.Z. Valiev, Y.V. Ivanisenko, E.F. Rauch, B. Baudelet, Acta Materialia, 44 (1996) 4705-4712.

28. C.D. Lee, Journal of Materials Science, 42 (2007) 10032-10039.

29. A.P. Zhilyaev, A.A. Gimazov, G.I. Raab, T.G. Langdon, Materials Science and Engineering: A, 486 (2008) 123-126.

30. J.M. Cubero-Sesin, Z. Horita, Materials Science and Engineering: A, 558 (2012) 462-471.

31. R. Kulagin, Y. Beygelzimer, Y. Ivanisenko, A. Mazilkin, H. Hahn, Procedia Engineering, 207 (2017) 1445-1450.

32. R. Kulagin, Y. Beygelzimer, Y. Ivanisenko, A. Mazilkin, H. Hahn, IOP Conference Series: Materials Science and Engineering, 194 (2017) 012045.

33. N.A. Fleck, G.M. Muller, M.F. Ashby, J.W. Hutchinson, Acta Metallurgica et Materialia, 42 (1994) 475-487.

34. A.H. Chokshi, A. Rosen, J. Karch, H. Gleiter, Scripta Metallurgica, 23 (1989) 1679-1683.

35. H. Yu, Y. Xin, M. Wang, Q. Liu, Journal of Materials Science & Technology, 34 (2018) 248-256.

36. S. Khani, M.R. Aboutalebi, M.T. Salehi, H.R. Samim, H. Palkowski, Materials Science and Engineering: A, 678 (2016) 44-56.

37. Y. Chino, M. Mabuchi, Advanced Engineering Materials, 3 (2001) 981-983.

38. B. Chen, D.-L. Lin, L. Jin, X.-Q. Zeng, C. Lu, Materials Science and Engineering: A, 483-484 (2008) 113-116.

39. C.W. Chung, R.G. Ding, Y.L. Chiu, M.A. Hodgson, W. Gao, IOP Conference Series: Materials Science and Engineering, 4 (2009) 012012.

40. W.J. Kim, H.G. Jeong, H.T. Jeong, Scripta Materialia, 61 (2009) 1040-1043.

41. S.S. Jamali, G. Faraji, K. Abrinia, Materials Science and Engineering: A, 666 (2016) 176-183.

42. L. Zhang, Q. Wang, W. Liao, W. Guo, B. Ye, H. Jiang, W. Ding, Journal of Materials Science & Technology, 33 (2017) 935-940.

43. J.U. Lee, S.-H. Kim, Y.J. Kim, S.H. Park, Materials Science and Engineering: A, 714 (2018) 49-58.

44. G. Nussbaum, P. Sainfort, G. Regazzoni, H. Gjestland, Scripta Metallurgica, 23 (1989) 1079-1084.

45. P. Zhang, S.X. Li, Z.F. Zhang, Materials Science and Engineering: A, 529 (2011) 62-73.

46. S.M. Razavi, D.C. Foley, I. Karaman, K.T. Hartwig, O. Duygulu, L.J. Kecskes, S.N. Mathaudhu, V.H. Hammond, Scripta Materialia, 67 (2012) 439-442.

47. F. Meng, J.M. Rosalie, A. Singh, H. Somekawa, K. Tsuchiya, Scripta Materialia, 78-79 (2014) 57-60.

Chapter 6.

Consolidation of magnesium and magnesium – quasicrystal composites through high-pressure torsion

Moara M. Castro[1], Witor Wolf[1], Augusta Isaac[1], Megumi Kawasaki[2], Roberto B. Figueiredo[1]

[1] Department of Metallurgical and Materials Engineering, Universidade Federal de Minas Gerais, Belo Horizonte 31270-901, Brazil

[2] Department of Mechanical, Industrial and Manufacturing Engineering, Oregon State University, Corvallis 97331-6001, U.S.A.

Abstract: It is of great interest to produce magnesium-based composites through room temperature consolidation of particles using high-pressure torsion. However, lack of bonding between the particles can compromise the integrity and ductility of such materials. The present work evaluates the microstructure of composites of pure magnesium and a magnesium alloy AZ91 with the incorporation of quasicrystal particles as reinforcement phase. Generalized lack of bonding is observed in the alloy matrix composite and localized lack of bonding in the pure magnesium matrix. High tensile strength might be achieved after consolidation of pure magnesium with and without quasicrystal reinforcement but all samples display limited ductility. This is attributed to pre-existing areas with lack of bonding in the matrix, cracking of the hard particles and lack of bonding between the matrix and the reinforcement particles.

Keywords: Magnesium, Composite, Severe plastic deformation, High-pressure torsion.

6.1. Introduction

Metal matrix composites (MMC) usually display the high strength, toughness and rigidity of metallic materials and incorporates a second phase which improves specific properties and the overall performance in targeted applications. For example, MMCs reinforced with ceramic phases may display improved wear resistance compared to the unreinforced metal. MMCs are usually produced by melting or sintering and these techniques involve a high temperature processing step.

Recent papers have shown that it is possible to produce MMCs, at room temperature, by consolidation of metallic particles through high-pressure torsion (HPT) [1-8]. This severe plastic deformation technique has been widely used to refine the grain structure of metallic materials [9, 10]. Additionally, the high hydrostatic stress and high amount of shear deformation are also effective to break up the surface oxide layer of metallic particles and promote their bonding.

HPT has been used to produce magnesium-based composites with different materials to meet the performance targets. For example, it was shown that the incorporation of alumina particles into pure magnesium matrix promotes a slight increase in hardness and in room temperature creep resistance [11]. Magnesium can also be mixed with pure aluminum to produce a ductile metastable composite which can be hardened by thermal treatment [12]. Also, bioactive materials can be used to produce a bioactive magnesium-based biodegradable composite [13]. Thus, a potential to produce the magnesium-based MMCs with improved performance is apparent. However, a recent paper [13] showed that the tensile behavior of a composite of magnesium with hydroxyapatite is characterized by a high mechanical strength, however, the elongation is significantly reduced compared to pure magnesium processed by HPT [14]. The reason for this lack of ductility in the magnesium-based composite is not clear yet. Also, the majority of reports on consolidation of magnesium-based composites are related to commercially pure magnesium as the matrix material. Despite a report of full consolidation of a Mg-Zn-Y alloy [15], recent attempts to consolidate the AZ91 alloy did not produce sound samples [13, 16]. Thus, the present paper aims to evaluate the tensile behavior of pure magnesium and a magnesium composite consolidated through HPT and to evaluate the effectiveness in consolidation of an AZ91 magnesium alloy. An Al-Cu-Fe icosahedral quasicrystalline alloy produced by gas-

atomization is used as a reinforcement phase in the magnesium-based composites. The fabrication process used here to produce quasicrystalline powders allows obtaining different particle sizes, which facilitates the mixing with the magnesium particles without significant heterogeneity in distribution of phases. Quasicrystalline phases display interesting functional properties such as low friction coefficient, low surface adhesion energy and high hardness [17], which are interesting for tribological protection [18]. These properties are associated to their complex atomic organization [19]. To this date, MMCs reinforced with quasicrystals have been only fabricated by thermally assisted processes, involving solidification [20, 21] or hot consolidation of mechanically mixed powders [22]. In this work, we fabricate this composite by cold consolidation.

6.2. Experimental procedure

The materials used in the present experiments were commercially pure magnesium, AZ91 magnesium alloy and AlCuFe quasicrystal (QC) particles. The QC particles were fabricated by gas-atomization of commercially pure elements (purity > 99%), with nominal atomic composition of $Al_{62.5}Cu_{25}Fe_{12.5}$. Figure 6.1 shows scanning electron microscopy images of the initial materials and the composition of the quasicrystal particles determined by energy dispersive spectroscopy (EDS), being relatively close to the nominal alloy composition.

Fig. 6.1. SEM images of the starting materials used to produce the green discs.

Two composite mixtures were prepared with 80% in weight of metallic particles (magnesium or the alloy) and 20%wt. of quasicrystal particles. The particles were hand mixed and pressed into 10 mm diameter and 1 mm thickness green discs using a pressure of ~400 MPa. Discs of 100% pure magnesium were also pressed using similar procedure. The pressed discs were processed by HPT using a quasi-constrained facility operating with a nominal pressure of 3.8 GPa. Samples were processed to 5, 10 and 20 turns at room temperature.

Processed discs were ground and polished and observed by scanning electron microscopy (SEM). Miniature tensile specimens with 1.5 mm gauge length and 1 mm width were cut from processed discs of pure magnesium and the Mg-20% QC composite. The specimens were ground and polished and the thickness of each specimen varied within the range 0.5 ~ 0.6 mm. Tensile tests were carried out using constant rate of cross-head displacement and an initial strain-rate of 10^{-4} s^{-1}. The load and displacement data were converted to engineering stress and strain. The elastic distortion of the tensile test apparatus was corrected by equating the elastic portion of the curves to the elastic modulus of magnesium. After testing, the specimens were observed using SEM.

6.3. Experimental results

Visual inspection of the HPT processed discs revealed an apparent effective consolidation. Careful examination of the SEM images with low to high magnifications of the Mg-20% QC and AZ91-20% QC composites, exhibited in Figure 6.1, provides clear evidence of their partial consolidation after 10 turns of HPT at room temperature. A large amount of interparticle pores can be detected in the matrix of the AZ91-20% QC composite, which are revealed as continuous frontiers between areas with size compatible to the original particles of AZ91 (hundreds of microns). Additionally, it is observed that the QC particles are well dispersed in the metallic matrix and exhibit a bimodal size distribution. Whereas most of the QC particles is still in the range of hundreds of microns, few particles have size in the order of tens of microns as a result of the fragmentation during the HPT processing. Differently from the generalized lack of consolidation in the AZ91-20% QC composite, the Mg-20% QC sample displays a small amount of interparticle pores suggesting localized lack of consolidation.

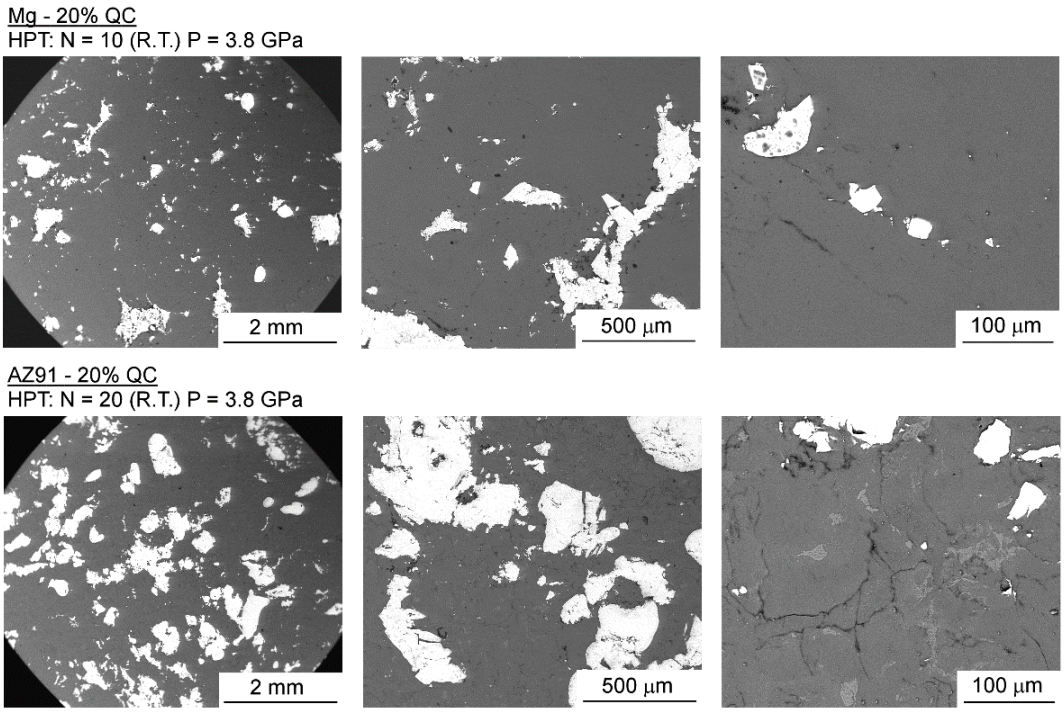

Fig. 6.1. Microstructure of the Mg-20% QC and AZ91-20% QC composites processed to 10 turns of HPT.

Figure 6.3 shows the stress vs strain curves obtained by tensile testing of pure magnesium and the Mg-20% QC composite processed to different number of turns. Each test was repeated and the difference between the ultimate stress and final elongation was within 10% for all conditions. It is observed that the discs of pure magnesium do not display significant difference in strength and elongation with varying number of turns. Also, the flow and ultimate stresses are higher than those observed in bulk pure magnesium processed by HPT [14, 23]. On the other hand, the elongation is significantly lower. In practice, the Mg-20% QC composite after 5 turns of HPT displayed about 50% of the ultimate stress obtained for the pure magnesium subjected to the same processing conditions, suggesting the relatively lower level of consolidation. The strength increases significantly after 10 turns suggesting improved consolidation. However, further processing to 20 turns reduces the strength of the composite. It is worth noting that the flow curve of the composite processed by 20 turns does not display a stage of apparent hardening, which was observed in all other samples. This suggests that the material is the most brittle among all samples and the fracture at low stress can be attributed to such less strain hardening.

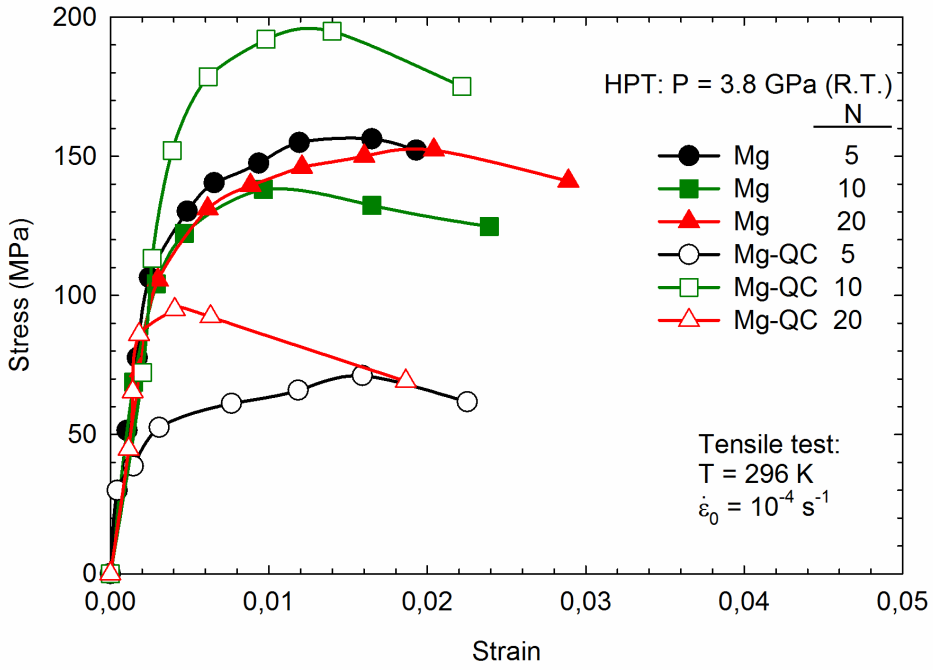

Fig. 6.3. Stress vs strain curves of the pure magnesium and the Mg-20% QC composite consolidated by different number of turns of HPT.

Both the pure magnesium and the Mg-20% QC composite exhibit very limited ductility. The elongations were ~2% only in all specimens. This is unexpectedly low for magnesium processed by HPT since the processing of bulk pure magnesium leads to extraordinary ductility after only 1/2 turn [24]. The surfaces of the tested specimens were observed in SEM and Figs. 6.4 and 6.5 show the representative images of the pure magnesium and the composite, respectively. The surfaces of the pure magnesium specimens show no evidence of plastic deformation within the gauge length which corroborates with the almost brittle behavior observed in the stress-strain curves. Slip bands were observed in different locations of the gauge length which shows a high tendency for localized deformation. Also, cracks were observed in areas far from the rupture surface. These cracks did not develop due to the reduced deformation but they confirm that consolidation was not complete.

The specimens of Mg-20% QC composite contained some QC particles with over 100 μm within the gauge length. The images on the left hand side of Fig. 6.5 show the area of the specimens head and a gradual decrease in the size of the QC particles with increasing the number of turns is observed. These particles could nucleate cracks and the image on the top right shows a coarse QC particle in the

fracture tip of the specimen. Also, cracking of the QC particles and a lack of continuity of these particles with the magnesium matrix were observed. The image at the middle and on the right-side shows an evidence of both. These could nucleate cracks and reduce the tensile ductility of the composite which agrees with the low elongations observed in tensile tests.

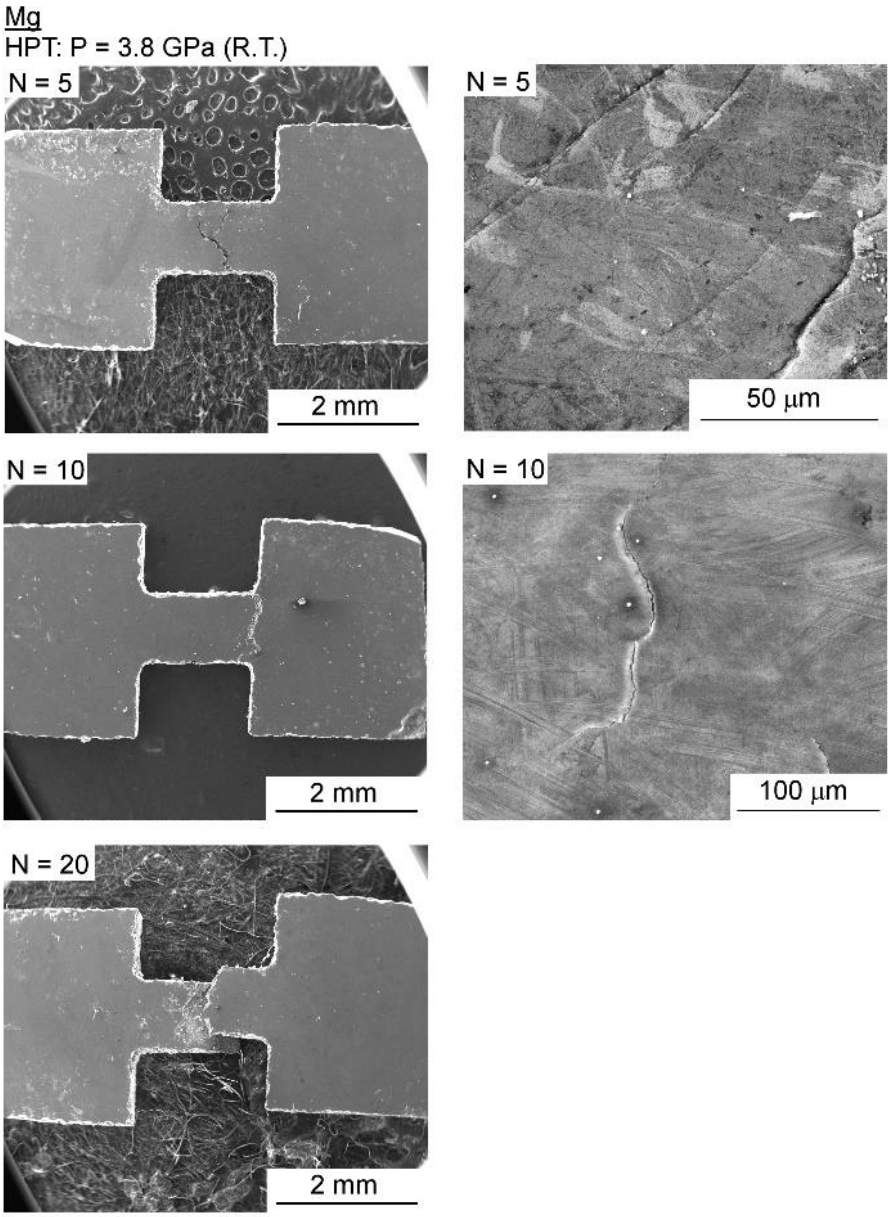

Fig. 6.4. Representative images of the tensile specimens of pure magnesium consolidated by HPT and tested to failure.

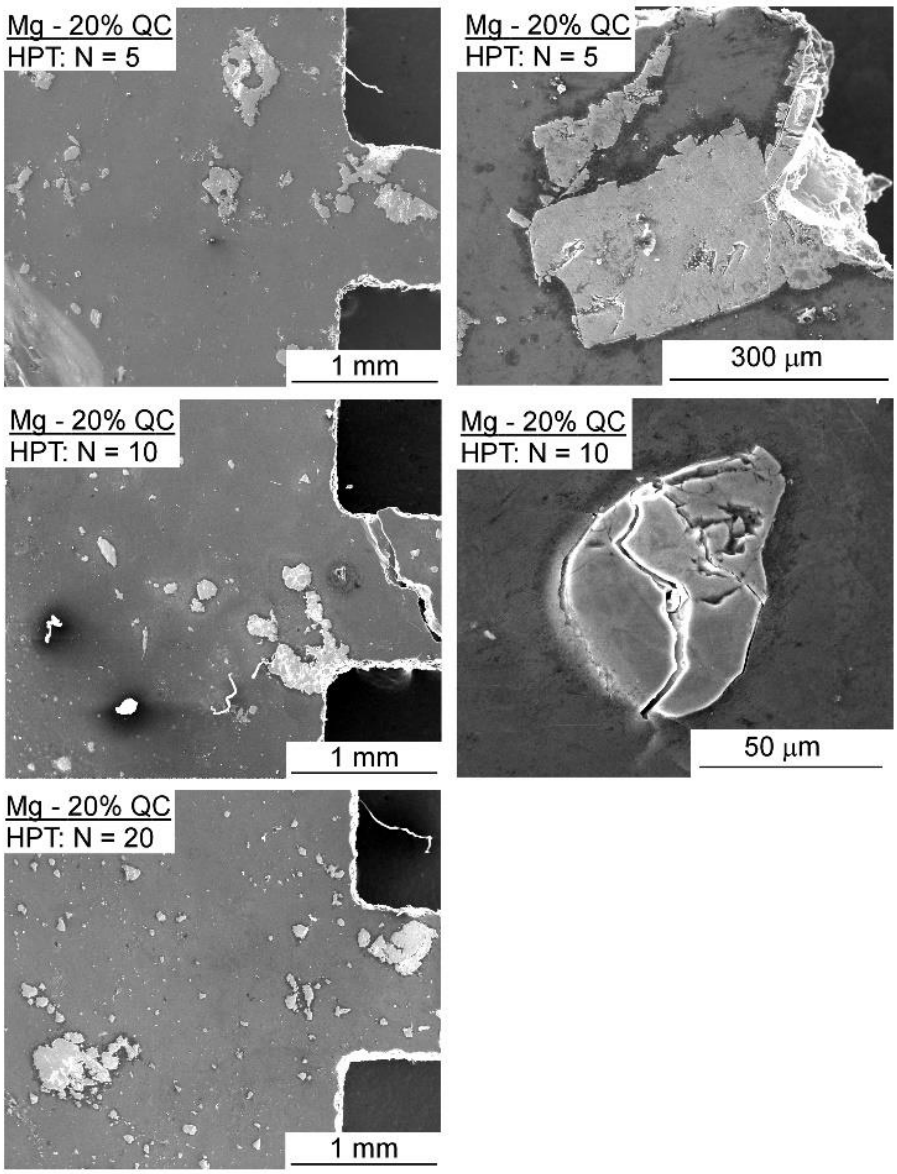

Fig. 5.5. Representative images of the tensile specimens of Mg-20% QC composite consolidated by HPT and tested to failure.

6.4. Discussion

The consolidation of metallic particles through HPT requires a high pressure to promote plastic deformation and full contact between the particles and high shear strain to break up the oxide surface layer and promote chemical bonding between the metals. Thus, it is expected that hard materials will have a difficulty to be consolidated due to the increased resistance against plastic deformation. Also, the thickness and resistance of the oxide layer is expected to affect the consolidation. The present results confirm that the AZ91 alloy is difficult to consolidate in comparison with pure magnesium. Composites with similar amount of hard

quasicrystal particles could be consolidated by 10 turns of HPT using pure magnesium as matrix material but not with AZ91. It is worth noting that previous studies have shown that pure magnesium chips, pure or with the addition of alumina particles, could be consolidated after 5 turns of HPT [11, 16]. On the other hand, machining chips of AZ91 were not consolidated in the same conditions [16]. Also, a recent paper showed the lack of consolidation of an AZ91-Bioactive Glass composite even after 50 turns of HPT [13].

Furthermore, the present results suggest that consolidation is not completed in pure magnesium discs and Mg-20% QC composite. This can be attributed to the heterogeneity of plastic deformation during HPT processing of magnesium [25-27]. Thus, some volumes of the sample might not undergo sufficient shear straining to promote bonding between the particles. Areas with the lack of consolidation can act as pre-existent cracks in the processed discs and compromise the tensile ductility of the material as shown in the present tensile tests. This explains the limited elongations observed in all samples of pure magnesium and Mg-20% QC composite.

6.5. Summary and Conclusions

1. Commercial purity magnesium and the AZ91 alloy particles were mixed with quasicrystal particles and processed by HPT. The processed discs were observed in SEM. Tensile tests were carried out in the Mg-QC composite and in samples of pure magnesium particles processed by HPT.

2. SEM images show significant consolidation of pure magnesium with quasicrystal particles and general lack of consolidation when using the AZ91 alloy as matrix material.

3. Pure magnesium consolidated by HPT display higher strength but reduced ductility compared to bulk pure magnesium processed by HPT. The brittle behavior is attributed to pre-existing cracks due to localized lack of bonding.

4. Mg-20% QC composite processed to 10 turns display high strength but limited ductility. The limited ductility is attributed to cracking of the coarse quasicrystal particles and lack of bonding between the reinforcement phase and the matrix.

6.6. Author contributions

M.M.C. carried out sample preparation, HPT processing, tensile tests, contributed to microstructure characterization and prepared the first draft of the manuscript.

6.7. Acknowledgements

RBF acknowledges financial support from CNPq (grant #400407/2016-7), FAPEMIG (grant #APQ-00580-15) and Serrapilheira Institute (grant #Serra-1709-17750). MMC received a research fellowship from CAPES.

6.8. References

1. H. Asgharzadeh, S.-H. Joo, J.-K. Lee, H.S. Kim, Journal of Materials Science, **50,** 3164-3174 (2015). 10.1007/s10853-015-8877-4
2. M. Ashida, Z. Horita, T. Kita, A. Kato, Materials Transactions, **53,** 13-16 (2012). 10.2320/matertrans.MD201128
3. W. Xu, X. Wu, T. Honma, S.P. Ringer, K. Xia, Acta Materialia, **57,** 4321-4330 (2009).
4. A.P. Zhilyaev, A.A. Gimazov, G.I. Raab, T.G. Langdon, Materials Science and Engineering: A, **486,** 123-126 (2008).
5. W.J. Botta, J.B. Fogagnolo, C.A.D. Rodrigues, C.S. Kiminami, C. Bolfarini, A.R. Yavari, Materials Science and Engineering: A, **375-377,** 936-941 (2004).
6. Z. Lee, F. Zhou, R.Z. Valiev, E.J. Lavernia, S.R. Nutt, Scripta Materialia, **51,** 209-214 (2004).
7. I.V. Alexandrov, Y.T. Zhu, T.C. Lowe, R.K. Islamgaliev, R.Z. Valiev, Nanostructured Materials, **10,** 45-54 (1998).
8. I.V. Alexandrov, R.K. Islamgaliev, R.Z. Valiev, Y.T. Zhu, T.C. Lowe, Metallurgical and Materials Transactions A, **29,** 2253-2260 (1998).
9. R.B. Figueiredo, T.G. Langdon, Advanced Engineering Materials, **21,** 1801039 (2019).
10. A.P. Zhilyaev, T.G. Langdon, Progress in Materials Science, **53,** 893-979 (2008).
11. M.M. Castro, P.H.R. Pereira, A. Isaac, R.B. Figueiredo, T.G. Langdon, Journal of Alloys and Compounds, **780,** 422-427 (2019).

12. M.M. Castro, S. Sabbaghianrad, P.H.R. Pereira, E.M. Mazzer, A. Isaac, T.G. Langdon, R.B. Figueiredo, Journal of Alloys and Compounds, **804,** 421-426 (2019).

13. M.M. Castro, D.R. Lopes, R.B. Soares, D.M.M. dos Santos, E.H.M. Nunes, V.F.C. Lins, P.H.R. Pereira, A. Isaac, T.G. Langdon, R.B. Figueiredo, Materials, **12,** 2609 (2019).

14. R.B. Figueiredo, S. Sabbaghianrad, A. Giwa, J.R. Greer, T.G. Langdon, Acta Materialia, **122,** 322-331 (2017).

15. E.Y. Yoon, D.J. Lee, T.S. Kim, H.J. Chae, P. Jenei, J. Gubicza, T. Ungar, M. Janecek, J. Vratna, S. Lee, H.S. Kim, Journal of Materials Science, **47,** 7117-7123 (2012).

16. M.M. de Castro, A.P. Carvalho, P.H.R. Pereira, A.C. Isaac Neta, R.B. Figueiredo, T.G. Langdon, Materials Science Forum, **941,** 851-856 (2019).

17. J.-M. Dubois, Materials Science and Engineering: A, **294-296,** 4-9 (2000).

18. B.A. Silva Guedes de Lima, R. Medeiros Gomes, S.J. Guedes de Lima, D. Dragoe, M.-G. Barthes-Labrousse, R. Kouitat-Njiwa, J.-M. Dubois, Science and Technology of Advanced Materials, **17,** 71-79 (2016).

19. J.-M. Dubois, Chemical Society Reviews, **41,** 6760-6777 (2012).

20. M. Galano, F. Audebert, I.C. Stone, B. Cantor, Acta Materialia, **57,** 5107-5119 (2009).

21. W. Wolf, C. Bolfarini, C.S. Kiminami, W.J. Botta, Scripta Materialia, **173,** 21-25 (2019).

22. W. Wolf, L.C.R. Aliaga, D.N. Travessa, C.R.M. Afonso, C. Bolfarini, C.S. Kiminami, W.J. Botta, Materials Research, **19,** 74-79 (2016).

23. R.B. Figueiredo, S. Sabbaghianrad, T.G. Langdon, IOP Conference Series: Materials Science and Engineering, **194,** 012039 (2017).

24. R.B. Figueiredo, P.H.R. Pereira, T.G. Langdon, Advanced Engineering Materials, **0,** 1900565 10.1002/adem.201900565

25. R.B. Figueiredo, M. Kawasaki, T.G. Langdon, Acta Physica Polonica A, **122,** 425-429 (2012).

26. R.B. Figueiredo, M.T.P. Aguilar, P.R. Cetlin, T.G. Langdon, Metallurgical and Materials Transactions A: Physical Metallurgy and Materials Science, **42,** 3013-3021 (2011).

27. R.B. Figueiredo, T.G. Langdon, Materials Science and Engineering A, **528,** 4500-4506 (2011).

Chapter 7.

Magnesium-based bioactive composites processed at room temperature

Moara M. Castro [1], Debora R. Lopes [2], Renata B. Soares [2], Diogo M. dos Santos[1], Eduardo H.M. Nunes [1], Vanessa F.C. Lins [2], Pedro Henrique R. Pereira [1], Augusta Isaac [1], Terence G. Langdon [3], Roberto B. Figueiredo [1]

[1] Department of Metallurgical and Materials Engineering, Universidade Federal de Minas Gerais, Belo Horizonte 31270-901, Brazil

[2] Department of Chemical Engineering, Universidade Federal de Minas Gerais, Belo Horizonte 31270-901, Brazil

[3] Materials Research Group, Department of Mechanical Engineering, University of Southampton, Southampton SO17 1BJ, UK

Abstract: Hydroxyapatite and bioactive glass particles were added to pure magnesium and an AZ91 magnesium alloy and then consolidated into disc-shaped samples at room temperature using high-pressure torsion (HPT). The bioactive particles appeared well-dispersed in the metal matrix after multiple turns of HPT. Full consolidation was attained using pure magnesium but the centre of the AZ91 disc failed to fully consolidate even after 50 turns. The magnesium-hydroxyapatite composite displayed an ultimate tensile strength above 150 MPa but a loss of mechanical stability after immersion in Hank's solution. The composites produced with bioactive glass particles exhibited the formation of calcium phosphate after 2 hours of immersion in Hank's solution and there was rapid corrosion in these materials.

Keywords: Bioactive glass; Biodegradable material; Composites; High-pressure torsion; Hydroxyapatite; Magnesium

7.1. Introduction

Biodegradable metals provide an opportunity for fabricating temporary implants with high initial load-bearing capacities which degrade as the surrounding tissue regenerates. In principle, the degradation byproduct can be absorbed and excessive amounts expelled by the human body without the need for secondary surgery for removal. A recent review describes past and current clinical trials in this field [1] where orthopedic and cardiovascular applications are the main targets. Iron, magnesium and zinc display good biocompatibility and gradually degrade in physiological media. Iron exhibits the highest mechanical strength but the corrosion rate is too low whereas zinc exhibits a fast corrosion rate but poor mechanical properties. Magnesium has attracted significant attention for these applications despite the relatively low strength of the pure metal and the fast corrosion of its alloys. The maximum daily dosage intake of magnesium is high [2] and the elastic modulus is low where these are considered advantages for this material.

In addition to biocompatibility, a bone graft should exhibit mechanical integrity with the bone tissue. This means that the mechanical strength and fracture toughness should be high and the Young's modulus must be similar to that exhibited by bone [3]. Together with its biological characteristics of high biocompatibility and a non-toxic risk during biodegradation, the density (1.74 g/cm^3) and tensile strength (~135-285 MPa) of magnesium are similar to those of bone (1.8-2.0 g/cm^3 and ~35-283 MPa, respectively) [3]. In addition, magnesium displays a higher fracture toughness of ~15-40 MPa/m^2 compared with ~3-6 MPa/m^2 for bone. The similarity in density and elastic modulus to bone makes magnesium a promising candidate material for applications such as bone graft because these properties will lead to lower stresses at the implant-bone interfaces [4].

In order to improve the performance of magnesium-based materials, research has focused primarily on improving the mechanical strength and corrosion resistance. Alloying is an effective way for increasing the yield strength but usually this will compromise the corrosion. Alternatively, grain refinement provides an opportunity for improving the strength without changing the composition. Severe plastic deformation (SPD) techniques such as Equal-Channel Angular Pressing (ECAP) [5] and High-Pressure Torsion (HPT) [6] have been used to refine the grain structure of metallic materials and give grain sizes in the submicrometer or

nanometer range that are smaller than those produced using conventional thermo-mechanical processing techniques. The low ductility of magnesium generally precludes the use of ECAP processing at low temperatures and ECAP processing at high temperatures reduces the effectiveness of the grain refinement. By contrast, processing by HPT is associated with high hydrostatic compressive stresses that prevent the failure of brittle materials. This SPD technique has been used widely to process magnesium and its alloys to produce ultrafine grain sizes and increasing strength [7]. There is now experimental evidence that HPT processing enhances the corrosion resistance of pure magnesium [8,9] and also significantly improves the mechanical properties [10,11].

Magnesium matrix composites are also potential candidates for structural orthopedic implants where the second phase may improve the strength and/or improve the biological performance. Calcium phosphates such as hydroxyapatite (HA) are particularly interesting materials for orthopedic applications because HA can form strong chemical bonds with the bone tissue and it is one of the main components affecting the mechanical strength and providing stiffness to bone [3]. However, bone grafts made exclusively of HA may have only restricted applicability because of their high density (3.1 g/cm^3) and low fracture toughness (0.7 MPa/m^2). Accordingly, metal-matrix composites consisting of a biodegradable Mg-alloy matrix together with HA particles as a secondary phase are important materials for orthopedic implants because they provide an opportunity to match the biological performance of HA with the toughness of Mg.

There are many reports on the fabrication of magnesium-based composites with hydroxyapatite using not only commercial purity Mg [12-18] but also Mg alloys such as AZ91 [19,20]. The usual fabrication methods involve heating, such as sintering [12,16,17] or hot extrusion [15,18,19,21]. The addition of HA within the Mg matrix, combined with mechanical processing, provides both grain refinement and a gain in strength. Conversely, a common difficulty when the HA content is above ~10 wt.% is the development of an inhomogeneous distribution of HA [15,19,21] which compromises the corrosion resistance of the composite.

The use of HPT also permits a fabrication of metal matrix composites (MMCs) through the consolidation of particles [22-24]. This method provides an opportunity for producing MMCs without any heating but with ultrafine grains in the matrix. Recently it was shown that it is possible to produce a Mg-Al_2O_3 composite with a

good dispersion of the ceramic phase [25] and a Mg-Al composite with good ductility [26]. Thus, the present research was undertaken in order to make use of HPT in fabricating magnesium-based bioactive composites and also to provide an initial characterization of these materials.

7.2. Materials and Methods

The experiments were conducted using particles as starting materials. Commercial purity magnesium and AZ91 magnesium alloy particles were provided by RIMA (Bocaiúva, MG). Hydroxyapatite-$Ca_5(OH)(PO4)_3$ (HA) nanopowder (Sigma-Aldrich) was used as the reinforcement phase. 58S bioactive glass (BG) (60 mol% SiO_2, 36 mol% CaO, 4 mol% P_2O_5) was prepared by the sol-gel process. Tetraethyl orthosilicate (TEOS/Aldrich/98%), triethyl phosphate (TEP/Aldrich/≥ 99.8%) and calcium nitrate tetrahydrate ($Ca(NO_3)_2$•$4H_2O$/Vetec/≥ 98%) were used as precursors in these syntheses. The monoliths produced were then hand-milled and air-dried at 120 °C for 5 days before heat-treating in air at 700 °C for 6 hours. A detailed description of this procedure is given elsewhere [27]. Figure 7.1 shows secondary electron images (SEI) of the materials used.

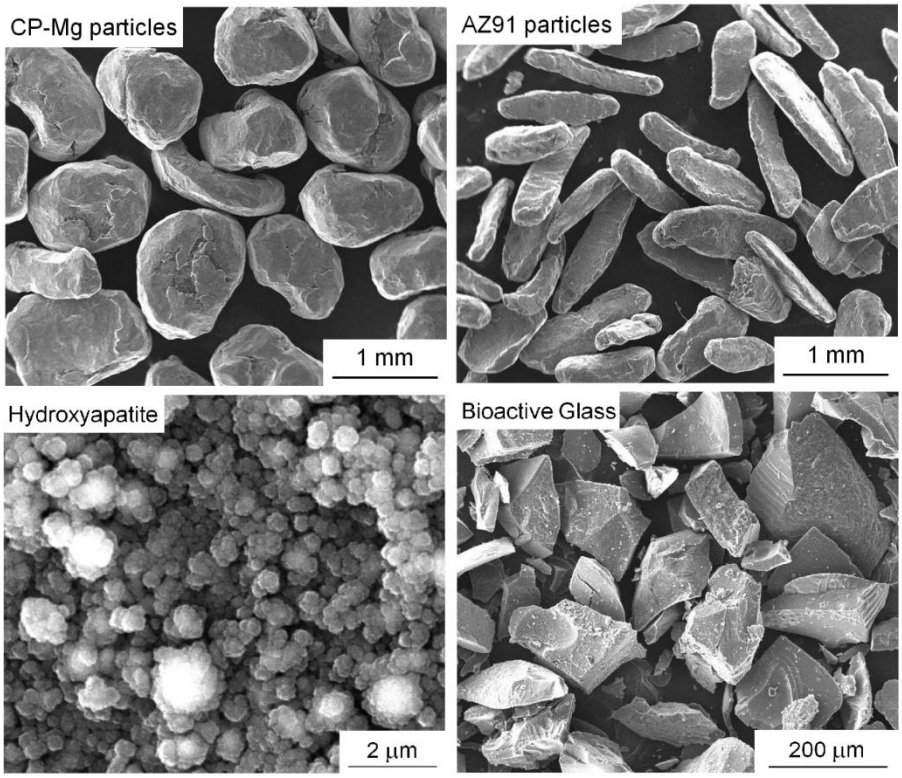

Figure 7.1. Particles used as starting materials.

The CP-Mg and AZ91 particles were mixed with 5 wt.% of a bioactive component (HA and BG) creating the blends Mg-5% HA, Mg-5% BG and AZ91-5% BG which were initially compacted at room temperature into 10 mm diameter discs using a hydraulic press. The compacted discs were subsequently consolidated at room temperature using a quasi-constrained HPT facility under a nominal pressure of 6 GPa. The Mg-5% BG was processed through 10 turns and the Mg-5% HA and AZ91-5% BG through 50 turns. After HPT processing, the samples were ground with abrasive paper, polished with diamond paste and a colloidal silica solution to obtain a mirror-like finish. Each polished sample was examined by scanning electron microscopy (SEM).

The mechanical properties were evaluated by Vickers hardness testing with a load of 50 gf and a dwell time of 10 s. Also, two miniature tensile specimens were cut from symmetrical positions in each Mg-5% HA disc using electro-discharge machining. As in an earlier investigation [28], the gauge sections of the specimens were located at distances of ~2 mm from the disc centres and the specimens had lengths and widths of ~1 mm and thicknesses of ~0.60 mm. Tensile tests were performed at room temperature at a constant cross-head displacement rate using an initial strain rate of 1.0×10^{-4} s^{-1}.

The corrosion behaviour was assessed by electrochemical impedance spectroscopy (EIS) in Hank's solution using a potentiostat (Autolab PGSTAT 100N with FRA32M impedance modulus) with 3 electrodes (Ag/AgCl as reference, platinum as counter electrode and the composite as the working electrode). The EIS test was performed at frequency range of 1 mHz to 10^4 Hz and amplitude of 0.01 V. The composition of Hank's solution is given in Table 1. The discs were ground using #4000 abrasive paper and then immersed in Hank's solution for at least 600 s before testing. After immersion, the samples were dried and the corroded surface was examined by SEM. In practice, the immersion times varied among samples since the composites with BG displayed faster corrosion than the HA-containing materials. The corrosion rate of the Mg-HA composite was determined by assessing the volume of H_2 formed during the soaking in Hank's solution. The electrochemical tests and immersion tests were conducted at room temperature and 37 °C, respectively.

The cytotoxicity of the Mg-5% HA composite was estimated using a 3-(4.5-dimethylthiazolyl-2)-2.5-diphenyltetrazolium bromide (MTT) test. Thus, 4 wells

were seeded with ~1.0 × 10^5 fibroblast cells, WI-26 VA4 (ATCC® CCL-95.1TM) cell lineage, in 500 µL of RPMI 1640 (Sigma-Aldrich) media supplemented with 10% fetal bovine serum (Gibco). The cells were maintained for 24 hours at 37 °C and 5% CO2 and then washed with 200 µL PBS 1X. Afterwards, 500 µL of media supplemented with 1% fetal bovine serum was added to each well. A sample of the Mg-5% HA composite was placed in one of the wells and kept for 24 hours. The cells in the 4 wells were then washed using PBS, a solution of 0.5 ng/mL of MTT was added and they were kept for a further 3 hours. The absorbance at 550 nm was measured using a SpectraMax M5E (Molecular Devices) spectrophotometer. The cells in the wells not in contact with the composite were considered the control group. The absorbance of the cells in contact with the composite was expressed as a fraction of the control group to evaluate the overall viability.

Table 7.1. Composition of Hank's solution.

Chemical compost	**Concentration ($g.L^{-1}$)**
NaCl	8
KCl	0.4
$MgSO_4.7H_2O$	0.06
$MgCl_2.6H_2O$	0.1
$CaCl_2$	0.14
$Na_2HPO_4.2H_2O$	0.06
KH_2PO_4	0.06
Glucose	0.1
$NaHCO_3$	0.35

7.3. Results

7.3.1. Consolidation

Observations using SEM showed good consolidation and the presence of well-dispersed particles in the Mg-HA composite. Figure 7.2 shows a representative image taken at the mid-radius position. A continuous magnesium matrix and second phase particles having sizes of tens to hundreds of microns is readily observed.

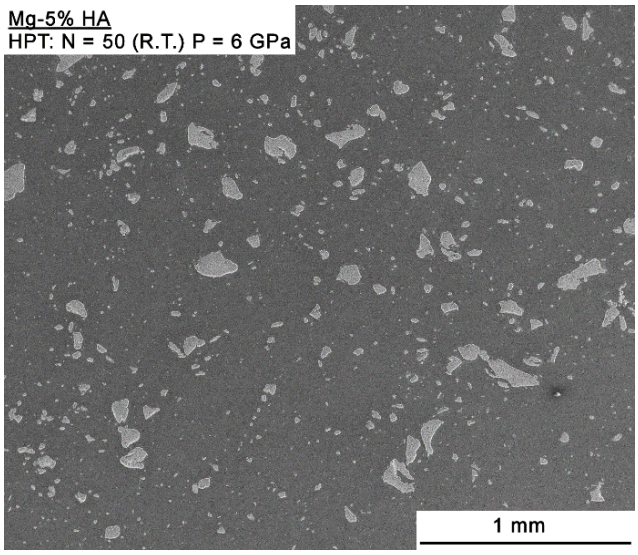

Figure 7.2. SEM backscattered electron image of the mid-radius area of the Mg-HA composite.

Figure 7.3 depicts EDS compositional maps of the Mg-HA composite where the distribution of Mg, Ca, P and O reveals a continuous Mg matrix while the second phase is rich in Ca, P and O.

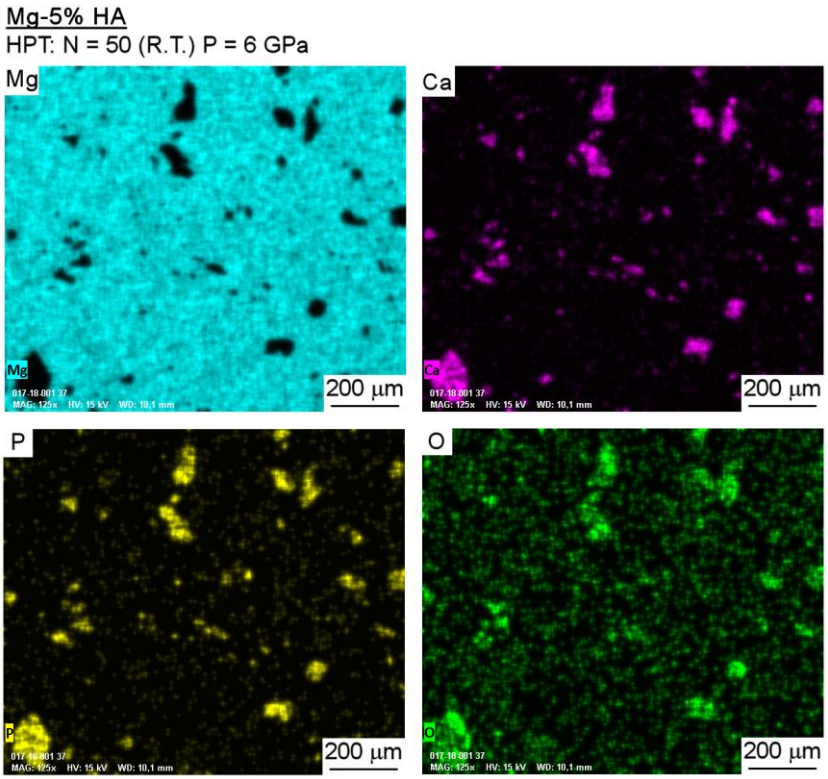

Figure 7.3. EDS composition maps taken at a selected area of the Mg-HA composite.

The Mg-BG composite displayed slightly different microstructures near and away from the centre of the disc-shaped sample. Thus, Fig. 7.4 shows SEM images demonstrating the presence of coarse second phase particles near the centre (left image) and much finer particles at the mid-radius position (right image). A few cracks are visible in the coarse second phase particles near the centre suggesting that HPT processing thereby promotes their fragmentation. This observation agrees with the presence of finer particles away from the centre where the amount of imposed torsional straining is significantly higher.

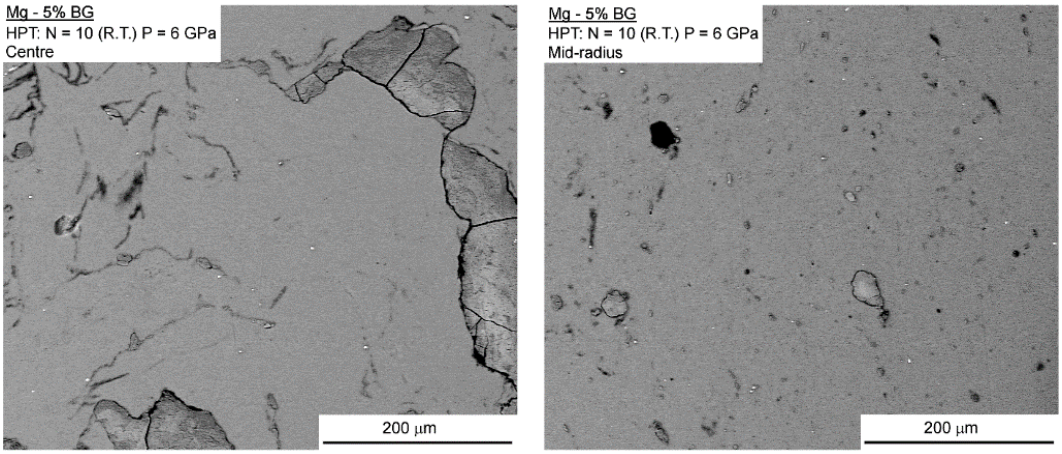

Figure 7.4. SEM backscattered electron images of areas near the centre (left) and at the mid-radius position (right) of the Mg-BG composite.

The AZ91-BG composite also exhibited different microstructures at and away from the disc centre. Figure 7.5 shows low magnification images, using backscattered electrons (BSE) and secondary electrons (SE), of a region near the centre. The BSE image on the left portrays the presence of coarse volumes with similar sizes to the initial AZ91 particles near the centre suggesting a lack of consolidation in this area. A continuous matrix was observed away from the centre indicating the achievement of full consolidation in this region. A higher magnification image of the boundary between the areas with or without consolidation is also shown. The SE image on the right depicts the distribution of the hard BG particles. As already noted for the Mg-BG composite, finer BG particles were observed away from the centre of the AZ91-BG composite.

Figure 7.6 presents the hardness distributions along randomly selected diameters for the samples obtained in these experiments. The CP-Mg-based composites display a homogeneous distribution of microhardness within the interval of ~75-80 Hv while the AZ91-based composite is harder with values in the range of ~115-

125 Hv. These latter values are similar to those recorded in a bulk AZ91 alloy subjected to 5 HPT turns [29] and this shows that the second phase was not effective in increasing the strength of the alloy. Nevertheless, there are some reports of lower hardness values for bulk pure magnesium processed by HPT as, for example, an average hardness of 45 Hv in as-cast magnesium processed from 1/8 to 16 HPT turns [30] and a hardness lower than 40 Hv for pure Mg processed to 10 turns [31]. Machining chips of CP-Mg consolidated using HPT displayed a hardness of ~48 Hv after 5 turns [25] but, by contrast, a Mg-Al_2O_3 composite consolidated by HPT exhibited a higher hardness (~65 Hv) than the bulk material near the edge of the sample after only 5 turns [25]. These various results show that the second phase is effective in increasing the hardness of pure magnesium and the higher values of hardness in the current experiments for the CP-Mg-based composites is therefore attributed to the presence of second phase particles and the large numbers of turns.

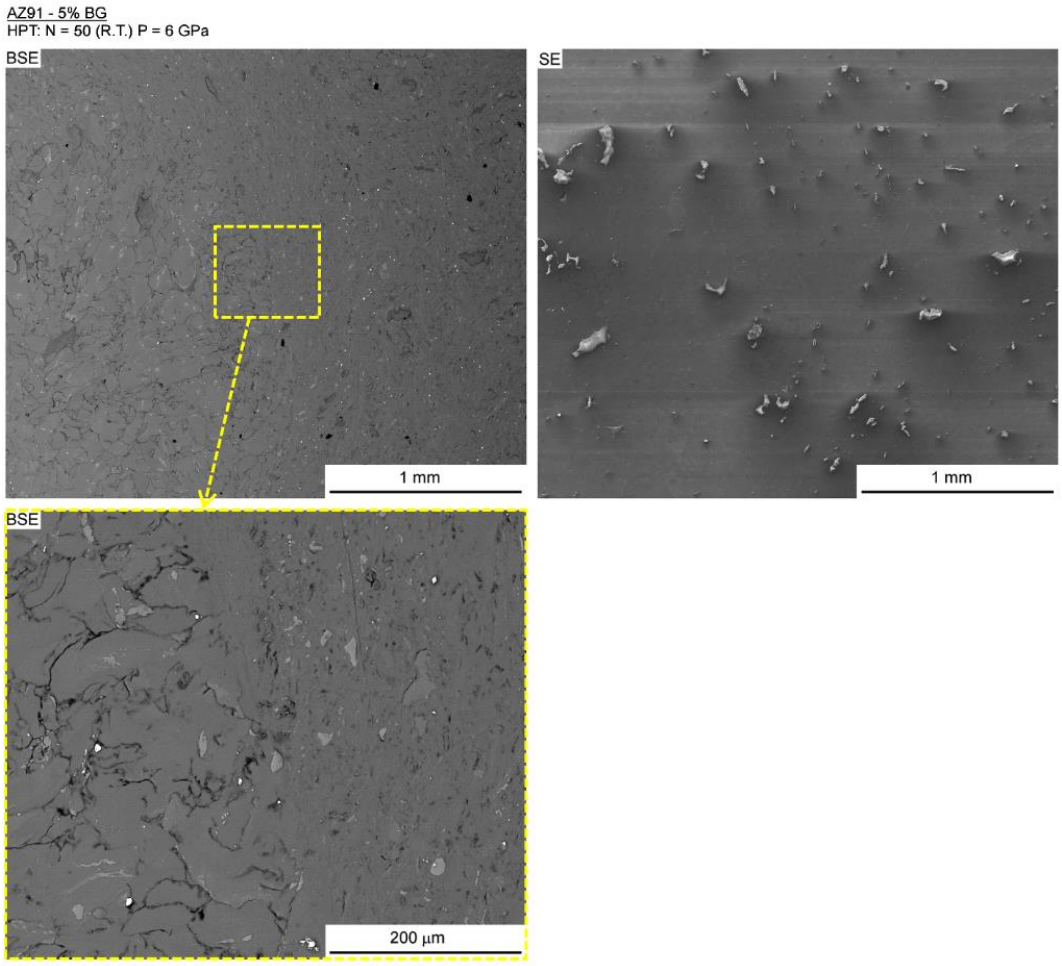

Figure 7.5. SEM images using backscattered electrons (left) and secondary electrons (right) of the AZ91-BG composite.

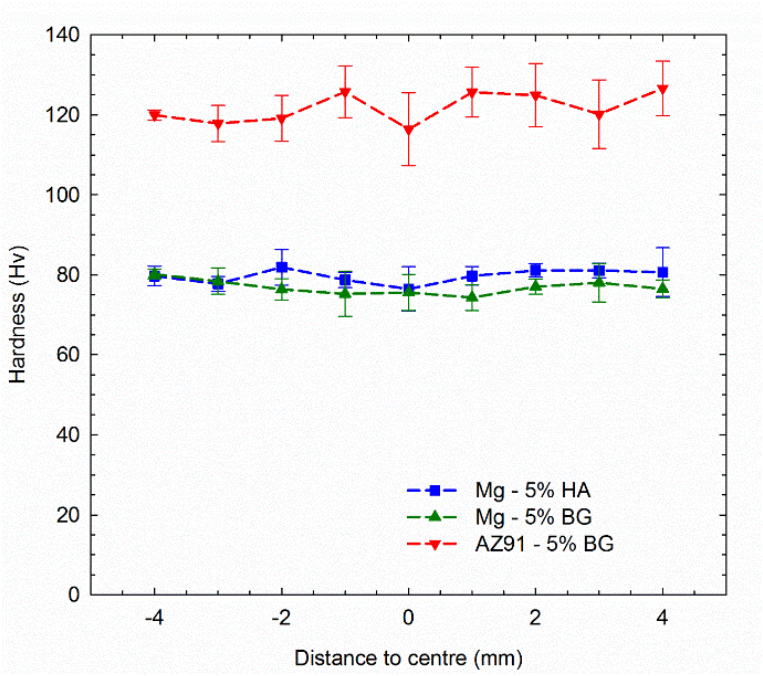

Figure 7.6. Microhardness distribution along the disc diameter in the different Mg composites.

7.3.2. Corrosion

The curves obtained by EIS for different composites are presented in Fig. 7.7 where the impedance arc is significantly larger for the Mg-HA composite when compared to the BG-containing composites. For convenience, the arcs for the Mg-BG and AZ91-BG composites are also shown in an insert at the upper right with a reduced scale. A curve obtained during testing of commercial purity Mg (CP-Mg) processed by HPT [32] is also shown in Fig. 7.7 for comparison purposes. Thus, it is apparent that the second phase reduces the corrosion resistance of Mg and this effect is more pronounced when using BG. In fact, the Mg-BG and AZ91-BG composites showed faster corrosion rates and the processed discs were completely corroded in less than 24 hours of immersion. It is worth noting also that the AZ91-BG alloy displays an arc smaller than the Mg-BG sample and this is attributed to the presence of precipitates in the AZ91 matrix.

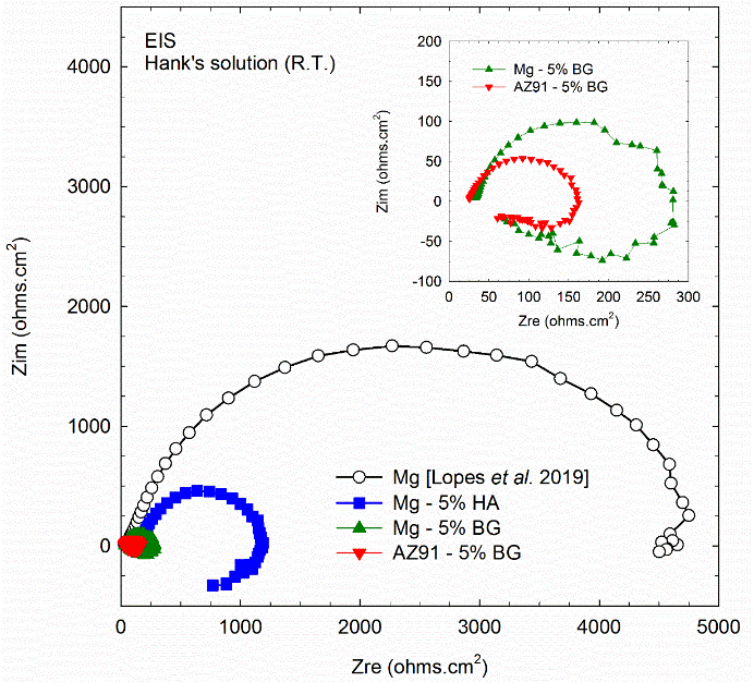

Figure 7.7. Electrochemical impedance spectroscopy tests in Hank's solution for the different composites. The value for bulk Mg processed by HPT [32] is also shown for comparison.

The surfaces of the Mg-BG and AZ91-BG composites were examined using SEM after 2 hours of immersion in Hank's solution. Figure 7.8 reveals that Mg-BG exhibits large areas of localized corrosion but it is apparent at lower magnification (left) that most of the surface undergoes no significant corrosion. However, at higher magnification (right) it is possible to distinguish many areas of localized corrosion throughout the magnesium matrix.

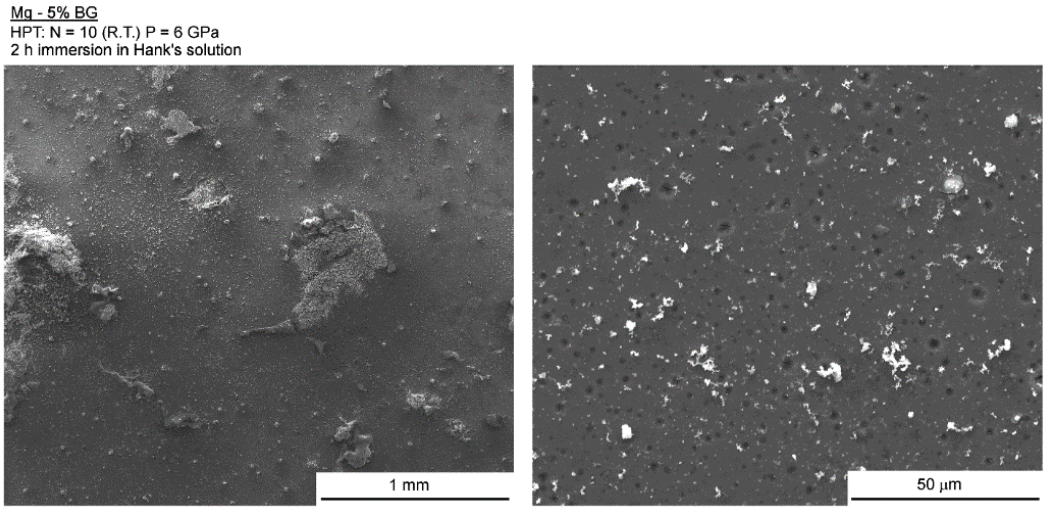

Figure 7.8. Low (left) and high (right) magnification images of the surface of the Mg-BG composite after 2 hours of immersion in Hank's solution.

EDS mapping was used to evaluate the composition around one of these areas and Fig. 7.9 displays the distribution of Mg, O, Ca, P and Si together with the secondary electron image. It is apparent that the volume of the corrosion product in this area is poor in Mg, rich in Ca, P and O and the distribution of Si is homogeneous but significantly lower than for Ca and P. This suggests the formation of calcium phosphate in the corrosion product.

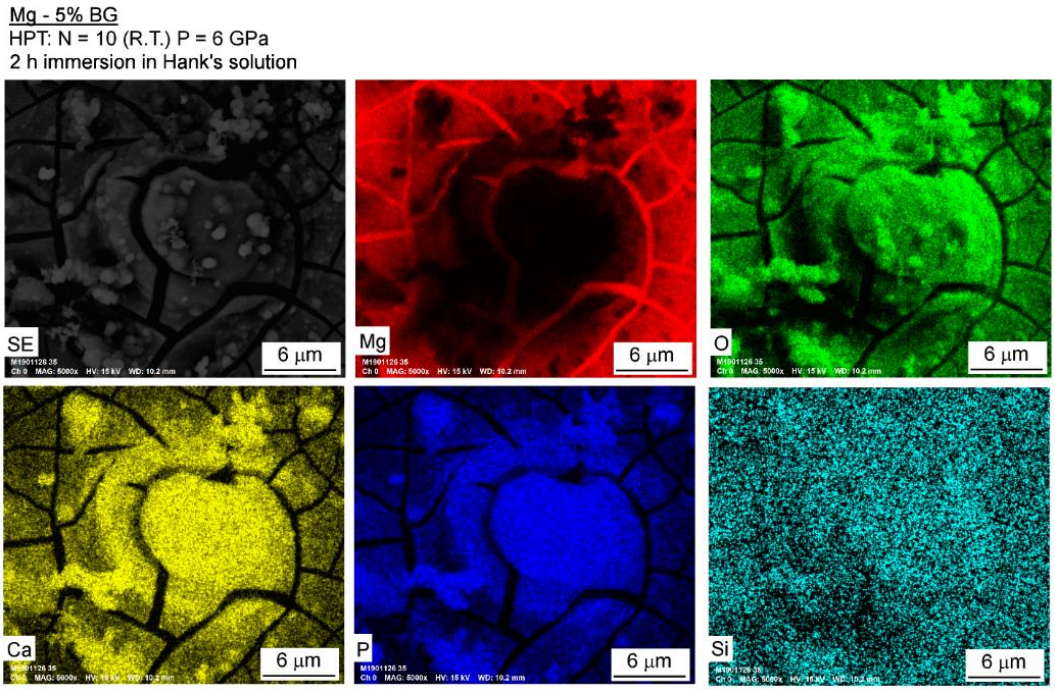

Figure 7.9. EDS mapping of an area of localized corrosion in the Mg-BG composite after 2 hours of immersion in Hank's solution.

The AZ91-BG composite showed signs of more severe corrosion throughout the sample surface and Fig. 7.10 portrays the appearance of the surface after 2 hours of immersion in Hank's solution. For this composite the corrosion product is thicker than observed in the Mg-BG composite and the whole surface of the sample is corroded.

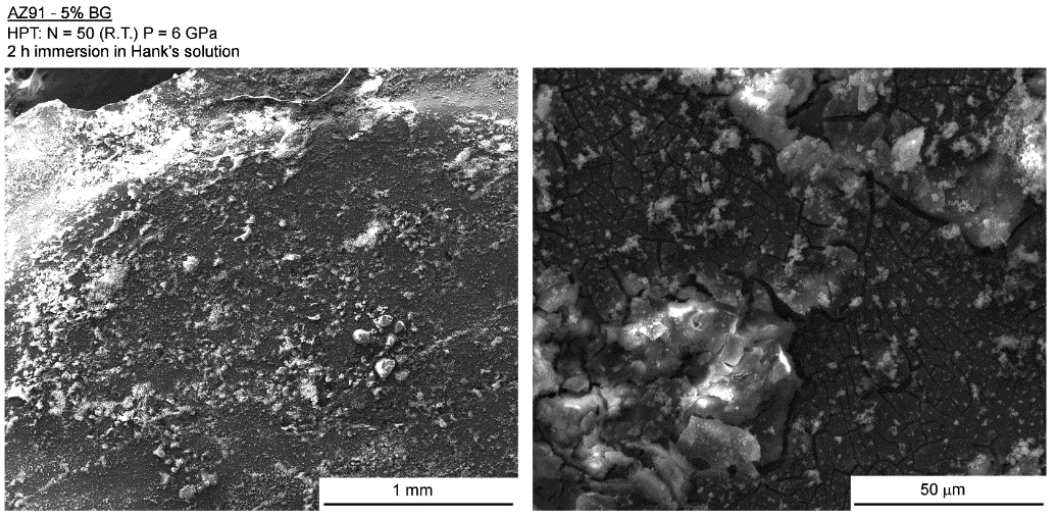

Figure 7.10. Low (left) and high (right) magnification images of the surface of the AZ91-BG composite after 2 hours of immersion in Hank's solution.

Figure 7.11 depicts the surface of the Mg-HA composite after 6 hours of immersion in Hank's solution where it is apparent that some areas undergo localized corrosion. Although the immersion period was longer in the Mg-HA composite compared to the Mg-BG composites, it is readily apparent that the process of corrosion is slower in the former and the areas of localized corrosion do not effectively propagate.

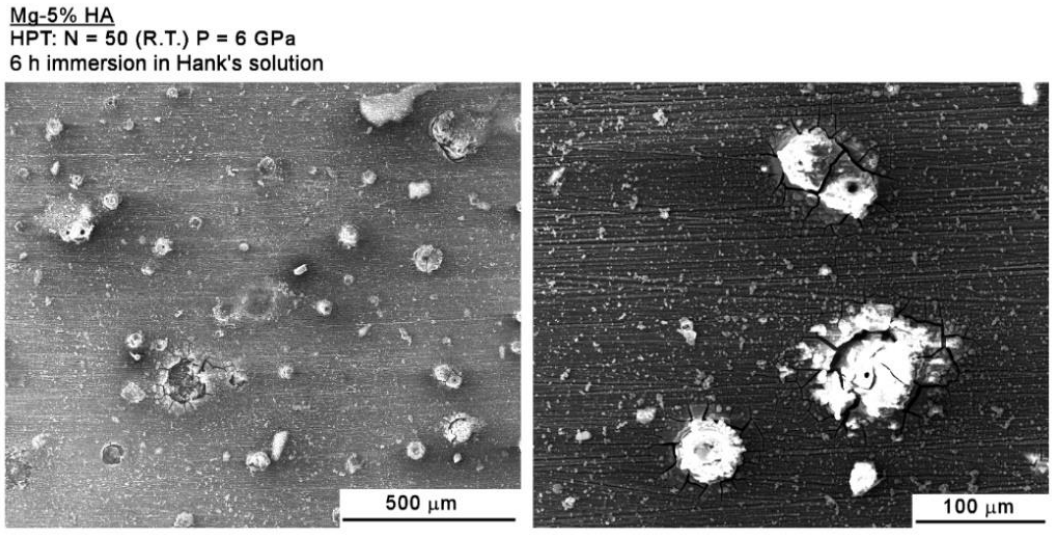

Figure 7.11. Low (left) and high (right) magnification images of the surface of the Mg-HA composite after 6 hours of immersion in Hank's solution.

7.3.3. Mg-Hydroxyapatite composite

The Mg-BG and the AZ91-BG samples failed to withstand 24 hours of immersion in Hank's solution at 37 °C. Nevertheless, the Mg-HA composite displayed a decreasing rate of corrosion with immersion time and further tests were therefore conducted with this material. Figure 7.12 shows the hydrogen evolution rate and thus a fast corrosion rate was observed in the initial testing stage. However, the corrosion rate decreased and ultimately became undetectable after about 15 hours of immersion. This suggests the formation of a protective layer of a corrosion product.

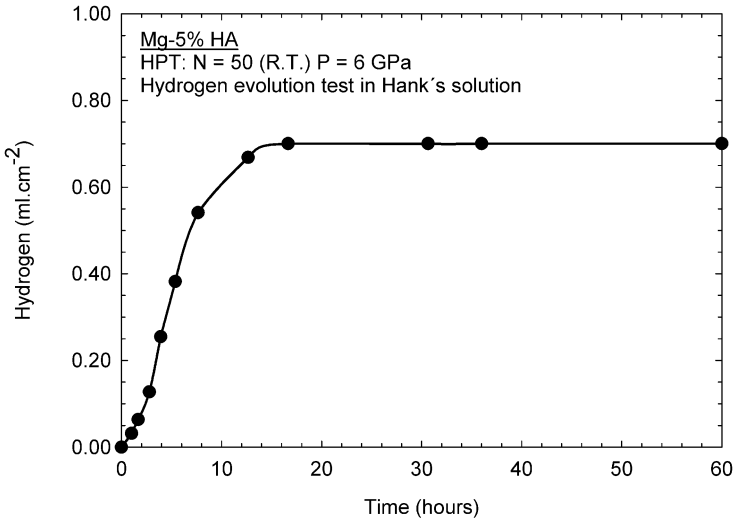

Figure 7.12. Hydrogen evolution as a function of time for the Mg-HA composite immersed in Hank's solution

The effectiveness of the consolidation of Mg particles in the Mg-HA composite was further assessed using miniature tensile testing and Fig. 7.13 shows an engineering stress vs. engineering strain curve obtained for the Mg-5% HA composite processed through 50 turns of HPT and then pulled to failure at room temperature. Thus, the composite displays an ultimate stress over 150 MPa which is significantly higher than observed in CP-Mg processed by HPT and tested using a similar strain rate [10,11]. The occurrence of this enhanced strength is consistent with the enhanced hardness compared to bulk magnesium and it is attributed to the presence of second phase particles. However, the ductility is significantly reduced compared to bulk magnesium [10,11].

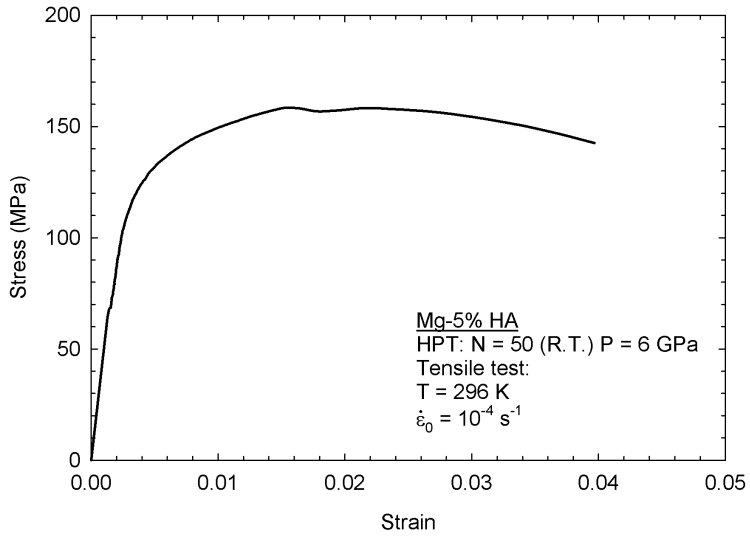

Figure 7.13. Stress vs strain curve for the Mg-HA composite.

The viability of the Mg-HA composite was evaluated using a MTT test. The values of the absorbance measured in the control groups (with no contact with any sample) and the group of cells in contact with the composite for 24 hours are presented in Table 7.2. Thus, the viability of the composite is high which shows that it is not toxic despite the fast initial corrosion. This is in agreement with an earlier report showing that HPT processing has no effect on the in vitro biocompatibility of pure magnesium and magnesium alloys [32].

Table 7.2. Citotoxicity of the Mg-5% HA composite evaluated by MTT test.

	Absorbance	Average	Viability
Control Group	2.8065	2.817	100%
	2.9065		
	2.7375		
Mg-5% HA	2.781	2.781	99%

7.4. Discussion

7.4.1. The effectiveness of the consolidation

The consolidation of metallic particles through HPT processing appears to be straight-forward in principle. Thus, the imposed compressive stress is many times higher than the flow stress of the base metal and this should induce plastic

deformation throughout the sample. The torsional strain is sufficiently high to promote an increase in contact area between the particles and this will lead to self-welding. This general effect was reported in the very early experiments of Bridgman [33] where it was claimed that finely divided powder emerges as a homogeneous disc after shearing. In fact, there are many reports of the consolidation of metallic particles by HPT [23,34-41] and initial observations of the processed discs suggest a full consolidation. Earlier reports described good consolidation of pure magnesium machining chips [25,42] after only 5 turns of HPT. Nevertheless, it was reported that the magnesium alloy AZ91 does not display full consolidation after similar processing [42]. The present results show that, even after 50 turns of HPT under a nominal pressure of 6 GPa, the boundaries between the initial coarse metallic particles remain visible at the centre of the AZ91-BG composite and a full consolidation was only observed from the mid-radius to the outer edge of the disc where the imposed torsional strains are significantly higher. The explanation for this lack of welding between particles is attributed to sliding between the particles which is probably aided by the presence of finely-dispersed bioactive glass particles in the present experiments. Also, it is known that strain localization may take place during the HPT processing of magnesium alloys [43,44] and this may lead to significantly lower deformation in large volumes of the disc which will effectively compromise the welding of the particles.

Despite the lack of full consolidation in the AZ91-based composite, pure magnesium-based composites display a homogeneous metallic matrix throughout the discs which suggests full consolidation. The effectiveness of consolidation was further assessed in the Mg-HA composite by tensile testing. Thus, areas with a lack of bonding should act as internal cracks that will then compromise the tensile resistance of the composite and yet the ultimate stress of the composite is higher than observed in bulk pure magnesium [10,11] which also supports the assumption of a full consolidation. It is worth noting that hardness and compression testing are not as effective as tensile testing in evaluating the soundness of the metallic matrix since internal defects propagate under tensile stresses but these defects can effectively withstand compressive loading. Although there are reports of the fabrication of magnesium-hydroxyapatite composites [12,15-19], tensile testing was seldom conducted and the ultimate stress observed in the present experiments is comparable to that observed in composites produced through hot-extrusion [14,15]. It is concluded, therefore, that HPT processing is effective in producing sound magnesium-based composites without the need to heat the

composite components. This approach therefore provides the opportunity to use temperature-sensitive materials to produce magnesium-based composites with a drug delivery ability.

7.4.2. Performance in Hank's solution

The EIS tests revealed small impedance arcs for the BG composites which is consistent with the fast corrosion observed in these materials. However, the Mg-HA composite displayed an impedance arc that was larger than observed in conventional AZ31 and ZK60 magnesium alloys [32] and this shows that the Mg-HA composite exhibits a considerable corrosion resistance. The hydrogen evolution test showed that the initially high corrosion rate gradually decreases until it reaches a very low value. Although this test is not effective for evaluating low corrosion rates, it shows clearly there is a trend of decreasing degradation rate and this is supported by the observation that a thin disc (~0.5 mm in thickness) withstood 60 hours of immersion in Hank's solution without developing a hole or any pronounced corrosion. It seems important in future experiments to further investigate the corrosion behaviour of this composite.

Although the Mg-BG and AZ91-BG composites displayed fast corrosion, there is evidence for the formation of calcium phosphate on the surface of the AZ91-BG composite. Thus, bioactive glass promotes the nucleation and growth of calcium phosphates in physiological media and this enhances the integration with bone. This bioactivity of BG is also observed in the magnesium-based composite but further research will be needed in order to enhance the corrosion resistance of this composite and to more fully establish the potential for producing bioactive and biodegradable composites. The poor corrosion resistance displayed by BG-containing composites may be related to the large particle size of BG which was above 200 μm. It appears that the BG exhibited breakage during the HPT processing with no filling of the voids and cracks by the metallic matrix (Figs 7.4 and 7.5). It was already reported that these defects can display a negative influence on the corrosion resistance of magnesium in physiological media [45]. Thus, in practice the particle size of BG could be decreased by, for example, either ball-milling or the use of a different sol-gel route [46].

7.5. Summary and Conclusions

1- Hydroxyapatite and bioactive glass particles were mixed with pure magnesium and particles of a magnesium AZ91 alloy and consolidated into a bulk disc at room temperature using HPT. The integrity of the composites was assessed using SEM examination and tensile testing. EIS and observations of the sample surfaces after immersion in Hank's solution were used to evaluate the corrosion behaviour.

2- Sound composites were produced with a continuous pure magnesium matrix and well-dispersed hydroxyapatite or bioactive glass particles. The AZ91 particles failed to consolidate well in the centre of the disc.

3- The composites with bioactive glass exhibited small impedance arcs and fast corrosion. Calcium phosphate was observed on the surface of a sample after only 2 hours of immersion in Hank's solution.

4- The composite with hydroxyapatite displayed a high tensile strength of ~160 MPa and a decreasing rate of corrosion.

7.6. Author contributions

M.M.C. contributed to sample preparation, microstructure characterization, carried out hardness and tensile tests, and prepared the first draft of the manuscript.

7.7. Acknowledgments:

The authors acknowledge the Centre of Microscopy at the Universidade Federal de Minas Gerais (http://www.microscopia.ufmg.br) for providing equipment and technical support for experiments involving electron microscopy. This research was funded by CNPq, grants numbers 306291/2018-5 and 400407/2016-7, FAPEMIG, grant number APQ-00580-15 and Serrapilheira Institute, grant number Serra-1709-17750. RBS received a research fellowship from CAPES.

7.8. References

1. Han, H.-S.; Loffredo, S.; Jun, I.; Edwards, J.; Kim, Y.-C.; Seok, H.-K.; Witte, F.; Mantovani, D.; Glyn-Jones, S. Current status and outlook on the clinical

translation of biodegradable metals. Materials Today 2019, 23, 57-71, doi:https://doi.org/10.1016/j.mattod.2018.05.018.

2. Kirkland, N.T.; Staiger, M.P.; Nisbet, D.; Davies, C.H.J.; Birbilis, N. Performance-driven design of Biocompatible Mg alloys. JOM 2011, 63, 28-34, doi:10.1007/s11837-011-0089-z.

3. Kuśnierczyk, K.; Basista, M. Recent advances in research on magnesium alloys and magnesium–calcium phosphate composites as biodegradable implant materials. Journal of Biomaterials Applications 2016, 31, 878-900, doi:10.1177/0885328216657271.

4. Brar, H.S.; Platt, M.O.; Sarntinoranont, M.; Martin, P.I.; Manuel, M.V. Magnesium as a biodegradable and bioabsorbable material for medical implants. JOM 2009, 61, 31-34, doi:10.1007/s11837-009-0129-0.

5. Valiev, R.Z.; Langdon, T.G. Principles of equal-channel angular pressing as a processing toold for grain refinement. Progress in Materials Science 2006, 51, 881-981.

6. Zhilyaev, A.P.; Langdon, T.G. Using high-pressure torsion for metal processing: Fundamentals and applications Progress in Materials Science 2008, 53, 893-979.

7. Figueiredo, R.B.; Langdon, T.G. Processing Magnesium and Its Alloys by High-Pressure Torsion: An Overview. Advanced Engineering Materials 2019, 21, 1801039, doi:doi:10.1002/adem.201801039.

8. Silva, C.L.P.; Oliveira, A.C.; Costa, C.G.F.; Figueiredo, R.B.; de Fátima Leite, M.; Pereira, M.M.; Lins, V.F.C.; Langdon, T.G. Effect of severe plastic deformation on the biocompatibility and corrosion rate of pure magnesium. Journal of Materials Science 2017, 52, 5992-6003, doi:10.1007/s10853-017-0835-x.

9. Silva, C.L.P.; Soares, R.B.; Pereira, P.H.R.; Figueiredo, R.B.; Lins, V.F.C.; Langdon, T.G. The Effect of High-Pressure Torsion on Microstructure, Hardness and Corrosion Behavior for Pure Magnesium and Different Magnesium Alloys. Advanced Engineering Materials 2019, 21, 1801081, doi:10.1002/adem.201801081.

10. Figueiredo, R.B.; Sabbaghianrad, S.; Giwa, A.; Greer, J.R.; Langdon, T.G. Evidence for exceptional low temperature ductility in polycrystalline magnesium processed by severe plastic deformation. Acta Materialia 2017, 122, 322-331, doi:10.1016/j.actamat.2016.09.054.

11. Figueiredo, R.B.; Sabbaghianrad, S.; Langdon, T.G. The effect of high-pressure torsion on the microstructure and properties of magnesium. IOP Conference Series: Materials Science and Engineering 2017, 194, 012039.

12. Ratna Sunil, B.; Ganapathy, C.; Sampath Kumar, T.S.; Chakkingal, U. Processing and mechanical behavior of lamellar structured degradable magnesium–hydroxyapatite implants. Journal of the Mechanical Behavior of Biomedical Materials 2014, 40, 178-189, doi:https://doi.org/10.1016/j.jmbbm.2014.08.016.

13. Mensah-Darkwa, K.; Gupta, R.K.; Kumar, D. Mechanical and Corrosion Properties of Magnesium–Hydroxyapatite (Mg–HA) Composite Thin Films. Journal of Materials Science & Technology 2013, 29, 788-794, doi:https://doi.org/10.1016/j.jmst.2013.04.019.

14. Kumar Khanra, A.; Jung, H.C.; Hoon Yu, S.; Sun Hong, K.; Shin, K.S. Microstructure and mechanical properties of Mg-HAP composites. Bulletin of Materials Science 2010, 33, 43-47, doi:10.1007/s12034-010-0006-z.

15. Gu, X.; Zhou, W.; Zheng, Y.; Dong, L.; Xi, Y.; Chai, D. Microstructure, mechanical property, bio-corrosion and cytotoxicity evaluations of Mg/HA composites. Materials Science and Engineering: C 2010, 30, 827-832, doi:https://doi.org/10.1016/j.msec.2010.03.016.

16. Khalil, K.A.; Almajid, A.A. Effect of high-frequency induction heat sintering conditions on the microstructure and mechanical properties of nanostructured magnesium/hydroxyapatite nanocomposites. Materials & Design 2012, 36, 58-68, doi:10.1016/j.matdes.2011.11.008.

17. Viswanathan, R.; Rameshbabu, N.; Kennedy, S.; Sreekanth, D.; Venkateswarlu, K.; Sandhya Rani, M.; Muthupandi, V. Plasma Electrolytic Oxidation and Characterization of Spark Plasma Sintered Magnesium/Hydroxyapatite Composites. Materials Science Forum 2013, 765, 827-831, doi:10.4028/www.scientific.net/MSF.765.827.

18. Campo, R.d.; Savoini, B.; Muñoz, A.; Monge, M.A.; Garcés, G. Mechanical properties and corrosion behavior of Mg–HAP composites. Journal of the Mechanical Behavior of Biomedical Materials 2014, 39, 238-246, doi:https://doi.org/10.1016/j.jmbbm.2014.07.014.

19. Witte, F.; Feyerabend, F.; Maier, P.; Fischer, J.; Störmer, M.; Blawert, C.; Dietzel, W.; Hort, N. Biodegradable magnesium–hydroxyapatite metal matrix composites. Biomaterials 2007, 28, 2163-2174, doi:https://doi.org/10.1016/j.biomaterials.2006.12.027.

20. Chen, B.; Yin, K.-Y.; Lu, T.-F.; Sun, B.-Y.; Dong, Q.; Zheng, J.-X.; Lu, C.; Li, Z.-C. AZ91 Magnesium Alloy/Porous Hydroxyapatite Composite for Potential Application in Bone Repair. Journal of Materials Science & Technology 2016, 32, 858-864, doi:https://doi.org/10.1016/j.jmst.2016.06.010.

21. Kumar Khanra, A.; Jung, H.C.; Hoon Yu, S.; Sun Hong, K.; Shin, K.S. Microstructure and mechanical properties of Mg-HAP composites; 2010; Vol. 33, pp. 43-47.

22. Ashida, M.; Horita, Z.; Kita, T.; Kato, A. Production of Al/Al_2O_3 Nanocomposites through Consolidation by High-Pressure Torsion. Materials Transactions 2012, 53, 13-16, doi:10.2320/matertrans.MD201128.

23. Cubero-Sesin, J.M.; Horita, Z. Powder consolidation of Al–10wt% Fe alloy by High-Pressure Torsion. Materials Science and Engineering: A 2012, 558, 462-471, doi:https://doi.org/10.1016/j.msea.2012.08.029.

24. Stolyarov, V.V.; Zhu, Y.T.; Lowe, T.C.; Islamgaliev, R.K.; Valiev, R.Z. Processing nanocrystalline Ti and its nanocomposites from micrometer-sized Ti powder using high pressure torsion. Materials Science and Engineering: A 2000, 282, 78-85, doi:https://doi.org/10.1016/S0921-5093(99)00764-9.

25. Castro, M.M.; Pereira, P.H.R.; Isaac, A.; Figueiredo, R.B.; Langdon, T.G. Development of a magnesium-alumina composite through cold consolidation of machining chips by high-pressure torsion. Journal of Alloys and Compounds 2019, 780, 422-427, doi:https://doi.org/10.1016/j.jallcom.2018.11.357.

26. Castro, M.M.; Sabbaghianrad, S.; Pereira, P.H.R.; Mazzer, E.M.; Isaac, A.; Langdon, T.G.; Figueiredo, R.B. A magnesium-aluminium composite produced by high-pressure torsion. Journal of Alloys and Compounds 2019, 804, 421-426, doi:https://doi.org/10.1016/j.jallcom.2019.07.007.

27. dos Santos, D.M.M.; de Carvalho, S.M.; Pereira, M.M.; Houmard, M.; Nunes, E.H.M. Freeze-cast composite scaffolds prepared from sol-gel derived 58S bioactive glass and polycaprolactone. Ceramics International 2019, 45, 9891-9900, doi:https://doi.org/10.1016/j.ceramint.2019.02.030.

28. Loucif, A.; Figueiredo, R.B.; Kawasaki, M.; Baudin, T.; Brisset, F.; Chemam, R.; Langdon, T.G. Effect of aging on microstructural development in an Al-Mg-Si alloy processed by high-pressure torsion. Journal of Materials Science 2012, 47, 7815-7820, doi:10.1007/s10853-012-6400-8.

29. Al-Zubaydi, A.; Figueiredo, R.B.; Huang, Y.; Langdon, T.G. Structural and hardness inhomogeneities in Mg–Al–Zn alloys processed by high-pressure torsion. Journal of Materials Science 2013, 48,4661-4670, doi:10.1007/s10853-013-7176-1.

30. Qiao, X.G.; Zhao, Y.W.; Gan, W.M.; Chen, Y.; Zheng, M.Y.; Wu, K.; Gao, N.; Starink, M.J. Hardening mechanism of commercially pure Mg processed by high pressure torsion at room temperature. Materials Science and Engineering: A 2014, 619, 95-106, doi:https://doi.org/10.1016/j.msea.2014.09.068.

31. Edalati, K.; Yamamoto, A.; Horita, Z.; Ishihara, T. High-pressure torsion of pure magnesium: Evolution of mechanical properties, microstructures and hydrogen storage capacity with equivalent strain. Scripta Materialia 2011, 64, 880-883, doi:https://doi.org/10.1016/j.scriptamat.2011.01.023.

32. Lopes, D.; Silva, C.L.P.; Soares, R.B.; Pereira, P.H.R.; Oliveira, A.C.; Figueiredo, R.B.; Langdon, T.G.; Lins, V.F.C. Cytotoxicity and corrosion behaviour of magnesium and magnesium alloys in Hank´s solution after processing by high-pressure torsion. Advanced Engineering Materials 2019, In press.

33. Bridgman, P.W. Shearing Phenomena at High Pressure of Possible Importance for Geology. The Journal of Geology 1936, 44, 653-669, doi:10.1086/624468.

34. Asgharzadeh, H.; Faraghi, H.; Kim, H.S. Fabrication of Fullerene-Reinforced Aluminum Matrix Nanocomposites. Acta Metallurgica Sinica (English Letters) 2017, 30, 973-982, doi:10.1007/s40195-017-0629-9.

35. Asgharzadeh, H.; Joo, S.-H.; Lee, J.-K.; Kim, H.S. Consolidation of Cu-based amorphous alloy powders by high-pressure torsion. Journal of Materials Science 2015, 50, 3164-3174, doi:10.1007/s10853-015-8877-4.

36. Edalati, K.; Ashida, M.; Horita, Z.; Matsui, T.; Kato, H. Wear resistance and tribological features of pure aluminum and Al–Al_2O_3 composites consolidated by high-pressure torsion. Wear 2014, 310, 83-89, doi:https://doi.org/10.1016/j.wear.2013.12.022.

37. Zhilyaev, A.P.; Gimazov, A.A.; Raab, G.I.; Langdon, T.G. Using high-pressure torsion for the cold-consolidation of copper chips produced by machining. Materials Science and Engineering: A 2008, 486, 123-126, doi:https://doi.org/10.1016/j.msea.2007.08.070.

38. Botta, W.J.; Fogagnolo, J.B.; Rodrigues, C.A.D.; Kiminami, C.S.; Bolfarini, C.; Yavari, A.R. Consolidation of partially amorphous aluminium-alloy powders by severe plastic deformation. Materials Science and Engineering: A 2004, 375-377, 936-941, doi:https://doi.org/10.1016/j.msea.2003.10.072.

39. Yavari, A.R.; Botta, W.J.; Rodrigues, C.A.D.; Cardoso, C.; Valiev, R.Z. Nanostructured bulk Al90Fe5Nd5 prepared by cold consolidation of gas atomized powder using severe plastic deformation. Scripta Materialia 2002, 46, 711-716, doi:https://doi.org/10.1016/S1359-6462(02)00057-X.

40. Alexandrov, I.V.; Zhu, Y.T.; Lowe, T.C.; Islamgaliev, R.K.; Valiev, R.Z. Consolidation of nanometer sized powders using severe plastic torsional straining. Nanostructured Materials 1998, 10, 45-54, doi:https://doi.org/10.1016/S0965-9773(98)00026-9.

41. Alexandrov, I.V.; Islamgaliev, R.K.; Valiev, R.Z.; Zhu, Y.T.; Lowe, T.C. Microstructures and properties of nanocomposites obtained through SPTS consolidation of powders. Metallurgical and Materials Transactions A 1998, 29, 2253-2260, doi:10.1007/s11661-998-0103-4.

42. de Castro, M.M.; Carvalho, A.P.; Pereira, P.H.R.; Isaac Neta, A.C.; Figueiredo, R.B.; Langdon, T.G. Consolidation of Magnesium and Magnesium Alloy Machine Chips Using High-Pressure Torsion. Materials Science Forum 2019, 941, 851-856, doi:10.4028/www.scientific.net/MSF.941.851.

43. Figueiredo, R.B.; Aguilar, M.T.P.; Cetlin, P.R.; Langdon, T.G. Deformation heterogeneity on the cross-sectional planes of a magnesium alloy processed by high-pressure torsion. Metallurgical and Materials Transactions A: Physical Metallurgy and Materials Science 2011, 42, 3013-3021, doi:10.1007/s11661-011-0609-z.

44. Figueiredo, R.B.; Langdon, T.G. Development of structural heterogeneities in a magnesium alloy processed by high-pressure torsion. Materials Science and Engineering A 2011, 528, 4500-4506, doi:10.1016/j.msea.2011.02.048.

45. Huan, Z.G.; Leeflang, M.A.; Zhou, J.; Duszczyk, J. ZK30-bioactive glass composites for orthopedic applications: A comparative study on fabrication method and characteristics. Materials Science and Engineering: B 2011, 176, 1644-1652, doi:https://doi.org/10.1016/j.mseb.2011.07.022.

46. Lins, C.E.C.; Oliveira, A.A.R.; Gonzalez, I.; Macedo, W.A.A.; Pereira, M.M. Structural analysis of fluorine-containing bioactive glass nanoparticles synthesized by sol–gel route assisted by ultrasound energy. Journal of Biomedical Materials Research Part B: Applied Biomaterials 2018, 106, 360-366, doi:10.1002/jbm.b.33846.

Chapter 8.

Mechanical mixing of Mg and Zn using high-pressure torsion

Moara M. Castro[1], Luciano A. Montoro[2], Augusta Isaac[1], Megumi Kawasaki[3], Roberto B. Figueiredo[1]

[1] Department of Metallurgical and Materials Engineering, Universidade Federal de Minas Gerais, Belo Horizonte, MG 31270-901, Brazil

[2] Department of Chemistry, Universidade Federal de Minas Gerais, Belo Horizonte, MG 31270-901, Brazil

[3] School of Mechanical, Industrial and Manufacturing Engineering, Oregon State University, Corvallis, OR 97331 U.S.A.

Abstract: High-pressure torsion (HPT) processing has proved to be a powerful tool to consolidate metallic particles and fabricate nanostructured metal-matrix composites with a wide range of compositions. In this study, HPT was used to fabricate different Mg-Zn composites at room temperature, and the evolution of microstructure and mechanical properties were analysed by x-ray diffraction, scanning and transmission electron microscopy, dynamic hardness and Vickers microhardness tests. The results show that ultrafine-grained microstructures were achieved in all composites compositions. Smaller grain sizes are observed in Mg-rich phases near areas with significant segregations of Zn. The Mg-rich phase appears to retain less deformation than the Zn-rich phase. Bending and vortex phenomena usually reported in microscale for materials mixed by HPT, are observed in nanoscale in this work. There is evidence of the $MgZn_2$ intermetallic phase with a morphology that varies with composition. Higher levels of deformation imposed by HPT leads to an increase in hardening and a decrease in strain-rate sensitivity which are attributed to the tendency to form intermetallics and Zn segregations that prevent grain boundary sliding. Moreover, a model is proposed to explain the mixing of phases in microscale and its relation to the evolution of mechanical properties.

Keywords: High-pressure torsion; Metal matrix composites; Magnesium; Zinc; Grain boundary segregation

8.1. Introduction

Severe plastic deformation (SPD) is one of the widespread methods used for producing ultrafine-grained structure of metal and alloys which usually results in exceptional mechanical strengthening. SPD processing is also an effective tool to consolidate metallic particles to produce bulk materials. In respect of consolidation, high-pressure torsion (HPT) is the most efficient technique because the processing is generally conducted under a high hydrostatic compressive stresses state and high shearing deformation. These conditions lead to the deformation and bonding of the particles while prevent cracking of the sample, enabling to process a wide range of materials. Many papers have reported the successful consolidation of pure metals [1, 2] alloys [3], and even harder materials such as partly amorphous [4] and fully amorphous [5] metallic glasses. Besides, a variety of metal-matrix composites were fabricated by HPT by the mixture of metallic particles and hard inert materials. For example, Al-based composites were produced by HPT processing of Al particles mixed with Al_2O_3 [6, 7] carbon nanotubes [8], fullerene [9] and Nb_2O_5 [10]. Recent papers also showed successful production of Mg-based composites with different reinforcement phases such as Al_2O_3 [11, 12], quasicrystal [13] and bioactive materials [14, 15]. These composites in which hard phases are incorporated, usually display an increase in strength in the range of Hall-Petch strengthening, as the inert phases enhance the grain refinement during HPT [16].

Moreover, HPT can be used for processing non-inert phases such as metals mixtures, and this provides the opportunity to induce solid-state reactions during deformation, enabling the achievement of further improvement in strength and other properties. Examples of reactions include the formation of supersaturated solid solutions [17, 18], segregation of alloying elements in crystalline defects [19], and the formation of different phases [20, 21]. Hence, there has been an increasing interest in the HPT of different metallic materials combined, either by consolidating a mixture of metal powders, machining chips, or by stacking different discs together. Many different systems have been processed including Al-Mg [22-28], Al-Cu [29], Ag-Ni [30], Cu-Ag [31-33], Cu-Co [34-37], Cu-Zr [38], Cu-Cr [18, 39], Cu-W [40-42], Cu-Ta [43], Fe-Cu [17, 38, 44, 45], Fe-V [38, 46], Fe-Zr [38], V-Zr [38, 45, 47], Zr-Nb [48], and Zn-Mg [49-51].

Among those systems, magnesium and zinc alloys are of great interest due to their high potential for biological applications since both are biocompatible and

biodegradable materials that could be used to produce temporary implants. Recent papers have shown that HPT processing does not affect the biocompatibility of Zn and Mg [52] and might even improve Mg corrosion resistance [53-55]. Although recrystallization and grain growth take place in pure Zn after HPT limiting the strengthening in this material [56], alloying with Mg usually lead to finer grain sizes and higher strength [52, 57, 58]. The main strengthening mechanism of the Zn-Mg system has been attributed to the Hall-Petch effect and precipitation of intermetallics [51]. Also, experiments with bulk Zn-Mg alloys have shown that grain growth is prevented and ultrafine grains are developed by hydrostatic extrusion [59]. In this study, a wide range of composition of Mg-Zn composites were synthesized by mechanical alloying of the elemental powders using HPT at room temperature. The microstructure and mechanical properties of the HPT-processed composites were systematically investigated. Special attention was given to the effect of Zn content on the deformation process and mixing of the different components.

8.2. Experimental Procedure

Magnesium particles with a sizing range of 20 to 200 μm and zinc powders with 2 to 10 μm in diameter were used in the present work. Scanning electron microscope (SEM) images of these initial materials are presented in Figure 8.1. The particles were separated into groups of pure magnesium, pure zinc and mixtures of Mg-20%wt Zn, Mg-50%wt Zn and Mg-95%wt Zn. Each group was prepared by hand mixing, cold-pressed at 400 MPa and processed by 10 and 20 turns of HPT using a nominal pressure of ~3.8 GPa and rotation speed of ~1 rpm. The discs had an initial diameter of 10 mm and thicknesses of ~1 mm. After HPT processing, the thickness of the discs was reduced to ~0.7 mm.

The processed discs were ground and polished using 3 μm and 1 μm diamond paste. Final polishing was carried out using colloidal silica suspension. The polished surfaces were observed using a JEOL 6360LV scanning electron microscope operating at 15 kV. X-ray diffraction was used on the polished surface to determine the major phases present. A Philips PW1710 diffractometer operating with Cu Kα radiation and a graphite monochromatic crystal with a wavelength of 1.5406 Å was used. The step was 0.01° with 2 s of time and the diffraction was collected in the range 30° - 65°.

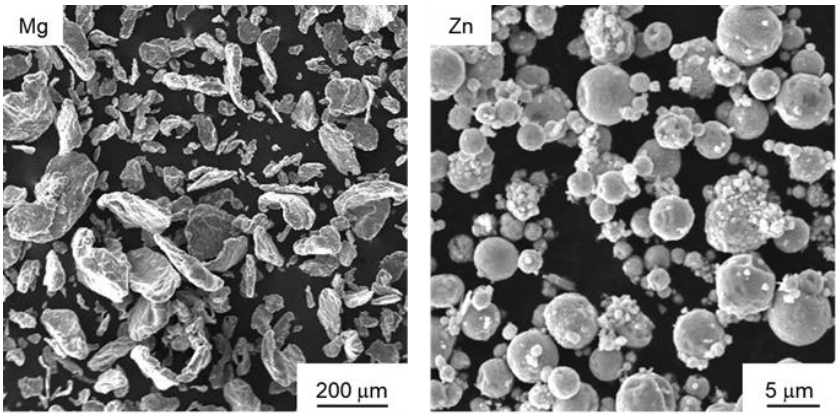

Figure 8.1 – Particles of Mg and Zn used to produce the composites.

Thin lamellae were extracted at ~4 mm from the disc center using focused ion beam milling. The lamellae were observed using a Tecnai G2-20 - SuperTwin FEI - 200 kV transmission electron microscope operated at 200 kV. Images were obtained using transmission (TEM) and scanning transmission electron microscopy (STEM) techniques, with bright-field (BF) and annular dark-field detection (ADF). Particularly, the Mg-20% Zn composite processed to 20 turns was also observed using STEM images on a FEI Titan Themis Cubed (FEI Company) operated at 300 kV, equipped with a Cs probe corrector. High angular annular dark field (HAADF) images were also obtained in order to provide better composition contrast. Local composition mapping was performed by using a Super-X EDS with four windowless silicon-drift detectors. The grain size was estimated by measuring the length of at least 50 different grains in each sample. It was not possible to distinguish the misorientation of grains and therefore subgrain boundaries were also considered grain boundaries.

Vickers microhardness tests were carried out at different locations using a load of 100 gf and 10 s of dwell time. The position of each indentation was recorded in order to determine its distance to the disc center which was used to estimate the effective strain imposed during HPT processing. A minimum of 5 indentations were carried out in locations with reduced scattering of the hardness and up to 20 indentations were carried out in areas with large scattering. Additionally, dynamic hardness tests were carried out at mid-radius locations of the discs using a Shimadzu DUH-211s equipment. A maximum load of 300 mN was applied for up to 999 s and the evolution of penetration depth was tracked with time. Care was taken to maintain a constant temperature during these tests. The time and depth were used to estimate the strain rate following the procedure reported in the

literature [60, 61]. The flow stress was estimated as the instant hardness divided by 3 [62] and plots of flow stress vs strain rate were used to estimate the strain-rate sensitivity.

8.3. Results

8.3.1. General microstructure

Figure 8.2 shows SEM images from backscattered electrons (SEM-BSE) of the surfaces of the processed samples. In Fig. 8.2.a, low magnification images of the discs processed to 10 (upper) and 20 turns (lower) of HPT are presented, where the bottom left of each image corresponds to the centre of the disc. Because the deformation imposed during HPT is proportional to the distance from the disc centre [63], the bottom left of each image corresponds to an area that underwent a lower plastic deformation; and the top right corresponds to an area submitted to larger strain. The image contrast observed in Fig. 8.2 is related to variations in the atomic number of the analyzed region. Thus, pure Zn (right) appears brighter and pure Mg (left) appears darker. Intermediate intensity levels can be also visualized in certain regions of the samples, which indicates the effective mixing of Mg and Zn at finer scales.

Higher magnification images taken at the mid-radius of the composites are presented in Figure 8.2.b. The contrast between different areas is clearly observed, thereby indicating that the Mg-rich and Zn-rich phases remain still present in all composites up to 20 turns of HPT. Nevertheless, thicknesses of the phases considerably decrease with an increasing number of HPT turns for the Mg-20% Zn and the Mg-50% Zn composites, suggesting a better mixing between the phases. The Mg-95% Zn composite - which is the only one having Zn as the major component - fails to show the occurrence of a greater mixing with increasing the number of HPT to 20 turns. In addition, an alignment between the phases and the shear direction can be observed in many areas of the discs, mostly Mg-20% Zn composite, as well as folding of phases in some areas. Bent phases with curvature radius higher than 1 µm are observed, mostly Mg-50% Zn composite. Both effects of alignment and folding of phases have been reported in the literature in multiphase materials processed by HPT [20, 38, 64, 65].

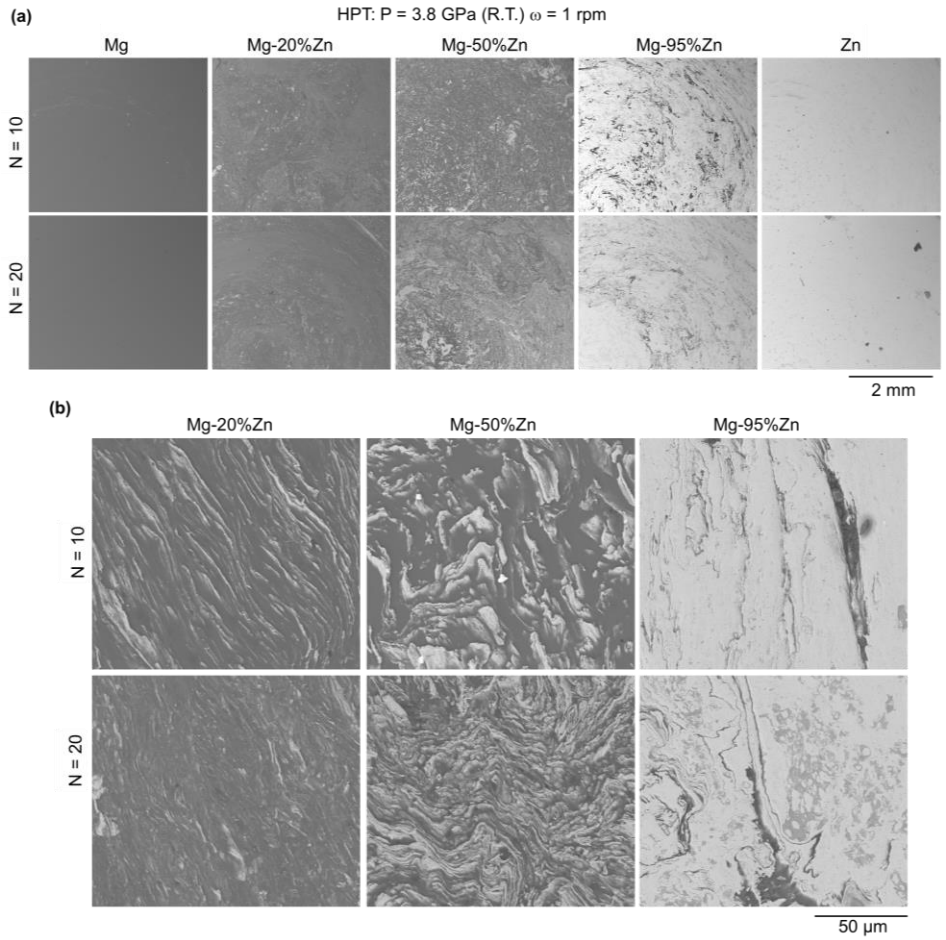

Figure 8.2 – BSE-SEM images of the Mg-Zn composites after 10 and 20 HPT turns: (a) general surface of all samples, and (b) surface at mid-radius of the Mg-Zn composites.

According to SEM investigation, it appears that HPT can fully consolidate pure Mg and Mg-Zn composites in which Mg occupies a larger volume fraction. However, pure Zn and Mg-95% Zn samples after 10 and 20 turns of HPT still exhibit some clear boundaries between original Zn particles, thereby indicating an apparent lack of bonding in these areas. Yet, a great majority of their volume was consolidated.

The X-ray diffraction peak profiles are shown in Figure 8.3 for the Mg-Zn composites, pure Mg and pure Zn discs after 10 and 20 HPT turns. The detected main constituent phases are Mg, Zn, ZnO, and $MgZn_2$. Zinc oxide peaks are clearly visible in the XRD patterns of all samples produced with Zn, which indicates that ZnO corresponds to a significant portion of the original particles. The presence of some naturally oxidized surface layer is expected on metallic particles. However, MgO peaks were not identified in XRD indicating that the fraction of this phase in the initial Mg particles is reduced. This is attributed to the larger size of the Mg particles and, consequently, reduced surface area prone to oxidation. All three Mg-

Zn composites exhibit the peaks related to $MgZn_2$, which confirms the occurrence of phase transformation and intermetallic formation during HPT processing. This agrees with recent observations of intermetallic formation in Zn-Mg composites produced by HPT processing of stacked discs [49-51]. In addition, the intensities of the peaks related to Mg or Zn are higher than the ones related to the other phases identified confirming that the pure metals are the major constituent of the composites.

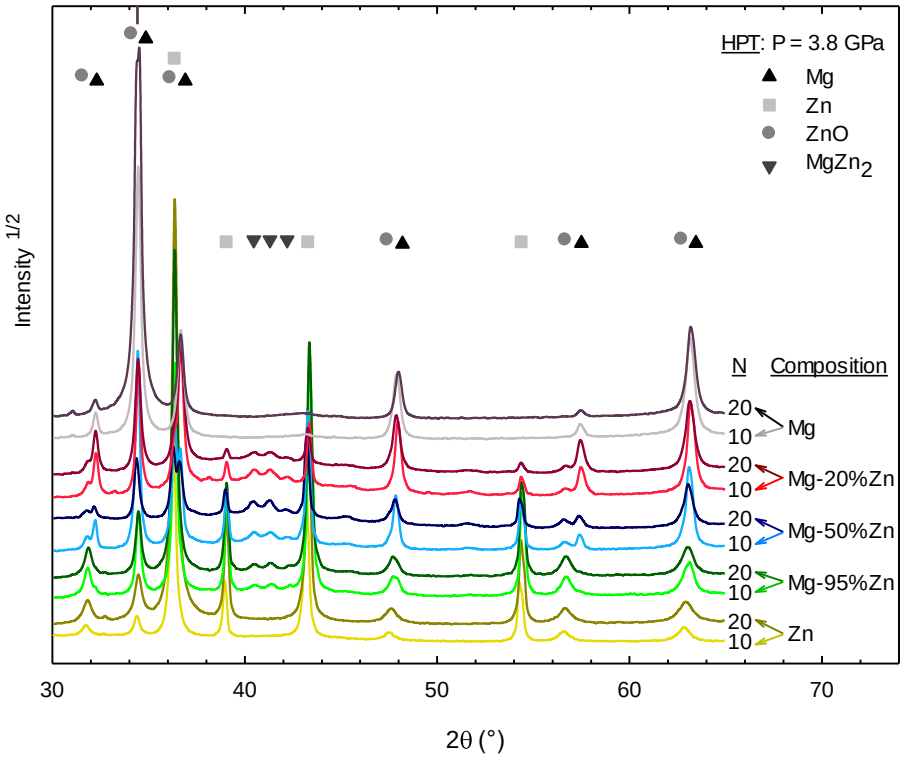

Figure 8.3 – X-ray diffraction patterns of the different materials.

8.3.2. Transmission electron microscopy

Transmission electron microscopy (TEM) analyses were carried out for a detailed examination of the microstructure of the Mg-Zn composites. Fig.8.4.a shows selected area electron diffraction (SAED) patterns of large areas of the lamellae of the three composites processed for 10 turns of HPT. These patterns confirm the presence of three main phases: Mg, Zn, and $MgZn_2$. The higher intensities of the SAED patterns are associated with the pure metals which agrees with the XRD results. Zinc oxide could not be properly distinguished in the patterns. Fig. 8.3.b-d presents STEM-BF images of the composites from which the patterns displayed in Fig. 8.4.a were taken. The Mg-20% Zn (Fig. 8.4.b) and Mg-50% Zn (Fig. 8.4.c)

samples exhibit thin (<100 nm) and elongated areas of Zn in the Mg matrices. Folding of the Zn-rich phase is also visible at the nanometer level in these composites. The Mg-95% Zn (Fig. 8.4.d) composite exhibits a comparatively coarse microstructure with elongated and folded Mg-rich areas in the Zn matrix. Submicrometer voids (the brightest regions) can be identified in the Mg-95% Zn composite, indicating poorer consolidation when compared to the other two composites.

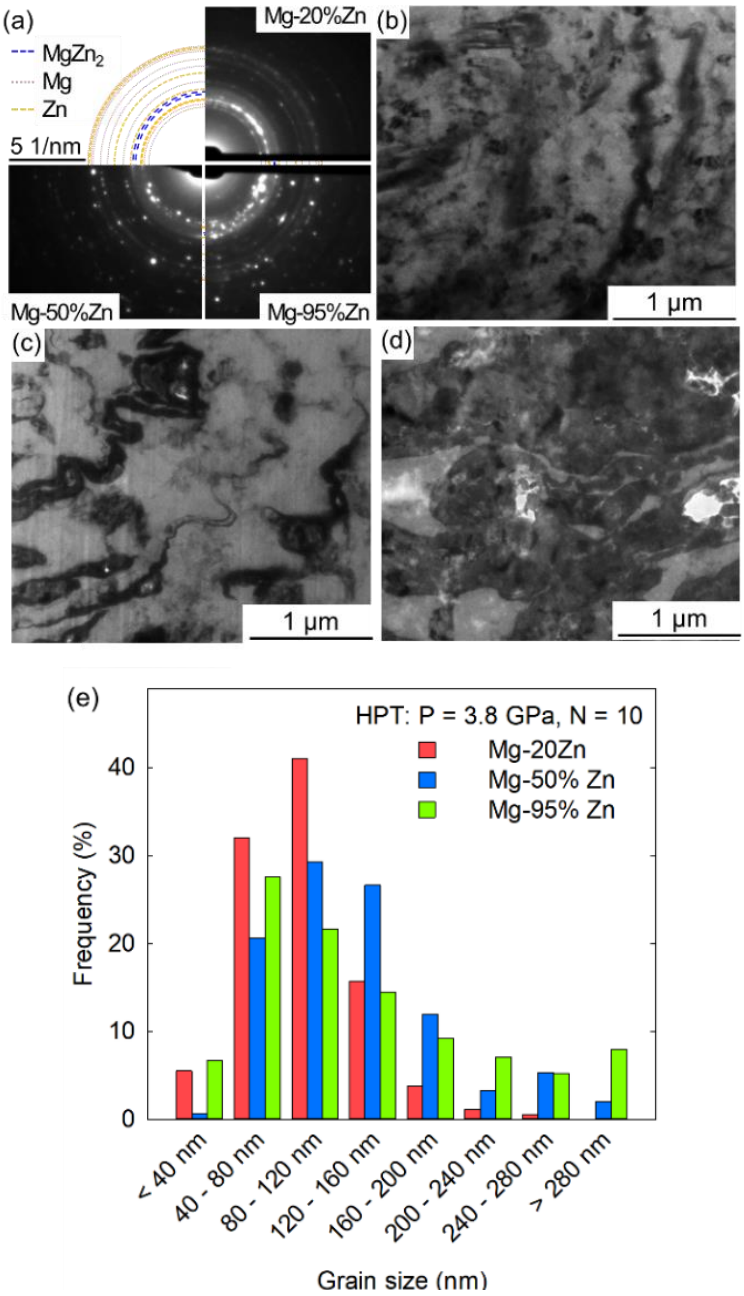

Figure 8.4 – Mg-Zn composites processed to 10 turns of HPT: (a) SAED patterns of the samples, (b-d) BF-STEM images of: b) Mg-20% Zn, c) Mg-50%Zn, and d) Mg-95% Zn; and (e) grain size distribution.

The grain size distributions of the Mg-Zn composites are presented in the histogram of Fig. 8.4.e. The composites display a broad range of grain sizes including grains smaller than 40 nm and grains larger than 240 nm. The average grain sizes measured were ~95 nm, ~130 nm, and ~135 nm for the Mg-20% Zn, Mg-50% Zn and Mg-95% Zn composites, respectively. In addition, the SAED patterns also suggest differences in grain sizes. The SAED patterns of Mg-50% Zn and Mg-95% Zn are significantly dotted which is evidence of coarse grains. On the other hand, the Mg-20% Zn pattern shows more uniform and diffuse rings, indicating smaller grains.

The STEM images shown in Figs. 8.5, 8.6, and 8.7 provide additional information on the microstructure of the Mg-20% Zn, Mg-50% Zn and Mg-95% Zn composites, respectively. The BF-STEM image of the Mg-20% Zn composite, shown in Fig. 8.4.a, confirms the refined grain structure with elongated strips (slightly darker than the matrix). These strips are attributed to Zn-rich areas and they have less than 100 nm thickness. The dark-field (DF) STEM image in Fig. 8.5.b reveals the presence of several isolated Mg-rich grains (bright) with less than 100 nm.

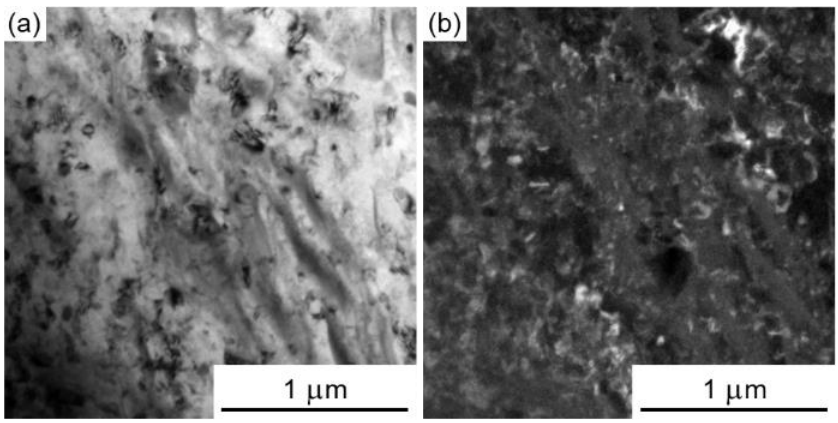

Figure 8.5 – STEM (a) BF and (b) DF images of the Mg-20% Zn composite processed to 10 turns of HPT.

Fig. 8.6.a presents an ADF-STEM image of the Mg-50% Zn composite. It is possible to distinguish Zn-rich areas (bright) dispersed in the Mg matrix. In addition, very thin layers (intermediate grey level) at the Mg grain boundaries can be distinguished which indicate the Zn segregation. Due to the contribution of diffraction effects in BF imaging, Fig. 8.6.b clearly shows long and thin strips of Zn (dark). These strips display thicknesses as thin as a few tens of nanometers and appear slightly folded. Figs. 8.6.c and 8.6.d show BF- and DF-STEM images of the

same area of the sample and reveal a wide range of grain sizes. The majority of grains observed in this composite have less than 100 nm in length, but some grains of hundreds of nanometers are also present. It is important to note that there was a limitation in the TEM examination to distinguish grains within the Zn-rich areas in both Mg-20% Zn and Mg-50% Zn composites.

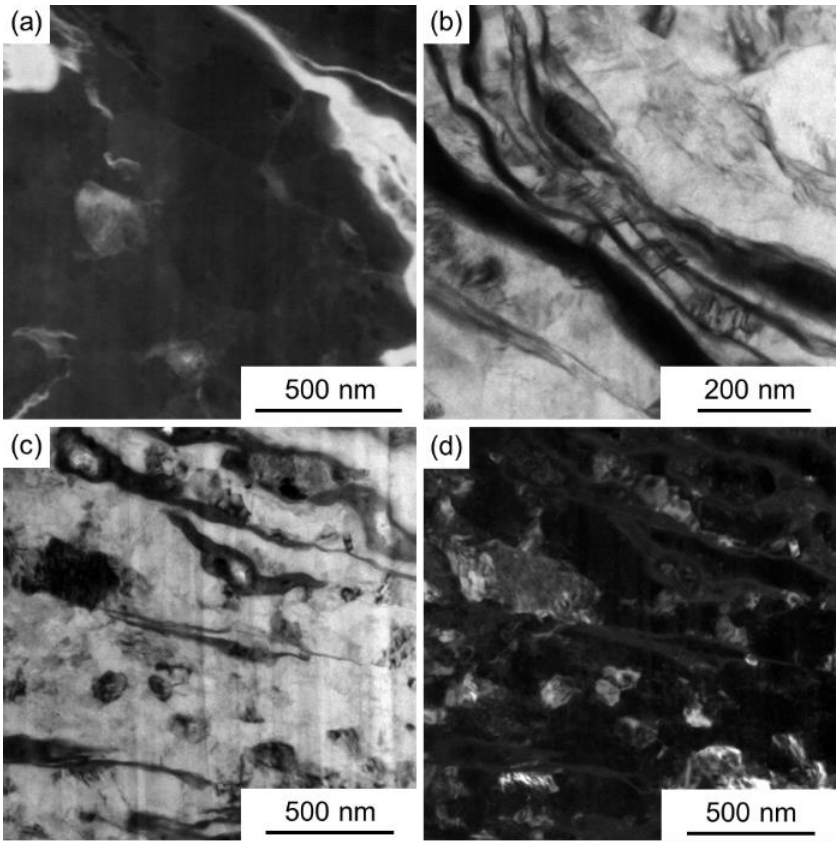

Figure 8.6 – (a) ADF-STEM, (b) BF, (c) BF, and (d) DF images of the Mg-50% Zn composite processed to 10 turns of HPT.

Further details of the structural features observed in the Mg-95% Zn composite after 10 turns of HPT are shown in Fig. 8.7. Areas with fine and distorted grains are distinguishable from some coarser grains with a clean interior in the BF-STEM image in Fig. 8.7.a, suggesting the partial recrystallization of this sample. This agrees with a report of recrystallization and grain growth at room temperature in zinc processed by HPT [56]. The ADF-STEM image in Fig. 8.7.b clearly shows grains with a broad range in sizes. Also, small black areas which correspond to pores can be visualized. These cavities support the idea that the surface oxide layer of the original Zn particle hindered the full consolidation. It is noted the presence of regions with an intermediate grey level at the Mg/Zn interfaces, which suggests the formation of a new phase during HPT processing. The thickness of

these layers lies in the range of tens of nanometers. The DF-STEM image with the corresponding diffraction pattern, shown in Fig. 8.7.c, reveals the presence of the $MgZn_2$ phase, evidenced by the weak rings and dots corresponding to 4.49 Å (100), 4.26 Å (002), and 3.97 Å (101) lattice spacings (planes), as indicated by the red dotted circle. Fig. 6.d shows an HRTEM image in which a lattice spacing of 4.49 Å is visible next to the Mg area (bright phase on the top right). This interplanar spacing is associated with $MgZn_2$ (100) planes.

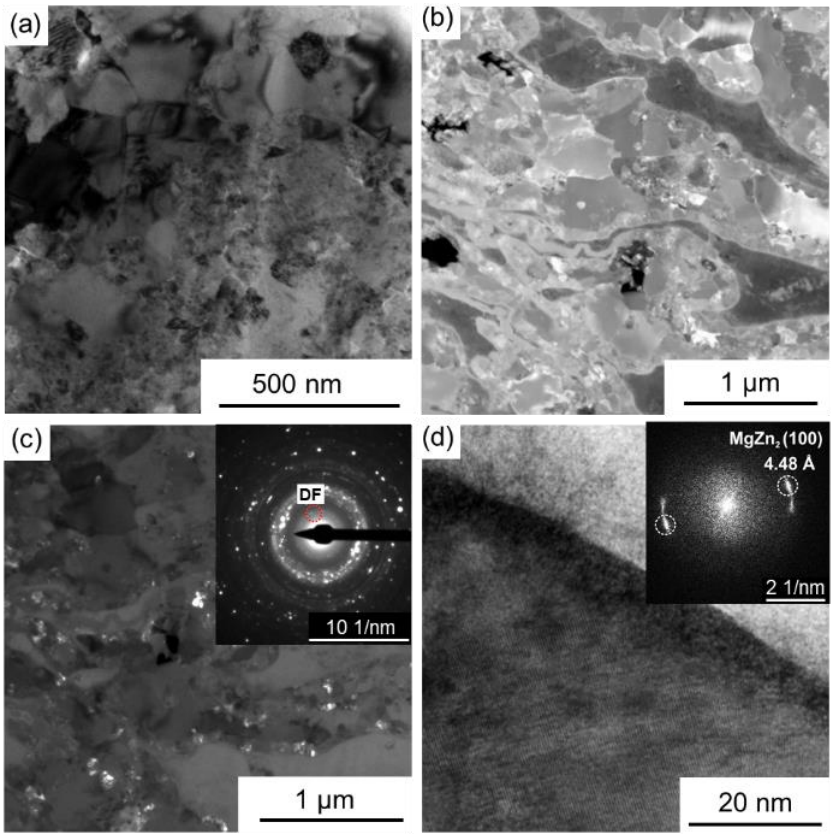

Figure 8.7 – Images of the Mg-95% Zn composite processed to 10 turns of HPT: (a) BF-STEM, (b) ADF-STEM, (c) DF with the corresponding diffraction pattern, and (d) HRTEM with the corresponding FFT.

For comparison purposes, DF-TEM images of the Mg-20% Zn composites processed to 10 and 20 turns of HPT are shown side by side in Fig. 8.8a, and the corresponding grain size distributions are presented in Fig. 8.8b. It is apparent that a significant grain refinement occurred with increasing numbers of turns of HPT. The average grain size decreased from ~95 nm to ~70 nm with the increase from 10 to 20 turns.

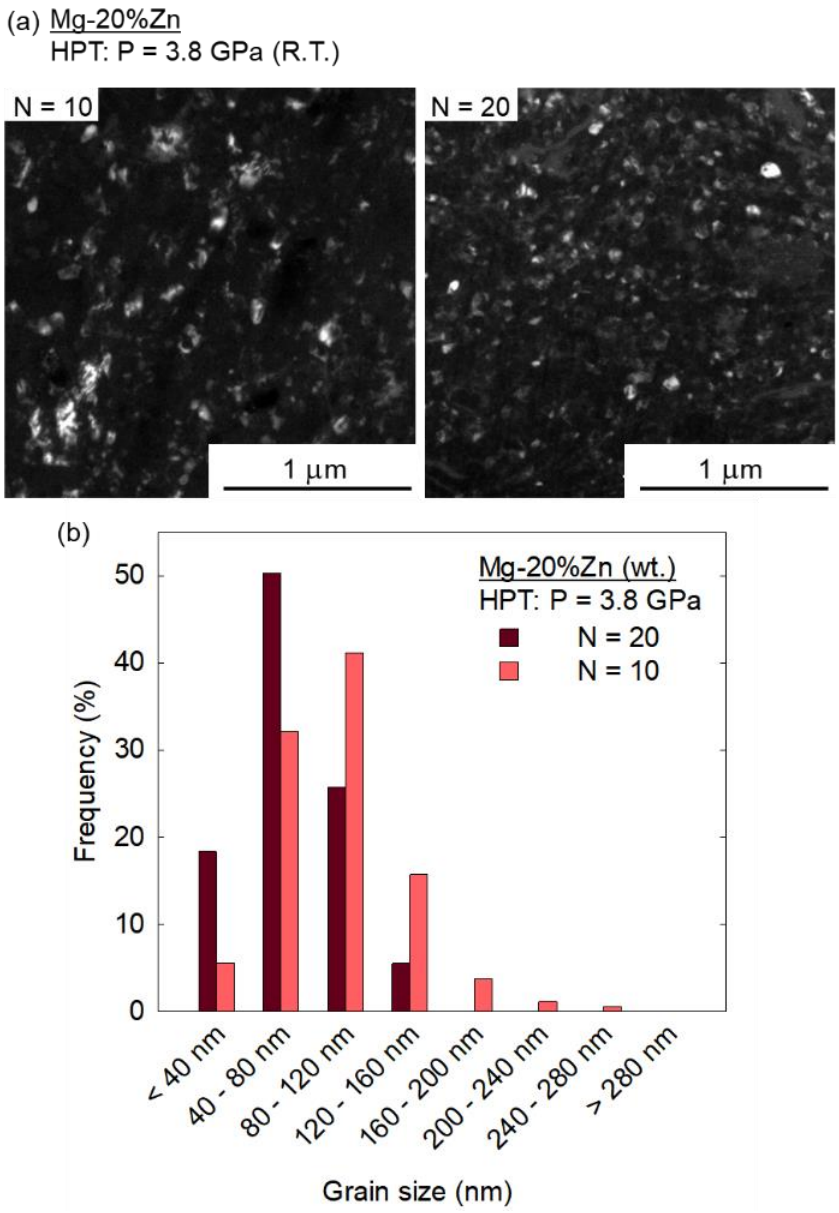

Figure 8.8 – Mg-20% Zn composites processed to 10 and 20 turns of HPT: (a) DF-TEM images and (b) the grain size distributions.

Fig. 8.9 presents additional information on the microstructure of the Mg-20% Zn composite processed to 20 turns of HPT. The HAADF-STEM image, displayed in Fig. 8.9.a, show that the morphology of the Zn-rich phases (bright) is quite heterogeneous throughout the sample. Figs. 8.9.b, 8.9.c, and 8.9.d correspond to magnified views of the regions indicated by red squares in Fig. 8.9.a. Fig. 8.9.b shows folded regions of Zn, whereas elongated ribbons with thicknesses ranging from few to tens of nanometers are observed in Figs. 8.9.c and 8.9.d. These findings indicate that areas of the composite distanced few microns apart from each other experienced different shear paths and deformations. Fig. 8.9.b reveals two folded Zn ribbons less than 100 nm apart connected by extremely thin bright

lines. These lines indicate the segregation of Zn along Mg boundaries. Fig. 8.8.c shows a high magnification image of region c in Fig. 8.9a and the EDS mapping associated with the region confirms that the bright areas are rich in Zn and the dark matrix is rich in Mg. The images show that Zn-rich veins separate the volumes of Mg as thin as a few tens of nanometers. Fig. 8.9.d shows a coarse volume of Zn surrounded by Zn fragments. This observation suggests the fragmentation of the initial components during HPT processing. Careful analysis of the HAADF-STEM image in Figs. 8.9.e and 8.9.f reveal that the Mg grain size differs significantly in close proximity to the Zn phase. For instance, the Mg grains close to the Zn-rich areas on the bottom Fig. 8.9.f are clearly smaller and extensive segregation of Zn can be observed at the boundaries of these grains. The region of the upper part of Fig. 8.9.f displays coarser Mg grains with the presence of the Zn segregations in more than ~100 nm distancing. This indicates that higher levels of Zn segregations can prevent grain growth and reduce the grain size of Mg.

Fig. 8.10.a shows a HAADF-STEM image of the Mg-20% Zn composite revealing different Zn-rich areas including some clusters with ~2 nm in size. A high-resolution image of the area marked in red around these particles is shown in Fig. 8.10.b, in which is possible to distinguish atomic planes in one of them. The respective Fast Fourier Transform (FFT) and a line profile of HAADF intensity are shown on the right side of this image and a spacing of 2.31 Å was determined, which is associated with Zn (100) planes.

The formation of $MgZn_2$ in the Mg-20% Zn composite processed to 20 turns of HPT could be confirmed. As it is shown in Fig. 8.10.c, the precipitates were located preferentially associated to grain boundaries which were decorated by Zn atoms and their sizes were in the range of tens of nanometers. Higher magnification of one of these precipitates which were located at a grain boundary triple junction is shown in Fig. 8.10.d. The FFT of the high-resolution image reveals atom positions associated with the Mg grains and positions having an interplanar spacing of 4.0 Å which is associated with $MgZn_2$ (101) planes.

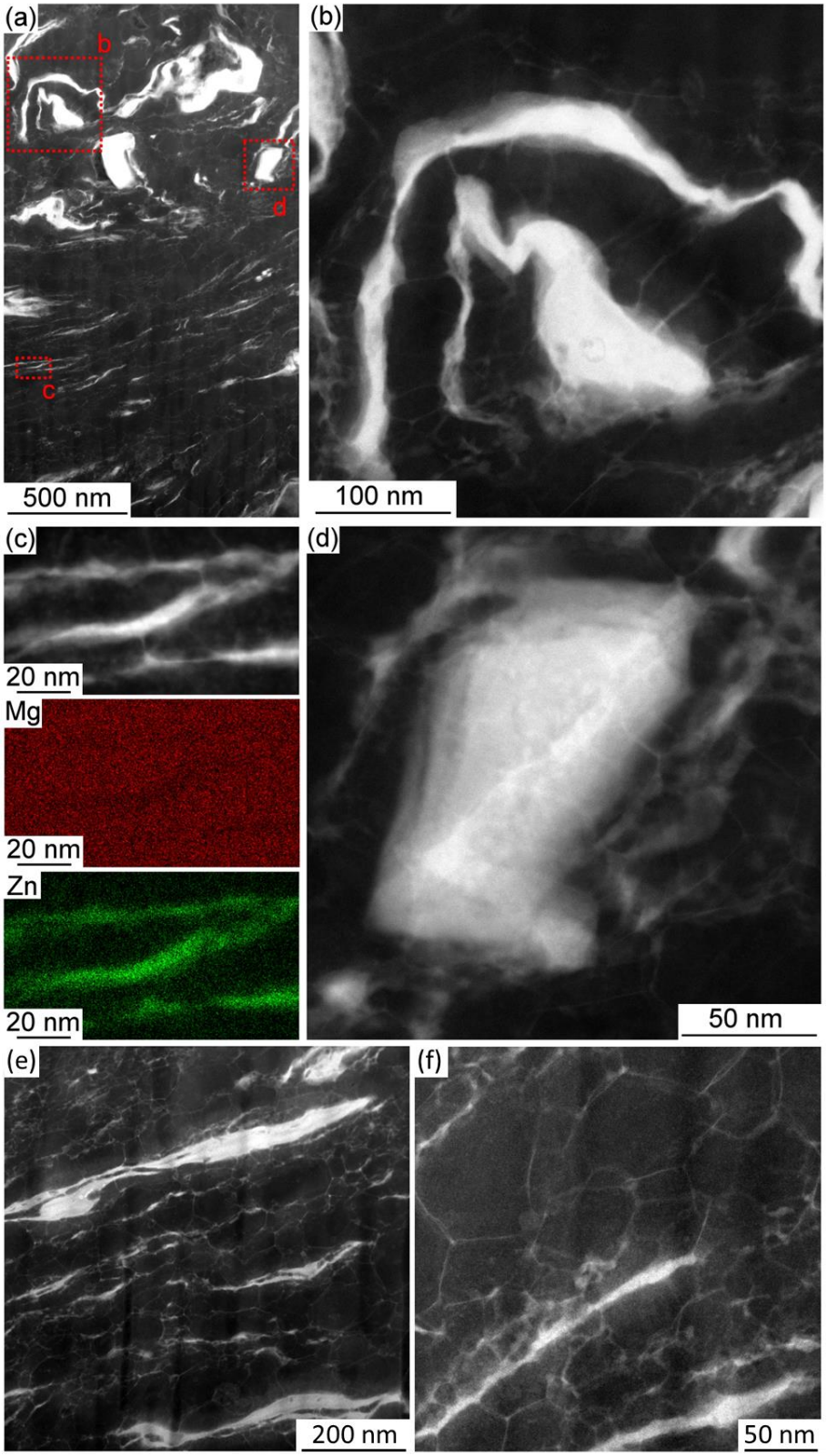

Figure 8.9 – HAADF-STEM and EDS composition maps of the Mg-20% Zn composite processed to 20 turns of HPT.

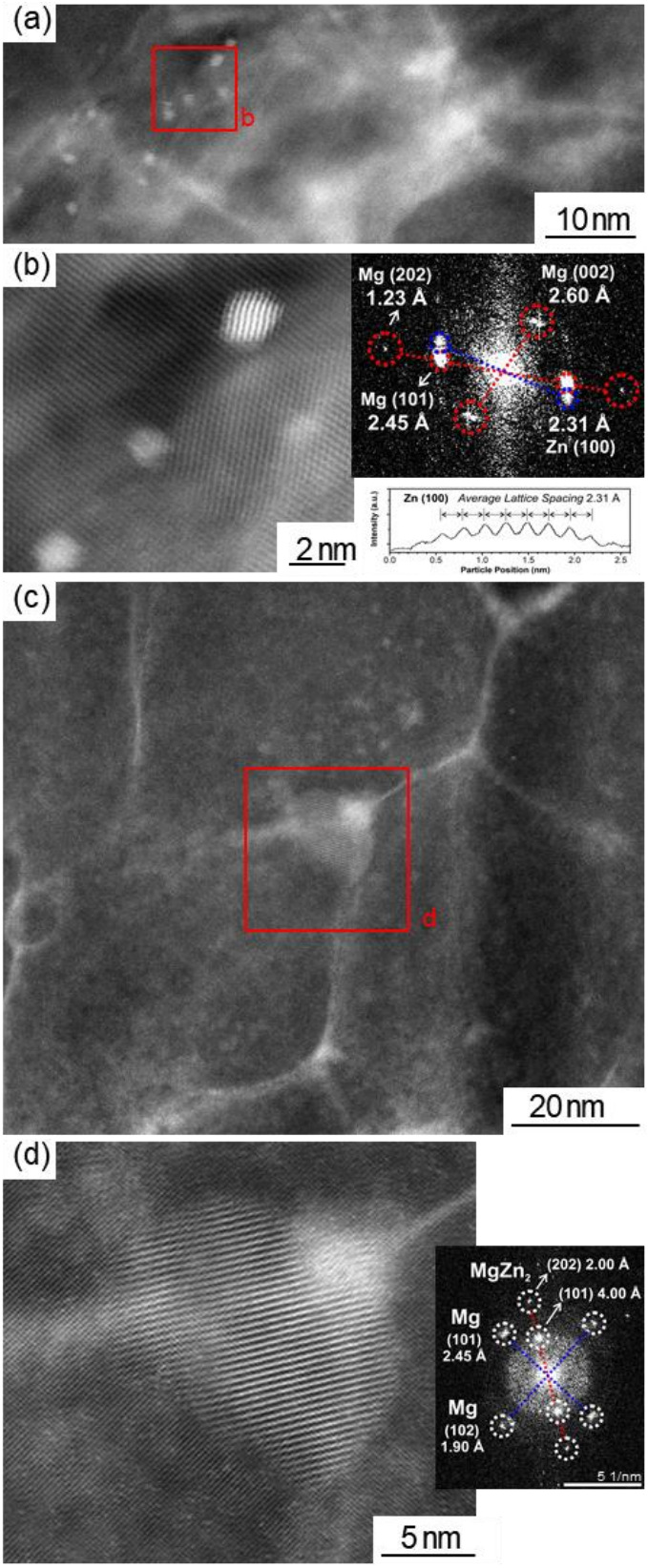

Figure 8.10 – Mg-20% Zn composite processed to 20 turns of HPT: (a) HAADF-STEM, (b) insert HAADF and respective FFT and HAADF intensity profile, (c) HAADF-STEM of an $MgZn_2$ precipitate at a grain boundary, and (d) insert HAADF and respective FFT.

8.3.3. Mechanical properties

Figure 8.11 summarizes the mechanical properties of the HPT-processed samples. Figure 8.11.a shows the evolution of microhardness as a function of the effective strain imposed on the materials. The continuous lines serve as a guide to the eyes. Pure Zn and pure Mg samples display reasonably constant hardness values at ~45 HV and ~55 HV, respectively, with increasing equivalent strain. The lack of hardening agrees fairly well with reports in the literature for bulk Zn [56] and Mg [54, 66]. All Mg-Zn composites display higher hardness than the pure metals and distinct hardening stages. It is interesting to note that the composites present a near saturation in hardness at strains of ~100 but a second hardening stage takes place at even higher strains. At strains >300, the Mg-50% Zn exhibits the highest hardness among the composites (some measurements give hardness values above 170 HV) while the Mg-95% Zn shows the lowest (hardness values not higher than 120 HV).

Dynamic hardness tests were used to estimate the strain-rate sensitivity, *m*, of all the HPT-processed materials. Figure 8.11.b shows representative curves of flow stress plotted as a function of the strain rate and the slopes of these curves can estimate the values of m. The estimated m values are summarized for the materials in Figure 8.11.c where the average microhardness values are indicated by squares and the m values are indicated by circles (determined for strain-rates lower than ~10^{-4} s^{-1}) and are plotted as a function of the Zn content in the composite for the samples processed to 10 and 20 turns. Both, pure Mg and pure Zn display curves with a high slope which agrees with reports of high strain-rate sensitivity in pure Mg processed by HPT [61, 67] and in pure Zn [68]. The composites also display a high strain-rate sensitivity after processing by 10 turns of HPT only. However, increasing the number of turns in HPT increased their hardness and reduced their strain-rate sensitivity.

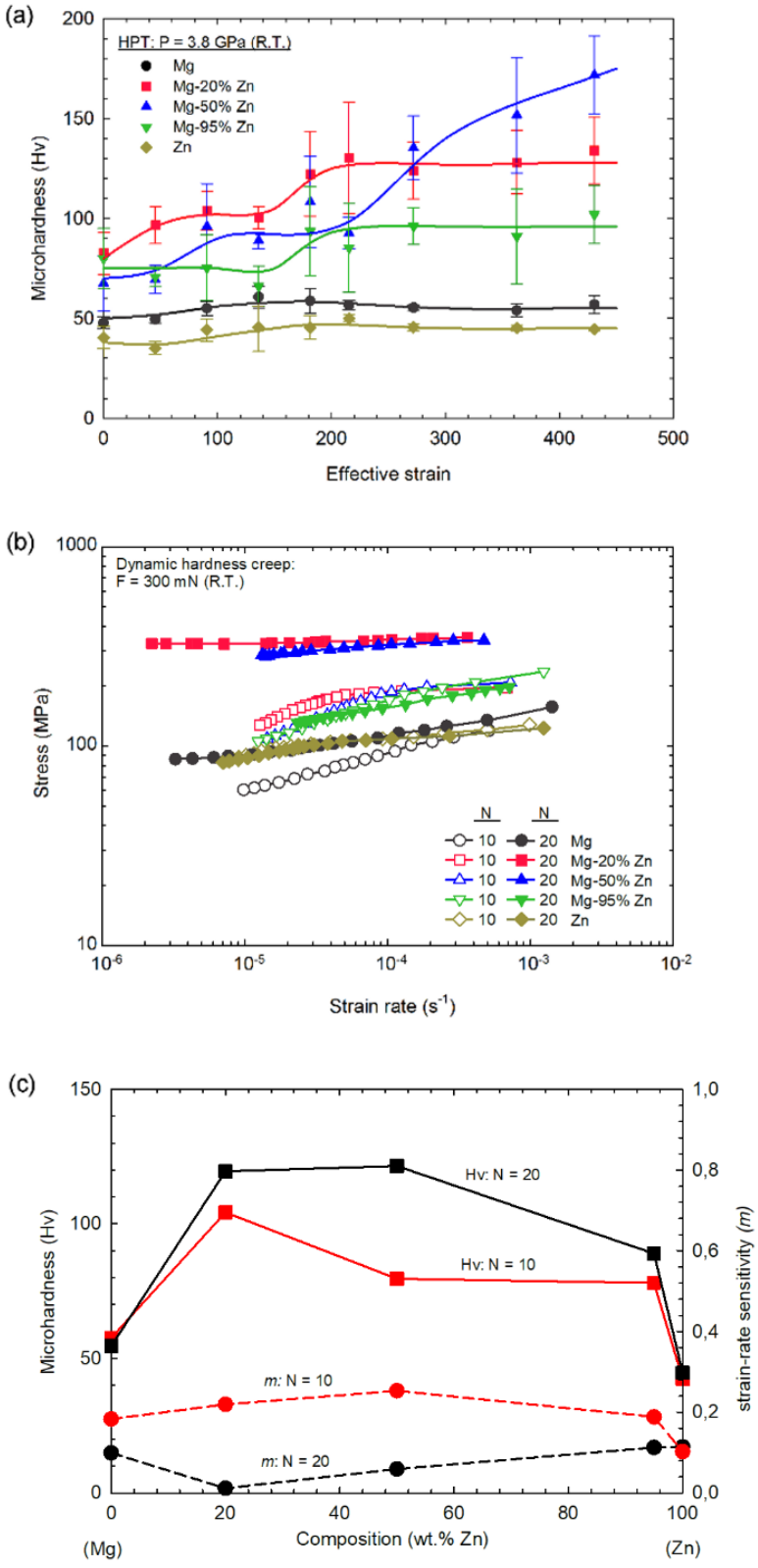

Figure 8.11 – (a) Vickers microhardness vs effective imposed strain and (b) stress vs. strain rate for the different materials and (c) microhardness and strain-rate sensitivity plotted as a function of the Zn content.

8.4. Discussion

8.4.1. Mixing of phases and formation of segregations

The present HPT consolidation of dissimilar metal powders is anticipated to introduce continuous and homogeneous shear deformation promoting thinning and alignment of phases along the shear direction. This effect has been observed in many multi-phase materials such as Fe-Cu [17] and Cu-Ag alloys [69], and pearlitic steel [70]. However, it is now known that the homogeneity of deformation during HPT can be affected by processing conditions such as anvil misalignment [71-73] and friction between the anvil and the sample [74]. The presence of different phases can also induce local heterogeneities in deformation and finite element modelling has shown changes of local material velocity, thus plastic instability, due to the presence of phases with different strength [75-79]. The heterogeneity of deformation in HPT can induce variations in hardness along the thickness of samples [80-82] and also develop local vortices of material flow inducing the curving of different phases. Vortex-like patterns have been observed using optical microscopy and SEM in many multi-phase materials [69, 77, 83, 84].

Experiments by stacking dissimilar metal discs revealed the microstructural evolution with different patterns upon HPT deformation. Continuous thinning of phases occurs due to delamination of individual layers in the early stage of deformation in stacked discs of Ag and Cu while folding of Cu layers takes place in Al and Cu stacked discs [64]. However, after larger deformation both systems develop tangled and turbulent-like patterns indicating pronounced mixing at the nanometer and even atomic scales. These different patterns were successfully predicted using numerical simulations in which the phases were treated as nonlinear viscous fluids with different viscosity ratios [64]. A recent paper [38] also combine different materials (Fe, V, Zr, Cu) using HPT to evaluate the formation of turbulent flow at their interface, and concluded that the structure evolution depends on the hardness ratio between the phases and their deformation capacity. It was shown that significant differences in hardness between the materials lead to smooth interfaces while similar levels of hardness and deformation capacity induce multi-layered vortex structure. Thus, when there is a significant difference in hardness between the phases, the softer phase accounts for most of the deformation inhibiting deformation of the harder phase and good mixing. Turbulent

flow and vortices formation are associated with increased deformation and promote better mixing of phases.

The present results show evidence of both co-deformation and bending of phases at different length scale in the Mg-20% Zn and Mg-50% Zn composites. In practice, bent phases with curvature radius higher than 1 µm was observed using SEM and bent phases with a curvature radius of ~100 nm were observed using TEM/STEM. Thus, the heterogeneity of plastic flow reported for many systems at microscale also takes place at sub-micron scale and contribute to the mixing of phases. On the other hand, the Zn-rich Mg-95% Zn composite did not display significant mixing, and Zn and Mg phases appear elongated as shown in Fig. 8.1.b and Fig. 8.3.d, suggesting co-deformation. Also, the Mg phase is thicker in this Zn-rich composite than the Zn phase in Mg-rich composites. This suggests that Zn is softer and undergoes larger deformation, which agrees with the slightly lower hardness in pure Zn discs when compared to the values in pure Mg discs. The observation of a thick and continuous layer of $MgZn_2$ intermetallic around the Mg phase also supports the assumption that this phase undergoes less deformation. The plastic deformation of the Mg phase would lead to a breakup of the intermetallic layer. It is worth noting that turbulent-like flow features are not readily observed in the Mg-95% Zn composite and such plastic instability of two elements under deformation could improve mixing.

In addition to bending, pronounced fragmentation of the Zn phase was observed in the Mg-20% Zn and Mg-50% Zn composites. Careful observation of the area surrounding the Zn particles suggests that mechanical fragmentation takes place at a nanometric scale. It is expected that diffusion assisted dissolution of the Zn phase would lead to a continuous gradient in composition around the Zn particles. However, discrete nanometric volumes of Zn are clearly observed surrounding these particles. The morphology of the Zn particle and fragments, depicted in Fig. 8.d resembles the reported finite element simulations of shearing of nonlinear fluids with different viscosities [64]. This supports the assumption that mechanical mixing, rather than atomistic diffusion, plays a major role in mixing Mg and Zn phases.

The small, and sometimes nano-scale, pieces of Zn undergo severe shear leading to the formation of very thin and aligned Zn ribbons in the Mg matrix. The thickness of these ribbons can be so small that they may segregate along Mg grain

boundaries as shown in Fig. 8.9.a. It is important to note that such segregations of Zn were observed throughout the Mg matrix forming a continuous network of segregations. The thick Zn ribbons are aligned along the shear direction, but thin segregations of Zn are observed in all orientations implying that diffusion also plays a role in their formation. Thus, the mechanical fragmentation and mixing of phases reduce the distance between Zn particles and therefore facilitate the formation of diffusion-assisted Zn segregations along grain boundaries. Such segregations along grain boundaries act as potential sites for the nucleation of $MgZn_2$ intermetallics.

8.4.2. Model for structure and mechanical properties evolution

The evolution of hardness with imposed strain shows discrete hardening stages in the composites. These hardening stages reported in systems fabricated by HPT mixing and consolidation of metal powders are attributed to microstructural changes during the mixing of phases. Different models of hardness evolution are proposed based on the fraction of each phase and their strength ratio [85]. In the present study, a model for the hardness and structure evolution is presented in Fig. 8.12 based on microstructural features observed.

Fig. 8.12.a illustrates the hardness evolution after the HPT process for single-phase materials such as pure Mg and pure Zn (black line) and for multi-phase materials such as the Mg-Zn composites (red line). Single-phase metallic materials and most alloys display a conventional strain hardening behaviour during HPT processing in which the hardness increases at low strains and saturates in a high value [86]. The increase in hardness is associated with grain refinement which is illustrated by sequence 8.12.b-c. The saturation in hardness is associated with a steady structure that remains constant with further deformation. Grain refinement of each phase is also expected at low strains in immiscible systems as the Mg-Zn composites, increasing the overall hardness of the material. This initial grain refinement is illustrated by sequence 8.12.d–e which shows refined and agglomerated grains forming elongated phases. Further deformation promotes the stretching and fragmentation of the phases and segregations of elements around the phases' interfaces, reducing grain boundary mobility and enabling further grain refinement in the local areas. This is illustrated in Fig. 8.12.f which shows grain boundaries without segregations (black lines) and finer grains separated by boundaries with segregations (red lines). Consequently, there is a broad

distribution of grain sizes at this stage as observed in the composites processed to 10 turns of HPT. As the fragmentation of phases and segregations are still restricted to some areas, there is no significant increase in hardness. However, further deformation leading to the stretching of the phases reduces the distance between the ribbons, increasing the amount of segregations. This process goes on until the whole sample is affected by the mixing of elements, as illustrated in Fig. 8.12.g, and this microstructural refinement is associated with a significant increase in hardness. The decrease in overall grain size, the narrowing of the range of grain sizes, fragmentation and thinning of phases and increase in hardness agree with the present observations in the Mg-20% Zn composite processed to 20 turns.

Precipitation of intermetallics is expected in the Mg-Zn system. The pronounced segregations of Zn along Mg grain boundaries convert these boundaries into sites for precipitation of $MgZn_2$ intermetallic. In fact, nanometric precipitates of $MgZn_2$ were observed at Mg grain boundaries in the Mg-20% Zn composite processed by 20 turns of HPT (see Fig. 8.9). As a consequence, the Zn segregations harden the Mg grain boundaries and prevent grain boundary sliding, which is the deformation mechanism responsible for the inverse Hall-Petch behaviour [87] and enhanced strain-rate sensitivity [61] in pure Mg. The tendency for precipitation of intermetallics is illustrated in Fig. 11.h while segregations of elements that do not precipitate intermetallics are illustrated in Fig. 8.12.i.

An analysis of data in the literature for different metallic systems processed by SPD suggests that the tendency of formation of intermetallics plays a major role in evolution of strength and strain-rate sensitivity when segregations are developed. For example, HPT mixing of Mg and Al, which tend to form intermetallics, is associated with hardening [25, 27, 28, 88] while HPT processing softened and increased the strain rate sensitivity of an Mg-Li alloy [89], which do not form intermetallics. Also, improved strain-rate sensitivity was reported in an Al-7% Si alloy processed by HPT [90] and the Al-Si system do not display intermetallics. Moreover, it has been shown that HPT processed Zn-Al alloys, which do not form intermetallics, may be softer than the pure components Zn and Al. It has been reported that HPT processing increases the strain-rate sensitivity [91] and may soften [92] a Zn-22% Al alloy. Also, experiments showed that HPT processing of an Al-30% Zn alloy induce formation of Zn segregations along Al grain boundaries

which favors the occurrence of grain boundary sliding [93, 94], increases strain-rate sensitivity and can introduce superplastic behavior [95].

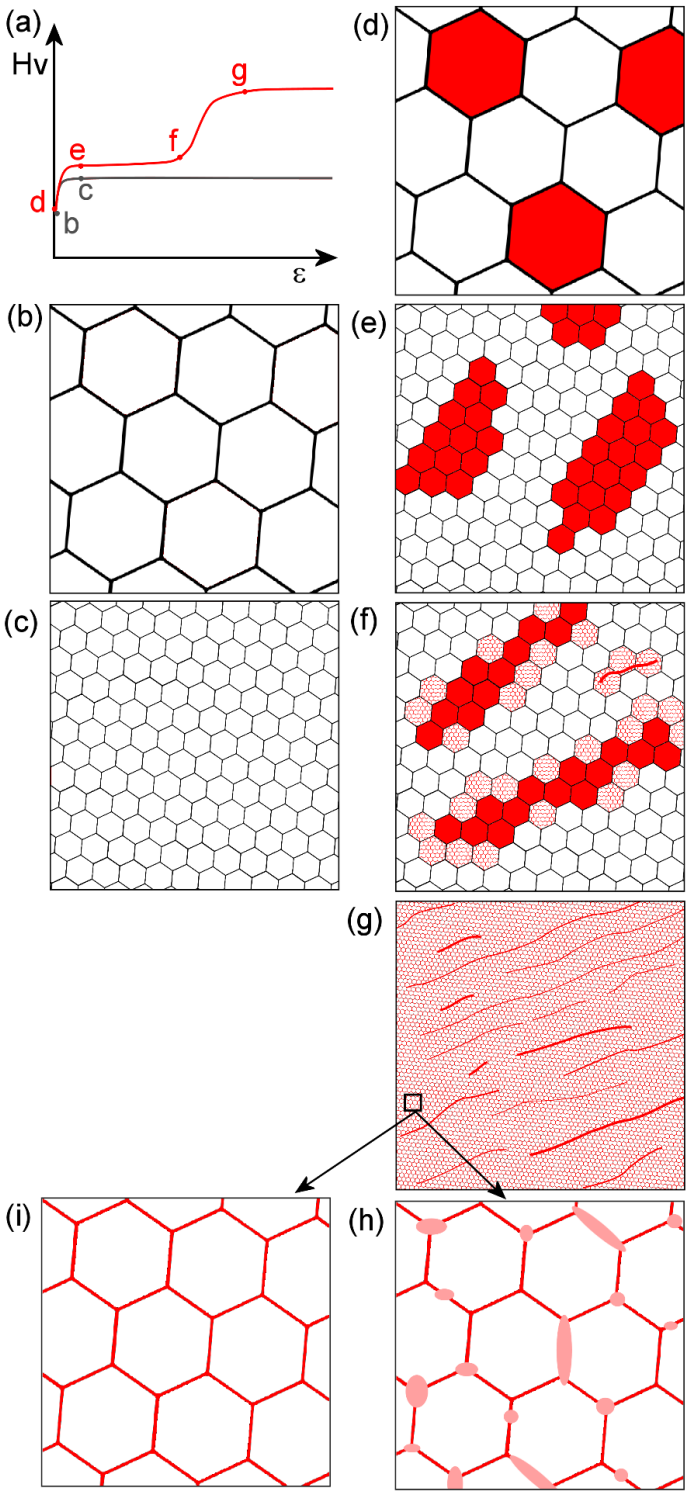

Figure 8.12 – Model for hardness and microstructure evolution of single-phase materials and multi-phase materials.

However, the present experiments show that HPT processing of the Mg-Zn composites induces significant hardening and reduces strain-rate sensitivity after 20 turns despite the introduction of finer grain sizes. Thus, the formation of Zn segregations along grain boundaries, which was associated with improved strain-rate sensitivity in the Al-Zn system [93, 94], is associated with an increase in strength and decrease in strain-rate sensitivity in the present experiments. The difference in behaviour is attributed to the tendency of forming precipitates in the different systems.

Thus, the present results, which show HPT induced hardening of Mg-Zn composites, agree with other reports of HPT processing of metallic systems associated with intermetallic formation, such as the Mg-Al. The reduced strain-rate sensitivity observed in the Mg-20% Zn and Mg-50% Zn composites processed to 20 turns of HPT is therefore attributed to a Zn segregation hardening of grain boundary areas that prevent grain boundary sliding.

8.5. Summary and Conclusions

1- Pure Mg and pure Zn particles were mixed in different proportions and consolidated into discs with different compositions using high-pressure torsion. Full consolidation was observed in discs of pure Mg and Mg-20% Zn and Mg-50% Zn composites. Lack of bonding was observed at isolated areas in Mg-95% Zn composite and pure Zn discs.

2- The mixing of phases differs between Mg-rich and Zn-rich composites. Folding, fragmentation and elongation into thin ribbons were observed in the Zn phase in Mg-rich composites. The Mg phase appears less deformed in the Zn-rich composite. $MgZn_2$ intermetallics were formed in all composites but its morphology differs.

3- Mechanical deformation plays a major role in mixing the phases and diffusion contributes to the development of grain boundary segregations. It is shown by the formation of $MgZn_2$ at a Zn segregation along Mg grain boundary.

4- Mg-Zn composites display pronounced hardening and decrease the strain-rate sensitivity with increasing the deformation imposed by HPT. This evolution in mechanical properties differs in the pure Mg and pure Zn observed in the present

study and from the reports for the Al-Zn and Mg-Li systems. These effects are attributed to the tendency of formation of intermetallics at segregations at grain boundaries which prevent grain boundary sliding.

5- Discrete hardening stages are observed in the Mg-Zn composites and are attributed to the slow evolution of the microstructure and the high amount of strain required to develop segregations. Smaller grain sizes are observed in Mg near areas with significant segregations of Zn.

6- A model is proposed to explain the mixing of phases and their relation to the evolution of mechanical properties.

8.6. Author contributions

M.M.C. carried out sample preparation, HPT processing, hardness and dynamic hardness tests, and contributed to microstructure characterization, XRD analysis, first and final version of the manuscript.

8.7. Acknowledgements:

The authors thank the Microscopy Centre of UFMG and the Electron Microscopy Laboratory from LNNano/CNPEM for providing the equipment and technical support during electron microscopy analysis. M.M.C. acknowledges a research fellowship from CAPES. This work was partly supported by CNPq (Grant No. 302445/2018-8), FAPEMIG and CAPES-Proex. This study was partly supported by the National Science Foundation of the United States under Grant No. DMR-1810343 (M.K.).

8.8. References

1. Alexandrov IV, Zhu YT, Lowe TC, Islamgaliev RK, Valiev RZ. Consolidation of nanometer-sized powders using severe plastic torsional straining. Nanostructured Materials. 1998;10(1):45-54.
2. Zhilyaev AP, Gimazov AA, Raab GI, Langdon TG. Using high-pressure torsion for the cold consolidation of copper chips produced by machining. Materials Science and Engineering: A. 2008;486(1):123-6.

3. Yavari AR, Botta WJ, Rodrigues CAD, Cardoso C, Valiev RZ. Nanostructured bulk Al90Fe5Nd5 prepared by cold consolidation of gas atomized powder using severe plastic deformation. Scripta Materialia. 2002;46(10):711-6.

4. Botta WJ, Fogagnolo JB, Rodrigues CAD, Kiminami CS, Bolfarini C, Yavari AR. Consolidation of partially amorphous aluminium-alloy powders by severe plastic deformation. Materials Science and Engineering: A. 2004;375-377:936-41.

5. Edalati K, Yokoyama Y, Horita Z. High-Pressure Torsion of Machining Chips and Bulk Discs of Amorphous Zr50Cu30Al10Ni10. Materials Transactions. 2010;51(1):23-6.

6. Alexandrov IV, Islamgaliev RK, Valiev RZ, Zhu YT, Lowe TC. Microstructures and properties of nanocomposites obtained through SPTS consolidation of powders. Metallurgical and Materials Transactions A. 1998; 29(9):2253-60.

7. Ashida M, Horita Z, Kita T, Kato A. Production of Al/Al_2O_3 Nanocomposites through Consolidation by High-Pressure Torsion. Materials Transactions. 2012; 53(1):13-6.

8. Tokunaga T, Kaneko K, Horita Z. Production of aluminum-matrix carbon nanotube composite using high pressure torsion. Materials Science and Engineering: A. 2008;490(1):300-4.

9. Tokunaga T, Kaneko K, Sato K, Horita Z. Microstructure and mechanical properties of aluminum–fullerene composite fabricated by high pressure torsion. Scripta Materialia. 2008;58(9):735-8.

10. Silva C, Montoro LA, Martins DAA, Machado PA, Pereira PHR, Gonzalez BM, *et al.* Interface structures in Al-Nb_2O_5 nanocomposites processed by high-pressure torsion at room temperature. Materials Characterization. 2020;162:110222.

11. Castro MM, Pereira PHR, Isaac A, Figueiredo RB, Langdon TG. Development of a magnesium-alumina composite through cold consolidation of machining chips by high-pressure torsion. Journal of Alloys and Compounds. 2019;780:422-7.

12. Castro MM, Pereira PHR, Isaac A, Langdon TG, Figueiredo RB. Inverse Hall–Petch Behaviour in an AZ91 Alloy and in an AZ91–Al_2O_3 Composite Consolidated by High-Pressure Torsion. Advanced Engineering Materials. 2019;n/a(n/a):1900894.

13. Castro MM, Wolf W, Isaac A, Kawasaki M, Figueiredo RB. Consolidation of magnesium and magnesium-quasicrystal composites through high-pressure torsion. Letters on Materials. 2019;9(4):546-50.

14. Castro MM, Lopes DR, Soares RB, dos Santos DMM, Nunes EHM, Lins VFC, *et al.* Magnesium-Based Bioactive Composites Processed at Room Temperature. Materials. 2019;12(16):2609.

15. Lopes D, Soares RB, Castro MM, Figueiredo RB, Langdon TG, Lins VFC. Corrosion Behavior in Hank's Solution of a Magnesium–Hydroxyapatite Composite Processed by High-Pressure Torsion. Advanced Engineering Materials. 2020; 2000765.

16. Bachmaier A, Hohenwarter A, Pippan R. New procedure to generate stable nanocrystallites by severe plastic deformation. Scripta Materialia. 2009; 61(11):1016-9.

17. Bachmaier A, Kerber M, Setman D, Pippan R. The formation of supersaturated solid solutions in Fe–Cu alloys deformed by high-pressure torsion. Acta Materialia. 2012;60(3):860-71.

18. Sauvage X, Jessner P, Vurpillot F, Pippan R. Nanostructure and properties of a Cu–Cr composite processed by severe plastic deformation. Scripta Materialia. 2008;58(12):1125-8.

19. Sauvage X, Duchaussoy A, Zaher G. Strain Induced Segregations in Severely Deformed Materials. MATERIALS TRANSACTIONS. 2019;60(7):1151-8.

20. Edalati K, Uehiro R, Fujiwara K, Ikeda Y, Li H-W, Sauvage X, *et al.* Ultra-severe plastic deformation: Evolution of microstructure, phase transformation and hardness in immiscible magnesium-based systems. Materials Science and Engineering: A. 2017;701:158-66.

21. Edalati K, Uehiro R, Ikeda Y, Li H-W, Emami H, Filinchuk Y, *et al.* Design and synthesis of a magnesium alloy for room temperature hydrogen storage. Acta Materialia. 2018;149:88-96.

22. Ahn B, Lee H-J, Choi I-C, Kawasaki M, Jang J-I, Langdon TG. Micro-Mechanical Behavior of an Exceptionally Strong Metal Matrix Nanocomposite Processed by High-Pressure Torsion Advanced Engineering Materials. 2016;18(6):1001-8.

23. Ahn B, Zhilyaev AP, Lee H-J, Kawasaki M, Langdon TG. Rapid synthesis of an extra hard metal matrix nanocomposite at ambient temperature. Materials Science and Engineering: A. 2015;635:109-17.

24. Han JK, Lee HJ, Jang JI, Kawasaki M, Langdon TG. Micro-mechanical and tribological properties of aluminum-magnesium nanocomposites processed by high-pressure torsion. Materials Science and Engineering a-Structural Materials Properties Microstructure and Processing. 2017;684:318-27.

25. Kawasaki M, Ahn B, Lee H, Zhilyaev AP, Langdon TG. Using high-pressure torsion to process an aluminum-magnesium nanocomposite through diffusion bonding. Journal of Materials Research. 2016;31(1):88-99.

26. Kawasaki M, Han J-K, Lee D-H, Jang J-i, Langdon TG. Fabrication of nanocomposites through diffusion bonding under high-pressure torsion. Journal of Materials Research. 2018:1-11.

27. Kawasaki M, Jang JI. Micro-Mechanical Response of an Al-Mg Hybrid System Synthesized by High-Pressure Torsion. Materials. 2017;10(6).

28. Castro MM, Sabbaghianrad S, Pereira PHR, Mazzer EM, Isaac A, Langdon TG, *et al.* A magnesium-aluminium composite produced by high-pressure torsion. Journal of Alloys and Compounds. 2019;804:421-6.

29. Han J-K, Han DK, Liang GY, Jang J-I, Langdon TG, Kawasaki M. Direct Bonding of Aluminum–Copper Metals through High-Pressure Torsion Processing. Advanced Engineering Materials. 2018;20(11):1800642.

30. Bachmaier A, Keckes J, Kormout KS, Pippan R. Supersaturation in Ag–Ni alloy by two-step high-pressure torsion processing. Philosophical Magazine Letters. 2014;94(1):9-17.

31. Kormout KS, Yang B, Pippan R. Deformation Behavior and Microstructural Evolution of Cu–Ag Alloys Processed by High-Pressure Torsion. Advanced Engineering Materials. 2015;17(12):1828-34.

32. Kormout KS, Yang B, Pippan R. Transmission electron microscope investigations on Cu-Ag alloys produced by high-pressure torsion. IOP Conference Series: Materials Science and Engineering. 2014;63:012092.

33. Kormout KS, Ghosh P, Maier-Kiener V, Pippan R. Deformation mechanisms during severe plastic deformation of a CuAg composite. Journal of Alloys and Compounds. 2017;695:2285-94.

34. Bachmaier A, Motz C. On the remarkable thermal stability of nanocrystalline cobalt via alloying. Materials Science and Engineering: A. 2015;624:41-51.

35. Bachmaier A, Pfaff M, Stolpe M, Aboulfadl H, Motz C. Phase separation of a supersaturated nanocrystalline Cu–Co alloy and its influence on thermal stability. Acta Materialia. 2015;96:269-83.

36. Bachmaier A, Aboulfadl H, Pfaff M, Mücklich F, Motz C. Structural evolution and strain induced mixing in Cu–Co composites studied by transmission electron microscopy and atom probe tomography. Materials Characterization. 2015;100:178-91.

37. Bachmaier A, Schmauch J, Aboulfadl H, Verch A, Motz C. On the process of co-deformation and phase dissolution in a hard-soft immiscible CuCo alloy system during high-pressure torsion deformation. Acta Materialia. 2016;115:333-46.

38. Rogachev SO, Nikulin SA, Khatkevich VM, Sundeev RV, Komissarov AA. Features of Structure Formation in Layered Metallic Materials Processed by High Pressure Torsion. Metallurgical and Materials Transactions A. 2020;51(4):1781-8.

39. Bachmaier A, Rathmayr GB, Bartosik M, Apel D, Zhang Z, Pippan R. New insights on the formation of supersaturated solid solutions in the Cu–Cr system deformed by high-pressure torsion. Acta Materialia. 2014;69:301-13.

40. Sabirov I, Pippan R. Formation of a W–25%Cu nanocomposite during high pressure torsion. Scripta Materialia. 2005;52(12):1293-8.

41. Sabirov I, Pippan R. Characterization of tungsten fragmentation in a W–25%Cu composite after high-pressure torsion. Materials Characterization. 2007;58(10):848-53.

42. Edwards D, Sabirov I, Sigle W, Pippan R. Microstructure and thermostability of a W–Cu nanocomposite produced via high-pressure torsion. Philosophical Magazine. 2012;92(33):4151-66.

43. Ibrahim N, Peterlechner M, Emeis F, Wegner M, Divinski SV, Wilde G. Mechanical alloying via high-pressure torsion of the immiscible Cu50Ta50 system. Materials Science and Engineering: A. 2017;685:19-30.

44. Rogachev SO, Sundeev RV, Kozlov DA, Khalidova DV. Structure and Hardening of Layered Steel/Copper/Steel Material Subjected to Co-Deformation by High-Pressure Torsion. Physics of Metals and Metallography. 2019;120(2):191-6.

45. Rogachev SO, Nikulin SA, Sundeev RV. Formation of Turbulent Structures in Metallic Hybrid Materials Under Pressure Torsional Deformation. Metal Science and Heat Treatment. 2018;60(3):224-8.

46. Rogachev SO, Sundeev RV, Khatkevich VM. Evolution of the structure and strength of steel/vanadium alloy/steel hybrid material during severe plastic deformation. Materials Letters. 2016;173:123-6.

47. Rogachev SO, Nikulin SA, Khatkevich VM, Tabachkova NY, Sundeev RV. Structure Formation and Hardening of the Hybrid Material Based on Vanadium and Zirconium Alloys during High-Pressure Torsion. Russian Metallurgy (Metally). 2018;2018(4):372-6.

48. Luo D, Huminiuc T, Huang Y, Polcar T, Langdon TG. The fabrication of high strength Zr/Nb nanocomposites using high-pressure torsion. Materials Science and Engineering: A. 2020:139693.

49. Hernández-Escobar D, Unocic RR, Kawasaki M, Boehlert CJ. High-pressure torsion processing of Zn–3Mg alloy and its hybrid counterpart: A comparative study. Journal of Alloys and Compounds. 2020;831:154891.

50. Hernández-Escobar D, Marcus J, Han J-K, Unocic RR, Kawasaki M, Boehlert CJ. Effect of post-deformation annealing on the microstructure and micro-mechanical behavior of Zn–Mg hybrids processed by High-Pressure Torsion. Materials Science and Engineering: A. 2020;771:138578.

51. Hernández-Escobar D, Rahman ZU, Yilmazer H, Kawasaki M, Boehlert CJ. Microstructural evolution and intermetallic formation in Zn-Mg hybrids processed by High-Pressure Torsion. Philosophical Magazine. 2019;99(5):557-84.

52. Kubásek J, Vojtěch D, Jablonská E, Pospíšilová I, Lipov J, Ruml T. Structure, mechanical characteristics and in vitro degradation, cytotoxicity, genotoxicity and mutagenicity of novel biodegradable Zn–Mg alloys. Materials Science and Engineering: C. 2016;58:24-35.

53. Silva CLP, Oliveira AC, Costa CGF, Figueiredo RB, de Fátima Leite M, Pereira MM, *et al.* Effect of severe plastic deformation on the biocompatibility and corrosion rate of pure magnesium. Journal of Materials Science. 2017;52(10):5992-6003.

54. Silva CLP, Soares RB, Pereira PHR, Figueiredo RB, Lins VFC, Langdon TG. The Effect of High-Pressure Torsion on Microstructure, Hardness and Corrosion Behavior for Pure Magnesium and Different Magnesium Alloys. Advanced Engineering Materials. 2019;21(3):1801081.

55. Lopes DR, Silva CLP, Soares RB, Pereira PHR, Oliveira AC, Figueiredo RB, *et al.* Cytotoxicity and Corrosion Behavior of Magnesium and Magnesium Alloys in Hank's Solution after Processing by High-Pressure Torsion. Advanced Engineering Materials. 2019;21(8):1900391.

56. Srinivasarao B, Zhilyaev AP, Langdon TG, Pérez-Prado MT. On the relation between the microstructure and the mechanical behavior of pure Zn processed by high pressure torsion. Materials Science and Engineering: A. 2013;562:196-202.

57. Figueiredo RB, Langdon TG. Processing Magnesium and Its Alloys by High-Pressure Torsion: An Overview. Advanced Engineering Materials. 2019;21(1):1801039.

58. Liu S, Kent D, Doan N, Dargusch M, Wang G. Effects of deformation twinning on the mechanical properties of biodegradable Zn-Mg alloys. Bioactive Materials. 2019;4:8-16.

59. Jarzębska A, Bieda M, Kawałko J, Rogal Ł, Koprowski P, Sztwiertnia K, *et al.* A new approach to plastic deformation of biodegradable zinc alloy with

magnesium and its effect on microstructure and mechanical properties. Materials Letters. 2018;211:58-61.

60. Somekawa H, Mukai T. Effect of grain boundary structures on grain boundary sliding in magnesium. Materials Letters. 2012;76:32-5.

61. Figueiredo RB, Sabbaghianrad S, Giwa A, Greer JR, Langdon TG. Evidence for exceptional low temperature ductility in polycrystalline magnesium processed by severe plastic deformation. Acta Materialia. 2017;122:322-31.

62. Zhang P, Li SX, Zhang ZF. General relationship between strength and hardness. Materials Science and Engineering: A. 2011;529:62-73.

63. Zhilyaev AP, Langdon TG. Using high-pressure torsion for metal processing: Fundamentals and applications. Progress in Materials Science. 2008;53(6):893-979.

64. Pouryazdan M, Kaus BJP, Rack A, Ershov A, Hahn H. Mixing instabilities during shearing of metals. Nature Communications. 2017;8(1):1611.

65. Kormout KS, Pippan R, Bachmaier A. Deformation-Induced Supersaturation in Immiscible Material Systems during High-Pressure Torsion Advanced Engineering Materials. 2017;19(4).

66. Silva CLP, Tristão IC, Sabbaghianrad S, Torbati-Sarraf SA, Figueiredo RB, Langdon TG. Microstructure and Hardness Evolution in Magnesium Processed by HPT. Materials Research. 2017;20:2-7.

67. Figueiredo RB, Poggiali FSJ, Silva CLP, Cetlin PR, Langdon TG. The influence of grain size and strain rate on the mechanical behavior of pure magnesium. Journal of Materials Science. 2016;51(6):3013-24.

68. Wagoner RH. Strain-rate sensitivity of zinc sheet. Metallurgical and Materials Transactions A. 1984;15(6):1265-71.

69. Tian YZ, Wu SD, Zhang ZF, Figueiredo RB, Gao N, Langdon TG. Microstructural evolution and mechanical properties of a two-phase Cu-Ag alloy processed by high-pressure torsion to ultrahigh strains. Acta Materialia. 2011;59(7):2783-96.

70. Hohenwarter A, Taylor A, Stock R, Pippan R. Effect of Large Shear Deformations on the Fracture Behavior of a Fully Pearlitic Steel. Metallurgical and Materials Transactions A. 2011;42(6):1609-18.

71. Huang Y, Kawasaki M, Langdon TG. Influence of anvil alignment on shearing patterns in high-pressure torsion. Advanced Engineering Materials. 2013;15(8):747-55.

72. Huang Y, Kawasaki M, Langdon TG. An investigation of flow patterns and hardness distributions using different anvil alignments in high-pressure torsion. Journal of Materials Science. 2013;48(13):4533-42.

73. Huang Y, Kawasaki M, Langdon TG. An evaluation of the shearing patterns introduced by different anvil alignments in high-pressure torsion. Journal of Materials Science. 2014;49(8):3146-57.

74. Figueiredo RB, De Faria GCV, Cetlin PR, Langdon TG. Three-dimensional analysis of plastic flow during high-pressure torsion. Journal of Materials Science. 2013;48(13):4524-32.

75. Gola A, Schwaiger R, Gumbsch P, Pastewka L. Pattern formation during deformation of metallic nanolaminates. Physical Review Materials. 2020; 4(1):013603.

76. Beygelzimer Y. Vortices and Mixing in Metals during Severe Plastic Deformation. Materials Science Forum. 2011;683:213-24.

77. Kulagin R, Beygelzimer Y, Ivanisenko Y, Mazilkin A, Straumal B, Hahn H. Instabilities of interfaces between dissimilar metals induced by high pressure torsion. Materials Letters. 2018;222:172-5.

78. Kulagin R, Zhao Y, Beygelzimer Y, Toth LS, Shtern M. Modeling strain and density distributions during high-pressure torsion of pre-compacted powder materials. Materials Research Letters. 2017;5(3):179-86.

79. Kulagin R, Beygelzimer Y, Ivanisenko Y, Mazilkin A, Hahn H. High Pressure Torsion: from Laminar Flow to Turbulence. IOP Conference Series: Materials Science and Engineering. 2017;194:012045.

80. Hohenwarter A, Bachmaier A, Gludovatz B, Scheriau S, Pippan R. Technical parameters affecting grain refinement by high pressure torsion. International Journal of Materials Research. 2009;100(12):1653-61.

81. Figueiredo RB, Aguilar MTP, Cetlin PR, Langdon TG. Deformation heterogeneity on the cross-sectional planes of a magnesium alloy processed by high-pressure torsion. Metallurgical and Materials Transactions A. 2011;42(10):3013-21.

82. Figueiredo RB, Langdon TG. Development of structural heterogeneities in a magnesium alloy processed by high-pressure torsion. Materials Science and Engineering A. 2011;528(13-14):4500-6.

83. Cao Y, Wang YB, Figueiredo RB, Chang L, Liao XZ, Kawasaki M, *et al.* Three-dimensional shear-strain patterns induced by high-pressure torsion and their impact on hardness evolution. Acta Materialia. 2011;59(10):3903-14.

84. Tian YZ, An XH, Wu SD, Zhang ZF, Figueiredo RB, Gao N, *et al.* Direct observations of microstructural evolution in a two-phase Cu-Ag alloy processed by high-pressure torsion. Scripta Materialia. 2010;63(1):65-8.

85. Kormout KS, Pippan R, Bachmaier A. Deformation-Induced Supersaturation in Immiscible Material Systems during High-Pressure Torsion Advanced Engineering Materials. 2017;19(4):1600675.

86. Kawasaki M, Langdon T. Review: achieving superplasticity in metals processed by high-pressure torsion. Journal of Materials Science. 2014;49(19):6487-96.

87. Somekawa H, Mukai T. Hall–Petch Breakdown in Fine-Grained Pure Magnesium at Low Strain Rates. Metallurgical and Materials Transactions A. 2015;46(2):894-902.

88. Kawasaki M, Ahn B, Lee H, Zhilyaev AP, Langdon TG. Using high-pressure torsion to process an aluminum–magnesium nanocomposite through diffusion bonding. Journal of Materials Research. 2015;31(1):88-99.

89. Edalati K, Masuda T, Arita M, Furui M, Sauvage X, Horita Z, *et al.* Room-Temperature Superplasticity in an Ultrafine-Grained Magnesium Alloy. Scientific Reports. 2017;7.

90. Kumar P, Kawasaki M, Langdon TG. Review: Overcoming the paradox of strength and ductility in ultrafine-grained materials at low temperatures. Journal of Materials Science. 2016;51(1):7-18.

91. Kawasaki M, Lee H-J, Choi I-C, Jang J-i, Ahn B, Langdon TG. Evolution of hardness, microstructure, and strain rate sensitivity in a Zn-22% Al eutectoid alloy processed by high-pressure torsion. IOP Conference Series: Materials Science and Engineering. 2014;63:012101.

92. Kawasaki M, Ahn B, Langdon TG. Microstructural evolution in a two-phase alloy processed by high-pressure torsion. Acta Materialia. 2010;58(3):919-30.

93. Chinh NQ, Valiev RZ, Sauvage X, Varga G, Havancsák K, Kawasaki M, *et al.* Grain boundary phenomena in an ultrafine-grained Al–Zn alloy with improved mechanical behavior for micro-devices. Advanced Engineering Materials. 2014;16(8):1000-9.

94. Chinh NQ, Csanádi T, Győri T, Valiev RZ, Straumal BB, Kawasaki M, *et al.* Strain rate sensitivity studies in an ultrafine-grained Al–30wt.% Zn alloy using micro- and nanoindentation. Materials Science and Engineering: A. 2012;543:117-20.

95. Edalati K, Horita Z, Valiev RZ. Transition from poor ductility to room-temperature superplasticity in a nanostructured aluminum alloy. Scientific Reports. 2018;8(1):6740.

Chapter 9.

Final Remarks

9.1. General conclusions

This doctoral thesis presents the fabrication and characterization of distinct Mg-based hybrids produced by HPT through particles mixture and consolidation at room temperature. The results enable the following conclusions:

- It is possible to consolidate Mg (pure or alloy) in the form of coarse particles or machining chips by HPT processing at room temperature. Other materials can be introduced into the Mg matrix to produce different Mg-matrix hybrids, such as composites reinforced with light oxides, quasicrystals and bioactive materials.
- There is evidence of Hall-Petch breakdown in the AZ91 Mg alloy after HPT processing. The insertion of the hard phase seems to contribute to achieving finer grain sizes in the Al_2O_3 reinforced composite when compared to the unreinforced one.
- The structural integrity of some hybrids was examined by tensile tests. The CP-Mg matrix hybrids display high tensile strength, which shows full consolidation. Some of the AZ91 matrix hybrids show evidence of lack of bonding after a few turns of HPT, which suggests this alloy requires larger strains to achieve full consolidation.
- The mechanical mixture of two soft metals by HPT leads to continuous stretching, bending and fragmentation of phases in the submicrometric range. It appears that mechanical stirring during HPT plays a major role than diffusional processes in the processed hybrids.

9.2. Original Contribution and Future Work

The research carried out during this work has led to many novel information which shows original contribution to the area. Although some early papers report consolidation of pure Mg particles and a few papers report the mixing of Mg with other metallic materials, a systematic study on the incorporation of different

particles (including ceramic and bioactive particles) and phases to produce Mg matrix hybrids using HPT had not been carried out.

Many papers in the literature have reported consolidation of metallic powders such as Al and Cu, with or without incorporation of other particles, using 5 turns of HPT at 6 GPa. The present research showed that this is not the case with a Mg alloy AZ91, which requires more turns. Also, many papers report consolidation of powders but do not test the consolidated material in tension. Such test is of major importance to evaluate the mechanical integrity of the material. The present research showed good tensile strength in pure Mg and Mg-Quasicrystal and Mg-HA hybrids consolidated by HPT. The present research also showed that the processing route used in this investigation is an effective way to incorporate bioactive material in a Mg matrix. This provides the possibility to produce bioactive and biodegradable hybrids.

Finally, the present investigation showed evidence of inverse Hall-Petch behaviour in a Mg alloy and shed light on the mechanism of shear mixing of ductile phases during deformation.

This doctorate has led to the publication of nine papers in peer-reviewed journals, which six of them had their "as submitted" version presented on this manuscript, and the other three are listed in section *9.3. Other published papers* [1-3]. Furthermore, the results obtained in this research was presented at five conferences.

Some recommendations of future work include:

- Evaluate the role of particle size distribution on the effectiveness of dispersion of phases and consolidation.
- Evaluate the role of HPT hydrostatic pressure on the effectiveness of consolidation of metallic particles.
- Exploit novel systems in collaboration with research groups in the biomedical area to investigate the feasibility of producing biodegradable Mg-matrix composites with the ability to act as controlled drug delivery systems.

9.3. Other published papers:

1. Lopes D, Soares RB, Castro MM, Figueiredo RB, Langdon TG, Lins VFC. Corrosion Behavior in Hank's Solution of a Magnesium–Hydroxyapatite Composite Processed by High-Pressure Torsion. Advanced Engineering Materials. 2020: 2000765.
https://doi.org/10.1002/adem.202000765

2. Castro MM, Sabbaghianrad S, Pereira PHR, Mazzer EM, Isaac A, Langdon TG, *et al.* A magnesium-aluminium composite produced by high-pressure torsion. Journal of Alloys and Compounds. 2019; 804: 421-6.
https://doi.org/10.1016/j.jallcom.2019.07.007

3. Castro MM, Pereira PR, Figueiredo RB, Langdon TG. Developing magnesium-based composites through high-pressure torsion. Letters on Materials. 2019; 9(4s): 541-5.
https://doi.org/10.22226/2410-3535-2019-4-541-545

9.4. Considerações finais

A presente tese de doutorado apresenta a fabricação e caracterização de diferentes híbridos à base de Mg produzidos por HPT através da mistura e consolidação de partículas em temperatura ambiente. A pesquisa realizada durante este trabalho gerou muitas informações inovadoras que mostram uma contribuição original para a área e resultou na publicação de nove artigos em periódicos revisados por pares, dos quais seis têm sua versão "como submetida" apresentada neste manuscrito, e os outros três estão listados na seção ***"9.3. Other published papers"***. Além disso, os resultados obtidos nesta pesquisa foram apresentados em cinco conferências.

Apesar de já haver alguns trabalhos relatando a consolidação de partículas de Mg (puro ou misturados com outros materiais metálicos), ainda não havia sido realizado um estudo sistemático sobre a incorporação de diferentes partículas (ex.: cerâmicas ou bioativas) para produzir híbridos de Mg por HPT.

Muitos trabalhos na literatura relatam a consolidação de pós metálicos como alumínio e cobre, com ou sem incorporação de outras partículas, usando 5 voltas

de HPT e 6 GPa. A presente pesquisa mostrou que este não é o caso para a liga de Mg AZ91, que requer um número maior de voltas. Além disso, muitos artigos relatam a consolidação de pós, mas não testam o material em tração. Assim, essa tese é de suma importância para avaliar a integridade mecânica do material.

A presente pesquisa mostrou boa resistência à tração em híbridos de Mg de pureza comercial (magnésio-quasicristal e magnésio-hidroxiapatita) consolidados por HPT. Além disso, mostrou que a rota de processamento utilizada nesta investigação é uma forma eficaz de incorporação de material bioativo em uma matriz de Mg, indicando a possibilidade de produzir híbridos bioativos e biodegradáveis.

Finalmente, a presente investigação mostrou evidências de quebra de Hall-Petch em uma liga de Mg e esclareceu o mecanismo de mistura pelo cisalhamento de fases dúcteis durante a deformação.

As conclusões gerais deste trabalho podem ser resumidas em quatro tópicos principais:

- É possível consolidar partículas grosseiras ou cavacos de usinagem de Mg (puro ou liga) por HPT em temperatura ambiente. Outros materiais (como óxidos leves, quasicristais e materiais bioativos) podem ser introduzidos na matriz de Mg para produzir diferentes compósitos.
- Há evidências de quebra de Hall-Petch na liga de Mg AZ91 após o processamento por HPT. A inserção da fase dura parece contribuir para a obtenção de grãos mais finos no compósito reforçado com Al2O3 quando comparado ao material não reforçado.
- Os híbridos de matriz de Mg de pureza comercial apresentam alta resistência à tração (indicando consolidação total), enquanto alguns dos híbridos de matriz de AZ91 apresentam evidências de falhas na consolidação após algumas voltas de HPT, mostrando que esta liga requer deformações maiores para atingir a consolidação total.
- A mistura mecânica de dois metais macios por HPT leva ao alongamento, dobramento e fragmentação contínua das fases na faixa submicrométrica. Parece que o cisalhamento em si durante o HPT desempenha um papel mais importante do que processos de difusão na mistura dos híbridos estudados.